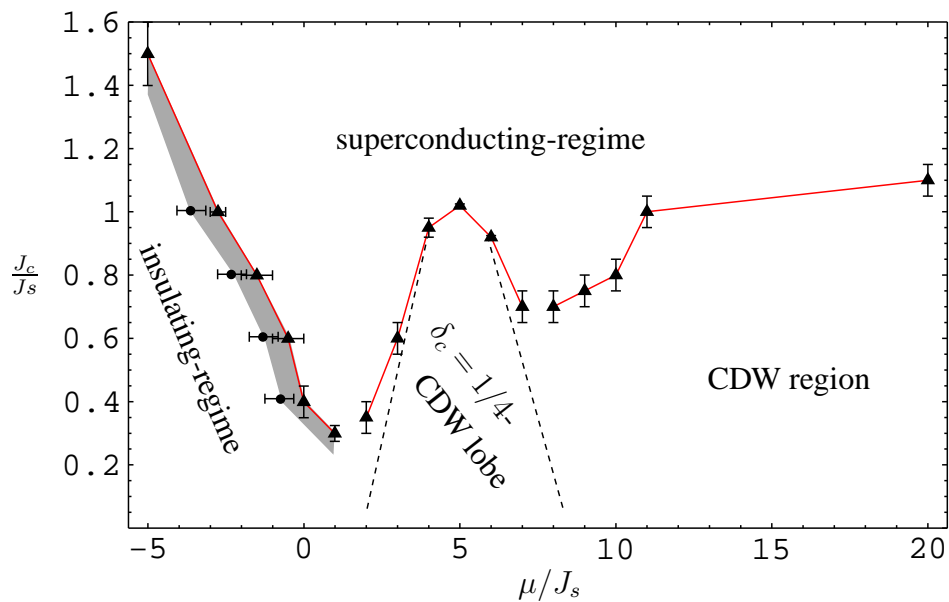


# On the competition of superconductivity, antiferromagnetism and charge order in the high- $T_c$ compounds

Dissertation zur Erlangung des  
naturwissenschaftlichen Doktorgrades  
der Bayerischen Julius-Maximilians-Universität Würzburg



vorgelegt von

MARTIN JÖSTINGMEIER

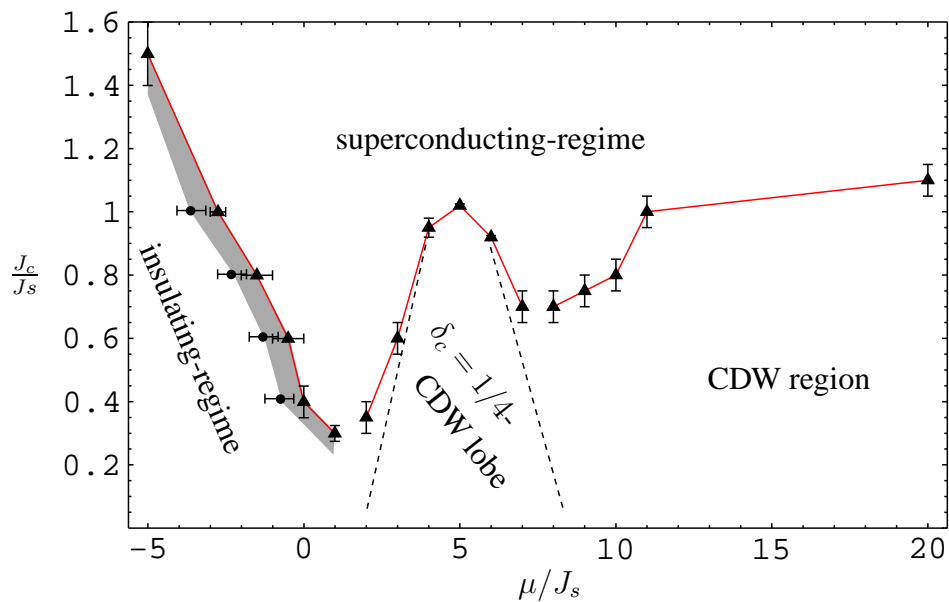
aus Halle (Westf.)

Würzburg, 2005



# On the competition of superconductivity, antiferromagnetism and charge order in the high- $T_c$ compounds

Dissertation zur Erlangung des  
naturwissenschaftlichen Doktorgrades  
der Bayerischen Julius-Maximilians-Universität Würzburg



vorgelegt von

MARTIN JÖSTINGMEIER

aus Halle (Westf.)

Würzburg, 2005

Eingereicht am:

bei der Fakultät für Physik und Astronomie

1. Gutachter: Professor Dr. Werner Hanke
  2. Gutachter: Professor Dr. Enrico Arrigoni (TU Graz)
- der Dissertation

1. Prüfer: Professor Dr. Werner Hanke
  2. Prüfer: Professor Dr. Fakher Assaad
  3. Prüfer: Professor Dr. Friedrich Reinert
- im Promotionskolloquium

Tag des Promotionskolloquiums: 29.04.2005

Promotionsurkunde ausgehändigt am:

Für  
Christina Maria



# Contents

---

<b>Introduction</b>	<b>1</b>
<b>1 Stochastic-Series Expansion</b>	<b>9</b>
1.1 Formulation of the SSE . . . . .	9
1.2 Operator-Loop Update . . . . .	12
1.3 Accessing Physical Observables . . . . .	16
1.3.1 Calculating Expectation Values . . . . .	16
1.3.2 Accessing Correlation Functions . . . . .	17
1.4 Conclusions . . . . .	21
<b>2 Effective Models</b>	<b>23</b>
2.1 Constructing an effective Hamiltonian via the Contractor- Renormalization Group Procedure . . . . .	24
2.2 The effective Hamiltonian . . . . .	28
2.3 Conclusions . . . . .	29
<b>3 <math>SO(5)</math>-Theory</b>	<b>31</b>
3.1 Introduction . . . . .	31
3.2 Mathematical formulation . . . . .	33
3.3 $SO(5)$ Symmetry in the Hubbard- and $t - J$ Model . . . . .	35
3.4 The projected $SO(5)$ -theory . . . . .	36
3.4.1 The projected $SO(5)$ Model . . . . .	38
3.4.2 Properties of the projected $SO(5)$ Model . . . . .	39
<b>4 Numerical Analysis of the projected <math>SO(5)</math> Model</b>	<b>40</b>
4.1 Phase Diagram . . . . .	40

4.2	Scaling Analysis . . . . .	42
4.2.1	Case $J_s = J_c/2$ , static $SO(5)$ -symmetry . . . . .	42
4.2.2	Case $J_s = J_c$ . . . . .	44
4.3	Validity of the Crossover Exponents obtained by the numerical Analysis . . . . .	48
4.4	Conclusions . . . . .	49
<b>5</b>	<b>Extension of the projected-<math>SO(5)</math> Model</b>	<b>51</b>
5.1	The extended projected $SO(5)$ Model . . . . .	52
5.2	Excuse: Phase Transitions in 2D-Systems . . . . .	54
5.2.1	Detecting Superconductivity in 2D-Systems . . . . .	54
5.2.2	Antiferromagnetic Order in 2D-Systems . . . . .	55
5.3	Phase Diagram of the $epSO(5)$ Model in 2D . . . . .	57
5.3.1	Doping Dependence of the Checkerboard Order . . . . .	62
5.3.2	Detailed Investigation of the CDW to SC Transition on Top of the $\delta_c = 1/4$ insulating Lobe . . . . .	65
5.3.3	Beyond HTSC: Supersolid Phase . . . . .	70
5.4	Conclusions . . . . .	73
<b>6</b>	<b>Summary</b>	<b>74</b>
<b>A</b>	<b>Calculation of the Spin Stiffness</b>	<b>78</b>
	<b>Bibliography</b>	<b>81</b>
	<b>Zusammenfassung</b>	<b>89</b>
	<b>Publikationen</b>	<b>95</b>
	<b>Lebenslauf</b>	<b>97</b>
	<b>Danksagung</b>	<b>99</b>



# Introduction

---

Superconductivity attracted enormous attention after its discovery in 1911 by the Dutch physicist H. Kamerlingh Onnes<sup>1</sup>. He succeeded in liquefying <sup>4</sup>He, opening the possibility to study the resistivity of metals at extremely low temperatures. Thereby he observed that the electrical resistance of mercury disappears when cooled down to 4.2K [1]. Later it turned out that a large number of metals and alloys are superconductors. The typical critical temperatures range from 1K to about 18K. A first successful attempt to describe the properties of superconductors has been reported by Ginzburg and Landau in 1950. They applied their theory of second-order phase transitions to characterize the behavior of the superconductors close to the superconducting (SC) transition temperature  $T_c$  [2]. Whereas their approach was phenomenological, a microscopic theory, starting from the constituent electrons and ions, was lacking until 1957, when Bardeen, Cooper and Schrieffer (BCS) explained the phenomenon of SC in metals and alloys [3]. According to their so called ‘BCS-theory’ (for which Bardeen, Cooper and Schrieffer were awarded with the Nobel Prize 1972), two electrons of opposite spin and momentum form “Cooper pairs” and condense into a symmetry broken ground state. The attraction of two electrons, which is necessary to form the pairs is mediated by the interaction of the electrons with phonons (lattice vibrations). This theory explained existing experiments and makes a lot of predictions, that have later been confirmed experimentally. The probably most well-known is the ‘isotope effect’: Due to the essential role of the lattice vibrations, the SC transition temperature depends on the mass of the atoms ( $m_{atom}$ ), which form the crystal lattice, i.e.,  $T_c \propto \sqrt{m_{atom}}^{-1}$ . This proportionality has been checked experimentally by replacing the atoms in the crystal by different isotopes of the same element.

The discovery of high-temperature superconductors (HTSC) in 1986 by Bednorz and Müller (Nobel Prize 1987) dramatically enhanced the interest in superconductivity. They

---

<sup>1</sup>For the achievement of liquefying <sup>4</sup>He H. Kamerlingh Onnes was honored with Nobel Prize in 1913

measured an unusually high SC transition temperature of about  $33K$  in the ‘ceramic’ compound  $\text{La}_{2-\delta}\text{Ba}_\delta\text{CuO}_4$  [4]. In the following months and years a burst of activity started and further high- $T_c$  superconductors, all of cuprate type (i.e.  $\text{CuO}_2$ -planes as essential lattice units), were synthesized:  $\text{La}_{2-\delta}\text{Sr}_\delta\text{CuO}_4$ ,  $\text{YBa}_2\text{Cu}_3\text{O}_{7-\delta}$ ,  $\text{Bi}_2\text{Sr}_2\text{CaCu}_2\text{O}_{8+\delta}$ ,  $\text{Tl}_2\text{Ba}_2\text{CuO}_{6+\delta}$ ,  $\text{HgBa}_2\text{Ca}_2\text{Cu}_3\text{O}_{8+\delta}$  or  $\text{Ca}_{2-\delta}\text{Na}_\delta\text{CuO}_2\text{Cl}_2$ , to name only a few. The critical SC-transition temperatures ( $T_c$ ) for these materials range up to  $T_c = 138K$  for  $\text{HgBa}_2\text{Ca}_2\text{Cu}_3\text{O}_{8+\delta}$  [5]. This makes the HTSC, in principle, interesting candidates for technical applications, because this temperature can be easily achieved using liquid  $\text{N}_2$  instead of rather expensive liquid  $^4\text{He}$ . However, the synthesis of these new copper-oxide based materials was mostly empirical, because a ‘guiding theory’, i.e., the BCS-theory evidently fails to describe the high- $T_c$  superconductors. For example, the transition temperature of the high- $T_c$  superconductors shows essentially no isotope effect at optimal doping, which is, as discussed above, in contradiction to key predictions of the BCS-theory. Also the experimentally observed d-wave symmetry of the SC order parameter [6, 7] cannot be understood straight forwardly in terms of a conventional phonon mediated mechanism. These experimental results suggest that the mechanism of high- $T_c$  superconductivity is mainly of an electronic nature.<sup>2</sup> However, until today there is no consensus about the microscopic origin of the high- $T_c$  superconductivity.

Such a theory would obviously be important in order to ‘show the way’ to obtain superconductors with a higher transition temperature, than available today.

An important common feature of all high- $T_c$  superconductors is the presence of stacked copper-oxide layers, separated by layers containing rare earth metals. It is well accepted that SC takes place in these copper-oxide layers. Doping with rare earth metals controls the charge carrier density in the copper-oxide planes and, thereby, has a profound impact on the material properties. At zero doping no ‘free’ charge carriers are available in the copper-oxide planes, and the materials show antiferromagnetic (AF) Mott insulating behavior. The situation changes already for small doping ( $\delta$ ), i.e., at  $\delta \approx 3\%$  the copper-oxide layers start to become SC (see Fig. 3.3). As soon as it became clear that BCS-theory cannot fully account for high- $T_c$  superconductivity, different theories have been proposed. The simplest model for the copper-oxide planes is the so called ‘*Hubbard-model*’, containing only two ingredients: a kinetic energy term, which describes the motion of the electrons on a two-dimensional (2D) lattice, and an on-site interaction term. The latter models the Coulomb repulsion, i.e., if two electrons occupy the same orbital. Despite its conceptual simplicity the *Hubbard-model* still awaits an exact solution in two and three dimensions. The standard approach to describe such a

---

<sup>2</sup>Recent experiments also suggest the importance of an interaction between electrons and phonons [8, 9] in copper-oxide superconductors, however it is well established, that the electron-electron interaction plays a major role in the HTSC.

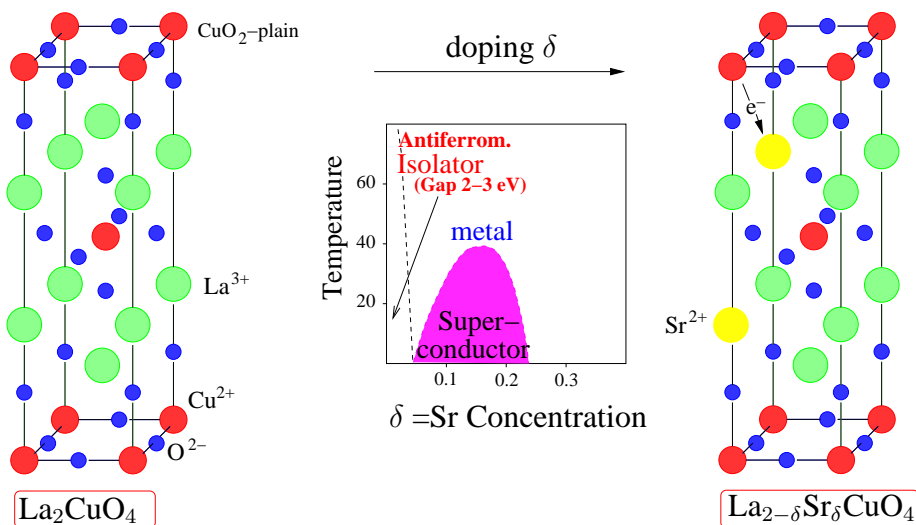


Figure 1: Lattice structure of a typical high- $T_c$  superconductor ( $\text{La}_{2-\delta}\text{Sr}_\delta\text{CuO}_4$ ) The Strontium atoms between the  $\text{CuO}_2$  layers remove electrons from these layers, and thereby introduce holes. These holes are the effective charge carriers in the superconducting  $\text{CuO}_2$  layers. Thus doping with Strontium changes the properties of  $\text{La}_{2-\delta}\text{Sr}_\delta\text{CuO}_4$  from an AF insulator at zero doping to a superconductor when  $0.7 \gtrsim \delta \gtrsim 0.25$ .

system would be to start from the non interacting system and introduce the interaction as a small perturbation. This assumes typically that the physics of the interacting system evolves adiabatically, i.e., from the non-interacting system when ‘switching’ on smoothly the interaction. This picture holds, if the interaction is small in comparison to the bandwidth. However, for the physics of the high- $T_c$  superconductors this standard Fermi-liquid approach does not work, because the Coulomb interaction is of the order of the bandwidth or even larger and, therefore, cannot be considered as a small perturbation. A possible way out is to solve the *Hubbard-model* numerically. There are in principle two complementary ways: One possibility is to diagonalize the Hamiltonian exactly. This method is very successful in studying the ground-state properties of small systems. For bigger systems and finite temperatures, however, this method cannot be applied successfully, because the Hilbert space grows like  $4^{N_s}$ , where  $N_s$  denotes the number of lattice sites. The second possibility is to apply importance sampling of the states. This procedure is carried through using the Quantum-Monte Carlo (QMC) technique. QMC simulations of fermionic models have been very useful to study the *Hubbard-model* [10, 11, 12, 13, 14]. The maximum system sizes are typically of the order of 100 lattice sites and also the accessible temperatures range down to  $T \approx 0.1t$ , where  $t$  corresponds to about  $0.5eV$ . Thus, the accessible parameter regime is rather

limited. The limitation is due to the necessary anti-symmetrization of the fermionic wave function, which introduces a severe sign problem in the importance sampling of the states. Moreover, this sign problem is strongly doping dependent, and becomes worse upon going away from half-filling further reducing the accessible parameter (temperature and system size) range.

On the analytical side, one of the first theoretical proposals for understanding HTSC was Anderson's so called "Resonating-Valence Bond" (RVB) theory [15]. In this theory, the Hilbert space of the *Hubbard-model* is reduced to the subspace of no double occupancies. The RVB ground state can be formally generated as a Gutzwiller projection of the BCS ground-state wave function, where electrons bind to a spin-singlet pair. These pairs then form a kind of Bose liquid of "pair bonds". This phenomenological ansatz is able to explain a variety of experimental observations [16], e.g. the pseudogap, properties of nodal quasiparticles and approximate spin-charge separation. Doping of the RVB-liquid state naturally leads to superconductivity. However, the original RVB Ansatz is not able to describe the long-range antiferromagnetic phase apparent in all HTSC.

A second rather different, successful theory for the HTSC is the '*SO(5)*-theory' of high- $T_c$  superconductivity [17, 18]. Here, the general idea is to use symmetry to resolve uniquely the competition between the different, yet nearly degenerate ground-states at low temperatures and energy. The AF has an underlying *SO(3)* symmetry, broken at  $T_{\text{Néel}}$  and the SC a *U(1)* symmetry, broken at  $T_c$ . The *SO(5)*-theory comprises the *SO(3)* and the *U(1)* symmetry and enlarges it to an *SO(5)*-Lie algebra [18]. This then allows for 'rotations' from the AF to the SC states and vice versa, and thereby connects both phases quite naturally. As described later in more detail, the *SO(5)*-theory describes the physics of the HTSC in terms of characteristic bosonic excitations, i.e., triplets and hole-pairs. It has recently been shown that the '2D-projected-*SO(5)* theory', which projects out the 'high-energy' physics of the double occupancies of charge carriers (due to the Hubbard- $U \approx 5eV$ ), can account for the global phase diagram [19], i.e., a SC phase, the experimentally observed Mott-Hubbard physics and dynamical properties, such as the dispersion of the  $k = (\pi, \pi)$  neutron resonance peak [20].

Both, the *SO(5)*-theory as well as the RVB phenomenology capture essential ingredients of the physics in the copper-oxide planes of the HTSC, using a bosonic description of the low energy physics.

In this effective bosonic description, the difficulties connected with fermionic Quantum-Monte Carlo simulations can be circumvented. Chap. 1 is dedicated to a description of an algorithm that is perfectly suited to simulate bosonic model systems, namely the *Stochastic Series Expansion* (SSE). Also its implementation is discussed in the framework of the operator-loop update [21, 22]. One major part of this work was to optimize the algorithm. Last, but not least, these optimizations made it possible to study

systems of the order of  $\approx 10^4$  lattice sites. This corresponds to an increase of about one order of magnitude in comparison to earlier implementations and two orders in comparison with fermionic Quantum-Monte Carlo simulations.

The next chapter (Chap. 2) addresses the question how a physically relevant bosonic Hamiltonian for the high- $T_c$  superconductors may be constructed. One possibility is provided by the so called ‘Contractor-Renormalization Group approach’. This method has been used to map the fermionic *Hubbard-model* onto an effective low-energy Hamiltonian [23], which can subsequently be analyzed numerically using the *Stochastic-Series Expansion* [20, 19].

As already mentioned above, there exists also an alternative way to derive an effective bosonic Hamiltonian for the HTSC: The  $SO(5)$ -theory of high- $T_c$  superconductivity [17, 18]. The  $SO(5)$ -theory starts from the experimental observation, that all copper-oxide superconductors share a significant common feature in their phase diagram, i.e the proximity of to competing phases: antiferromagnetism (AF) and superconductivity (SC). The main idea of the  $SO(5)$ -theory is to use symmetry arguments, leading to a unified description of antiferromagnetism and superconductivity. This concept is motivated by the success of employing symmetry principles in other fields in physics. One of the most famous examples of symmetry approaches is the unification of the magnetic field  $\vec{B}$  and the electric field  $\vec{E}$  into a common electro-magnetic field tensor  $F_{\mu\nu}$  in the theory of relativity.

The  $SO(5)$ -theory is presented in chapter 3 and, as already stated above, it permits to construct an effective bosonic Hamiltonian for the high- $T_c$  superconductors. Astonishingly, the model which is motivated by the  $SO(5)$ -theory has a strong similarity to the Hamiltonian, that has been constructed independently in chapter 2 by means of the Contractor-Renormalization Group approach (in the physically relevant strong-coupling regime  $U \approx 8t$ ) [23].

So far the three concepts of treating strongly-correlated many-body systems had been connected only loosely, i.e., the  $SO(5)$ -theory as well as the Contractor-Renormalization Group approach permit to motivate an effective bosonic Hamiltonian, that can be studied efficiently using the SSE. However, when looking at the energy scales in the HTSC problem, the connection between the  $SO(5)$ -theory, the SSE and the Contractor-Renormalization Group approach becomes obvious (see Fig. 2): The energy scale of the interactions in the *Hubbard-model*, which is commonly believed to be the simplest relevant model for the HTSC, is of the order of several eV ( $U \approx 5$  eV). But the interesting phenomena in the high-temperature superconductors, i.e., the competition between antiferromagnetic-, superconducting- or charge-ordered states take place at an energy

scale corresponding to  $k_B T_c$ , i.e., at only few meV (100K correspond to  $\approx 8.6\text{meV}$ ). In order to extract the relevant physics for the low-energy regime from a ‘high-energy’ model, the three concepts, i.e. the  $SO(5)$ -theory, the SSE and the Contractor-Renormalization Group technique can be combined to a multi-stage procedure, depicted in Fig. 2. When starting from the ‘high-energy’ *Hubbard-model*, the Contractor-Renormalization Group technique permits (within only one iteration) to construct an effective Hamiltonian, that brings the energy scale down to 100 – 150 meV [23] (see also Fig. 2.4). Subsequently, this effective Hamiltonian can be studied at temperatures corresponding to  $T_c$  using the SSE. On the other hand, according to the  $SO(5)$ -theory, the competition between the quasi-degenerate states at these low temperatures should be controlled by an  $SO(5)$ -symmetry close to a multicritical point [18].

In the following two chapters (Chap. 4 and Chap. 5), the results obtained by the bosonic Quantum-Monte Carlo simulations are presented. Chapter 4 starts with a detailed numerical study of the so called ‘projected- $SO(5)$  model’, using the essentially numerical exact Stochastic Series Expansion (SSE). The projected- $SO(5)$  model describes the physics in terms of four hard-core bosons, i.e. three triplets and the hole-pair or Cooper-pair bosons. The boson, which contains two doubly occupied (with electrons) sites has been projected out. The results are encouraging: The projected- $SO(5)$  model indeed reproduces salient features of the high- $T_c$  superconductors and captures the competition between AF and SC order [24, 19]. But what about the role of the  $SO(5)$ -symmetry? In the projected- $SO(5)$  model the  $SO(5)$ -symmetry is manifestly broken on the Hamiltonian level, but for the validity of the  $SO(5)$ -theory the Hamiltonian does not need to be  $SO(5)$ -invariant. This is expressed already in Zhang’s original  $SO(5)$ -theory [17], where the chemical potential breaks the  $SO(5)$ -symmetry. Nevertheless, in the low energy regime the competition of antiferromagnetism and superconductivity in the vicinity of multi-critical point should be described by  $SO(5)$ -scaling relations [?].

Due to the efforts spent towards an optimization of the code [21, 22], it was possible to calculate the 3D-phase diagram with an unprecedented accuracy, permitting even to determine the scaling behavior close to multi-critical points. This is essential, since it allows to address the central question of  $SO(5)$ -symmetry restoration in the vicinity of a multi-critical point. The detailed analysis is presented in in Sec. 4.2.

Restricting the theory to antiferromagnetism and superconductivity is, however, not sufficient, because the real copper-oxides display also a variety of other different phases, for example charge density waves [25, 26, 27, 28, 29]. It is under discussion how these ‘checkerboard’ like charge density waves are connected to superconductivity. In Ref. [25] this question has been addressed by means of scanning tunneling microscopy

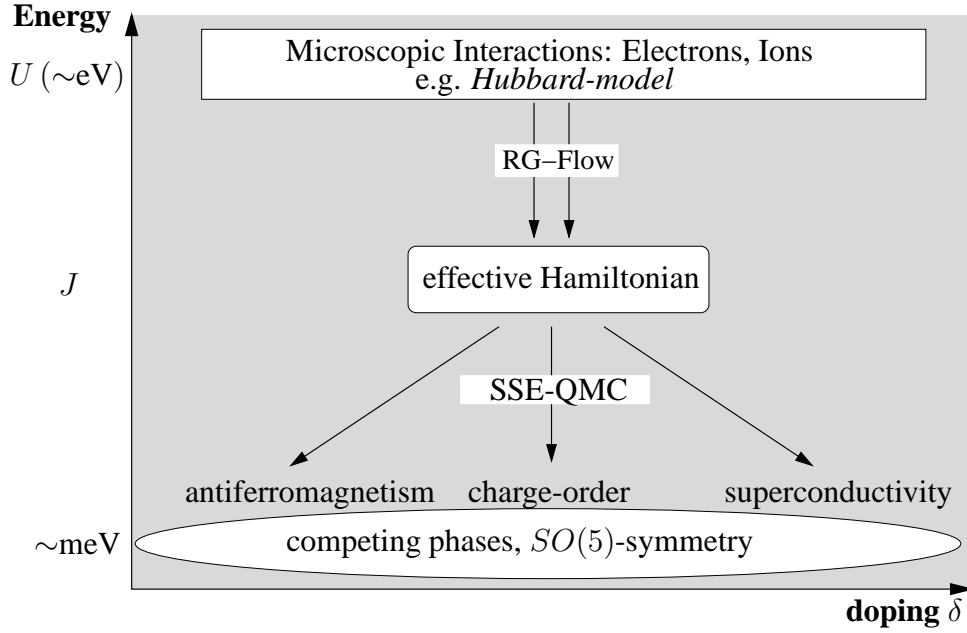


Figure 2: Overview of the energy scales relevant for a description of the high- $T_c$  superconductors. The microscopic interactions between electrons and ions are of the order of the Hubbard  $U$  ( $\approx 5$  eV). The interesting physics, however, takes place at considerably lower energies of the order of  $k_B T_c \lesssim 10$  meV. When starting, for example with the Hubbard-model, one may use a renormalization-group flow (CORE) to derive an effective Hamiltonian, where the interaction energies are of the order of  $100 - 150$  meV ( $\sim J$ ). This is the energy-scale of the  $t - J$  model as well as the projected- $SO(5)$  model. In the next step, one has to go down to even lower energies and increasing length-scales. In the present work this is performed using bosonic QMC simulations, which allow for temperatures of about  $J/20$  ( $5 - 7$  meV). In this regime, the different orders compete and the energetically most favorable one should be observable. If the  $SO(5)$ -theory is valid, the Hamiltonian, which describes the experimentally observed physics, does not need to be  $SO(5)$ -symmetric. But in the low energy regime the  $SO(5)$ -symmetry should be restored ‘dynamically’ close to a multi-critical point.

(STM) experiments. STM yields that the superconducting coherence peaks, ubiquitous in nearly-optimal doped tunneling spectra, disappear in favor of a local ‘checkerboard’ charge order. In order to include also charge-ordered phases, the projected- $SO(5)$  model needs to be extended.

As shown in chapter 5 the competition between charge order and superconductivity can be incorporated in the projected- $SO(5)$  model, by taking into account longer-ranged Coulomb interactions. These additional interactions arise naturally from the Contractor-Renormalization Group analysis [30] as well as from the  $SO(5)$ -theory [31].

The numerical investigation of the extended model starts with the calculation of the ground-state phase diagram [32]. As discussed in Sec. 5.3, the extended model indeed permits an explanation for the experimentally observed [25, 26, 27, 28, 29] charge ordered patterns. Next, motivated by the experimental results in Ref. [33], the doping dependence of the checkerboard order parameter is studied (Sec. 5.3.1). It is shown there, that in the extended projected- $SO(5)$  model the checkerboard order parameter displays maxima for filling factors of  $\delta_{hole} = 1/16, 1/8, 3/8$  and  $1/4$ . Moreover, at exactly these dopings the system shows Mott insulating behavior. This offers a natural explanation for the experimental results of Ref. [33], in particular, for the ‘magic numbers’  $\delta_{hole}$ . The subsequent sections are dedicated to the interplay of checkerboard and superconducting phases. First, the checkerboard to superconductor phase transition is studied (Sec. 5.3.2). An interesting interplay of superconductivity and checkerboard order as a function of temperature is reported in Sec. 5.3.2: Starting at  $T = 0$  from a SC-ground state the system shows, with increasing temperature, checkerboard order that again disappears upon further heating in favor of superconductivity. Such a ‘reentrance behavior’ upon increasing temperature is rare but not unique. It has been observed in the Ising antiferromagnet [34], as a Pomeranchuk effect in  $^3\text{He}$  and in a 2D hardcore-boson model [35].

In Sec. 5.3.3 data are presented, displaying another unusual phenomenon, namely the coexistence of charge order and superconductivity. When considering the model as a more generalized effective Hamiltonian, the charge bosons may be loosely interpreted as  $^4\text{He}$  atoms. Then the coexistence of these two at first glance diametrically opposed order parameters, i.e., charge order and SC order, can be interpreted in terms of a ‘supersolid’ behavior. The possible experimental detection of this phenomenon by Kim and Chan [36, 37] has recently led to renewed interest in this topic.

Finally, in chapter 6 the results are summarized.



# 1

## Stochastic-Series Expansion

---

In modern many body physics numerical simulations have proven to be an important tool to calculate macroscopic quantities (observables) originating from a microscopic model for some physical system. The numerical techniques that can be applied successfully to strongly interacting many body systems can be classified by their Ansatz: One path to follow, is to diagonalize the Hamiltonian. This route, at least in principle, allows to access any physical quantity, but due to the exponential growth of the Hilbert-space with the number of orbitals or lattice sites, only very small systems can be treated using diagonalization techniques. Several strategies to overcome this limitation have been developed. Some try to combine a small cluster with other clusters (CPT), couple a small cluster to bath sites or to reduce the Hilbert-space following a renormalization group scheme. For a review see Ref. [38]. Despite the restrictions, these techniques can be very useful to understand the physics on small length scales and at low temperatures. But on the other hand, if one is interested in questions that imply long distances or finite temperature, one has to follow a different direction. One possibility to avoid the disadvantages of the exact diagonalization Ansatz are *Quantum-Monte-Carlo* (QMC) simulations. Using QMC one does not directly diagonalize the Hamiltonian, but one tries to describe the physical many-body system by importance sampling of its many-body states. Quantum-Monte Carlo has proven to be an excellent tool for quantum many body physics since its first formulation in the eighties [39, 40]. In the following, a description of a very efficient member of these “importance-sampling methods”, namely the *Stochastic-Series Expansion*, is presented.

### 1.1 Formulation of the SSE

The main idea of all known types of QMC simulations is to map the  $d$ -dimensional quantum problem to  $d + 1$ -dimensional classical problem that can be solved using “standard”

Monte-Carlo. Starting point of most QMC simulations is the Trotter decomposition of the grand-canonical partition function:

$$Z = \text{Tr} \left( e^{-\beta \hat{H}} \right) = \text{Tr} \left( \prod_{l=1}^{L_\tau} e^{-\Delta\tau \hat{H}} \right), \quad (1.1)$$

where the imaginary time

$$\Delta\tau = \frac{\beta}{L_\tau}, \quad (1.2)$$

adds a further dimension to the system. Here  $\beta$  is the inverse temperature and  $L_\tau$  is the number of time slices. However, simulating systems in discrete imaginary time introduces a systematic error of the order of  $\mathcal{O}(\Delta\tau^2)$ . Thus, these methods require a delicate extrapolation of  $\Delta\tau \rightarrow 0$  ( $L_\tau \rightarrow \infty$ ). Furthermore these type of QMC simulations suffer from the purely local update schemes, which often do not sample all possible states efficiently, and as a consequence they show huge autocorrelation times. The last inconvenience can be avoided using a more recent class of QMC algorithms, the so called ‘‘cluster-algorithms’’ or ‘‘loop-algorithms’’ [41, 42, 43, 44, 45, 46, 47, 48, 49, 50]. These algorithms reduce in some cases the autocorrelation time by several orders of magnitude, as they use non-local cluster updates. Unfortunately this improvement does not come without some serious disadvantages, i.e., the loop-update scheme cannot be ported to any kind of second-quantized Hamiltonian: it is often a nontrivial task to find a loop formulation for a new Hamiltonian and some interactions cannot be incorporated in the loop scheme. These interactions can slow down the simulation considerably, because one has to add them to the loop as *a posteriori* acceptance probabilities after the construction of the loop. An other problem connected with some loop-update schemes occurs, when there is a high probability for one vertex to occupy the system, then the algorithms tends to freeze [41, 51].

A considerable improvement has been developed by A. Sandvik named the *Stochastic-Series Expansion* (SSE) (see Ref. [52] and references therein). The SSE is very efficient, applicable to a wide range of Hamiltonians and in principle exact. Starting point for the SSE is also the grand-canonical partition function, but in contrast to the Trotter decomposition, one chooses a convenient Hilbert base  $\{|\alpha\rangle\}$  and expands the partition function in a Taylor series.

$$Z = \sum_{|\alpha\rangle} \sum_{n=0}^{\infty} \frac{(-\beta)^n}{n!} \langle \alpha | \hat{H}^n | \alpha \rangle. \quad (1.3)$$

Sandvik has shown [52] that the statistical relevant powers are centered around

$$\langle n \rangle \propto \beta N_s, \quad (1.4)$$

where  $N_s$  is the number of orbitals (or lattice sites). Thus, one can truncate the power series after some  $L \propto \beta N_s$ , chosen such, that no systematic error is introduced by the

cutoff. In practice, one determines a suited cutoff length  $L$  during an initial thermalization phase: One simply starts with an arbitrary length  $L$  and whenever the actual cutoff length is exceeded one increases it by a factor of 1.1 – 1.2.

So far the first problem in evaluating Eq. (1.3), namely the infinite sum over all power, has been reduced to a numerically tractable one. But there still remains the sum over the complete Hilbert base  $\{|\alpha\rangle\}$ , that cannot be evaluated exactly, because the Hilbert space grows exponentially with the number of orbitals (or lattice sites). The SSE method evaluates the sum over all basis states by sampling them according to their physical relevance. Let  $\hat{H}$  be composed of a fixed number of elementary interactions involving one or two sites, for example chemical potentials and Hubbard terms, as on-site interactions or hopping terms and nearest neighbor interactions as off-site (two-site) interactions. In order to obtain a uniform notation, one rewrites the on-site interactions in terms of bond operators, e.g. a chemical potential term  $\mu \cdot \hat{n}(\text{site1}) + \mu \cdot \hat{n}(\text{site2})$  can be reformulated as  $\frac{1}{C}\mu \cdot (\hat{n}(\text{site1}) + \hat{n}(\text{site2}))$ , where the constant  $C$  assures that the sum over all new bond operators is equal to the sum of the initial on-site operators. Thus, now it is possible to write the Hamiltonian  $\hat{H}$  as a finite sum over bond operators  $\hat{H}_{b_i} = \sum_i \hat{H}_{b_i}$ , and the operator strings  $\hat{H}^n$  in Eq. (1.3) can be expressed in terms composed of

$$\prod_i^n H_{b_i}^{(a_i)}, \quad (1.5)$$

here  $a_i$  labels the operator type and  $b_i$  the bond on which the elementary interaction  $a_i$  (e.g. hopping or spin flip) acts on. For actual calculations it is convenient to have one fixed number of factors in the term (1.5). This can be accomplished by introducing ‘empty’ unit operators  $\mathbb{1}$  and Eq. (1.3) reads [53]:

$$Z = \sum_{\alpha} \sum_{\{S_L\}} \frac{(-\beta)^n (L-n)!}{L!} \langle \alpha | \prod_{i=0}^L (-\hat{H}_{b_i}^{(a_i)}) | \alpha \rangle, \quad (1.6)$$

where  $\{S_L\}$  denotes the set of all concatenations of  $L$  bond operators  $\hat{H}_b^{(a)}$  and  $n$  the number of non unit operators in  $S_L$ . Now one can sample  $(\alpha, S_L)$  accordingly to their relative weights with a Monte Carlo procedure, but only if it is ensured that the energy of each bond operator is non positive. This requirement is crucial, because in order to fulfill detailed balance one chooses the weight of each bond operator proportional to its negative matrix element. If a matrix element is however positive there are three possibilities, to ensure anyhow purely positive acceptance rates:

- If the positive matrix element is a diagonal matrix element, then one can simply add a constant to all diagonal matrix elements and thereby redefine the zero energy such, that all diagonal matrix elements are zero or negative.

- If the positive matrix elements can appear only pairwise (or in any even number), then one can simply alter the sign, without changing the system's physics, because in Eq. 1.3 it is the product of the matrix elements that contributes to the partition function.<sup>1</sup>
- If none of the two solutions above can be applied, one has to replace the acceptance probability  $p$  by  $p' = |p|$ , and calculate the expectation value of some observable  $\hat{O}$  as [40, 54, 55]:

$$\langle \hat{O} \rangle = \frac{\langle \hat{O} \text{sign}(p) \rangle}{\langle \text{sign}(p) \rangle}. \quad (1.7)$$

Unfortunately the  $\langle \text{sign}(p) \rangle$  tends exponentially to zero with increasing inverse temperature  $\beta$  and the number of sites (orbitals)  $N_s$ . As a direct consequence the computation time grows also exponentially with  $\beta \cdot N_s$ , what imposes restrictions on the accessible temperatures and system sizes.

## 1.2 Operator-Loop Update

In the preceding section the principle idea of the SSE has been reviewed. To apply the SSE to a physical problem one needs an effective update mechanism to sample the states  $|\alpha\rangle$  and operator sequences  $S_L$ . In the following the *Operator-Loop Update*, proposed by Sandvik [52] is reviewed. The Operator-Loop Update uses the so called world-line representation, here the x-axis represents the sites and the y-axis the propagation level  $l$  from  $l = 1$  to  $l = L$  (see Fig. 1.1 left). The update mechanism is separated in two fundamental steps, a diagonal and an off-diagonal update, that alter during a simulation. Starting point is an empty world-line lattice with an arbitrary start state  $|\alpha_0\rangle$  for all propagation levels (see Fig. 1.1). The update mechanism starts with a diagonal update, where for each propagation level one chooses one bond. If the bond operator, corresponding to the chosen bond is off-diagonal, the bond is left unchanged. If the bond operator is diagonal or empty, it is replaced by an empty or diagonal operator, with a probability satisfying detailed balance, i.e., a bond operator with lower energy is more likely to be kept or inserted than one with a higher energy. Following Sandvik we write a state at propagation level  $l$ :

$$|\alpha(l)\rangle = \prod_{i=1}^l \hat{H}_{b_i}^{(a_i)} |\alpha(0)\rangle, \quad (1.8)$$

---

<sup>1</sup>This procedure corresponds to a gauge transformation on all lattice sites with odd parity, thus this trick is restricted to non frustrated lattices.

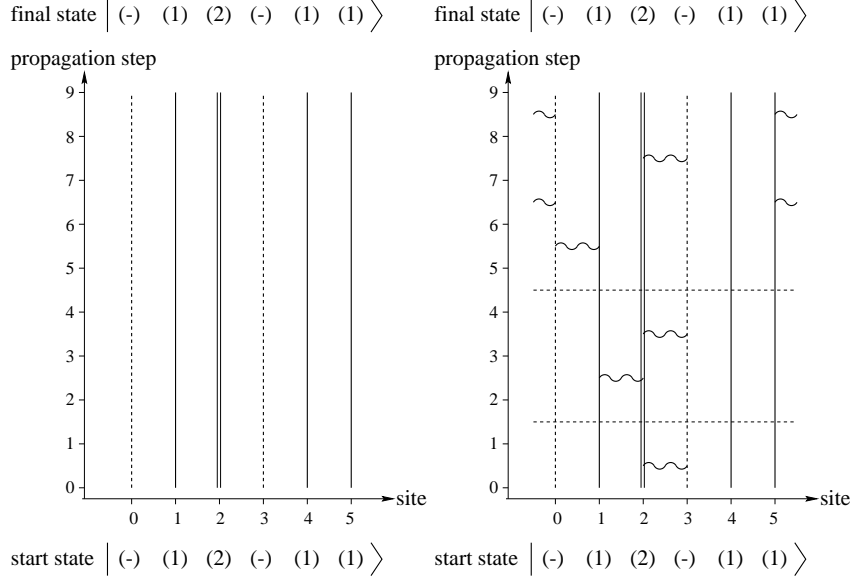


**Figure 1.1: Left:** Example of the world-line representation for a six site system, with two different particle types, before the first diagonal update. The initial state  $|-, 1, 2, -, 1, 1\rangle$  has been selected arbitrarily. The cutoff length  $L$  is chosen to be nine ( $L = 9$ ). **Right:** The same world-line representation as left, but now the diagonal update has been performed. In this example seven out of nine possible empty operators (i.e. unit operators) have been replaced.

The detailed balance conditions then read:

$$P(\hat{H}^{(0)}(l) \rightarrow \hat{H}^{(diag)}(l)) = \min\left(1, \frac{M\beta\langle\alpha(l) | \hat{H}_b^{(diag)} | \alpha(l)\rangle}{L - n}\right), \quad (1.9)$$

$$P(\hat{H}^{(diag)}(l) \rightarrow \hat{H}^{(0)}(l)) = \min\left(1, \frac{L - n + 1}{M\beta\langle\alpha(l) | \hat{H}_b^{(diag)} | \alpha(l)\rangle}\right). \quad (1.10)$$

In contrast to the diagonal update, the off-diagonal update introduces changes in the world-lines and thereby samples the states. In order to perform an off-diagonal update, one selects arbitrarily a world-line  $n_s$  and a propagation level  $l$ . Next, one inserts a local change to the world-line and propagates this change through the world-line space until the initial change is reached again, and the artificially introduced discontinuity is ‘healed’. The aim of constructing such a closed loop is to obtain a changed, but valid world-line web. To achieve this, one selects a propagation direction (up or down) and moves the initial change (‘loop head’) in that direction, until one reaches an interaction vertex. Now one has to decide how to go on. The loop head can go straight on, or if the Hamiltonian contains an appropriate interaction it can turn, jump or bounce. The straight path is always

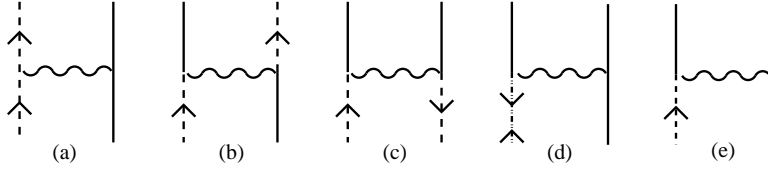


Figure 1.2: Possible paths in the Operator-Loop Update: (a) Path straight: always possible because the resulting vertex is diagonal. (b) Path jump: possible if Hamiltonian contains hopping or site interchange terms. (c) Path turn: can occur in the construction of the loop, if the Hamiltonian has a term creating or annihilating two particles on adjacent sites. (d) Bounce path: Here the loop head simply changes its direction, in some cases this can enlarge the autocorrelation time, because the choosing the bounce path can result in an unchanged vertex. (e) Loop head ends.

possible, because it is equivalent to the insertion of a diagonal vertex. There is also a fifth possibility: The loop head can get stuck. In the latter case one has to restart the loop from the initial world-line  $n_s$  and propagation level  $l$  and move the loop head in the opposite direction until the loop gets stuck again, or the initial discontinuity is reached and healed. The selection of a path through a vertex has to fulfill detailed balance. Thus, an interaction vertex with lower energy is more likely to be inserted than one with a higher energy. If the outgoing leg is chosen, the loop head moves along the world-line in the corresponding direction, until it reaches the next vertex, where again a new path has to be selected. This process has to be repeated until the loop head returns to its initial position  $(n_s, l)$  and a change is applied also to the ‘dangling’ end of the world-line. This closes the loop and the propagation of the loop head is stopped. The world-line web contains now only valid world-lines, in the sense, that there is no change in a world-line, that is not mediated by some elementary bond operator  $\hat{H}_b^{(a)}$  represented by a non-diagonal vertex. In the limit of high temperatures a third update step can be useful: From Eq. (1.4) it becomes obvious, that the world-line web of a simulation at high temperatures, i.e.,  $\beta \rightarrow 0$ , will contain mostly empty bond operators, what decreases the efficiency of the off-diagonal update. Thus, it takes longer to sample the states  $|\alpha\rangle$ . One can compensate this by adding a free world-line update to the simulation, which changes the occupation of entire world-lines, if they are not connected to any vertex.

Finally, one has to proof the ergodicity of the Operator-Loop Update mechanism, i.e., that starting the simulation with a given  $|\alpha\rangle$  the update mechanism can reach any  $|\alpha'\rangle \in \mathcal{H}_\alpha$ , where  $\mathcal{H}_\alpha$  denotes the basis of the Hilbert space. Recalling Eq. (1.8), it is obvious that any  $|\alpha'\rangle = |\alpha(l)\rangle$  can be sampled, if a finite operator sequence can be composed from

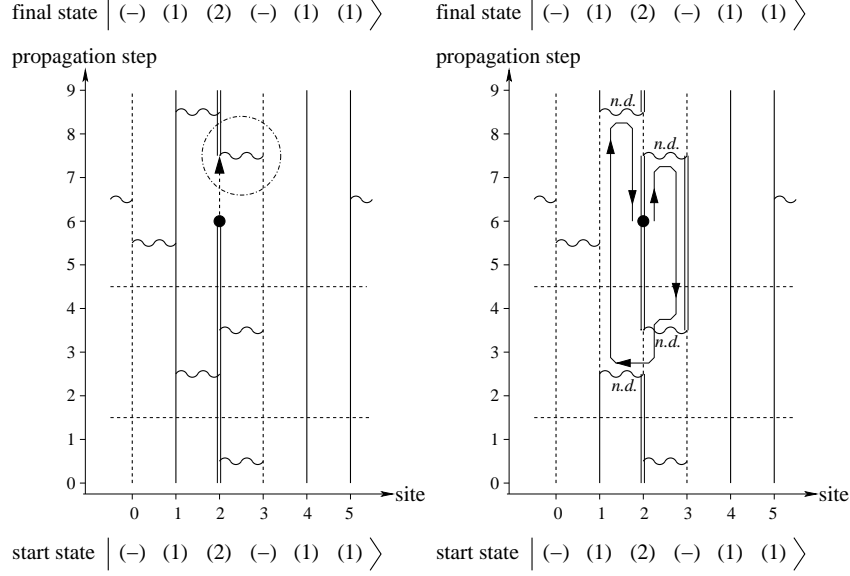


Figure 1.3: Example for the construction of a loop update. **Left:** Start of the off-diagonal update, on world-line  $n_s = 2$  a local change (annihilation of a particle of type 2) is inserted at propagation level  $l = 6$  and the chosen direction is “up”. The loop head reaches the first interaction vertex. **Right:** Now the loop reached its starting position after a replacing four diagonal vertices by a sequence of ‘turn’, ‘jump’, ‘turn’, ‘turn’ off-diagonal vertices. In the last step the initial discontinuity is removed. (Pictures by A. Dorneich [56])

the terms forming the Hamiltonian, such that any  $|\alpha\rangle$  can be connected via Eq. (1.8) with  $|\alpha'\rangle$ :

$$|\alpha'\rangle = \prod_i^{L_{os}} \hat{H}_{b_i}^{(a_i)} |\alpha\rangle. \quad (1.11)$$

Thus, if it is ensured that the length of longest necessary operator sequence ( $\max(L_{os})$ ) is smaller than the cutoff length  $L$  the update is ergodic. In an actual simulation this can be ensured by choosing  $L$  during the thermalization phase such that it is big enough.

**Further Improvements of the Operator-Loop Update** As already mentioned above the bounce path can undo the last change made to the world-line web. If such a bounce path has a significant probability, it can slow down the simulation considerably. Two attempts have been developed to avoid the bounce path: If the matrix elements of all bounce vertices can be made equal, for example by shifting the energy of the diagonal matrix elements, the bounce path can be eliminated by shifting their energy to zero. This has very favorable effects on the systems dynamics, since now all vertices of the loop accomplish a change in the world-lines. A more general Ansatz has been proposed by Sandvik [57],

called the *Directed-Loop Update*. Whereas in the Operator-Loop Update the heat-bath algorithm is used for propagating the path between connected vertices, in the *Directed-Loop Update* a more general set of equations have to be satisfied, in order to ensure that the chosen path obeys detailed balance. This set of equations has an infinite number of solutions and in principle one can select the solution that minimizes the probability for the bounce path, but these equations have to be solved for each model that one wishes to simulate. Moreover, finding an optimum solution is often a nontrivial task. The implementation that has been enhanced significantly during this thesis, does not require the solution of the directed-loop equations. The resulting disadvantage is, from our point of view, overcompensated by the fact, that the implementation of the SSE used and further developed within this thesis can simulate, within the restrictions discussed above, any bosonic-quantum model [22].

### 1.3 Accessing Physical Observables

Simulating a physical system is only half of the job: To achieve a better understanding of the physical model under consideration it is essential to have efficient access to the observables during a simulation. In the following we will discuss briefly some of these measurements, in order to exploit the general concept.

#### 1.3.1 Calculating Expectation Values

Suppose we are interested in the expectation value of some observable  $\langle \hat{O} \rangle$ . Starting from its definition,

$$\langle \hat{O} \rangle = \frac{1}{Z} \text{Tr} \left( \hat{O} Z \right), \quad (1.12)$$

one easily rewrites  $\langle \hat{O} \rangle$  in terms of the SSE formulation:

$$\langle O \rangle = \frac{\sum_{\alpha, n, S_n} O(\alpha, n) W(\alpha, S_n)}{\sum_{\alpha, n, S_n} W(\alpha, S_n)}, \quad (1.13)$$

where  $W(\alpha, S_n)$  is defined as:

$$W(\alpha, S_n) = \frac{(-\beta)^n}{n!} \langle \alpha | \prod_{i=1}^n \hat{H}_{b_i}^{(a_i)} | \alpha \rangle \quad (1.14)$$

Often such an operator  $\hat{O}$  is an elementary interaction in the Hamiltonian,

$$\langle \hat{O} \rangle = \langle \hat{H}^{(a)} \rangle, \quad (1.15)$$



than  $\hat{O}$  can be accessed very efficiently by simply counting the number ( $N^{(a)}$ ) of interaction vertices  $\hat{H}^{(a)}$ :

$$\langle \hat{O} \rangle = -\frac{1}{\beta} \langle N^{(a)} \rangle. \quad (1.16)$$

Thus, the energy  $E$  of a system can be measured as:

$$\langle \hat{E} \rangle = -\frac{1}{\beta} \langle n \rangle, \quad (1.17)$$

where  $n$  is the number of non unit operators. It is straightforward to access also more complicated observables, that are not directly given by elementary interactions in the Hamiltonian, but are connected to them, e.g. the heat capacity  $C_V$ :

$$C_V = \langle n^2 \rangle - \langle n \rangle^2 - \langle n \rangle \quad (1.18)$$

Sandvik derived very efficient expressions, for a wide range of static observables. A more complete description can be found in Ref. [58].

### 1.3.2 Accessing Correlation Functions

#### Mathematical Formulation

The observables mentioned in Sec. 1.3.1 serve to describe important thermodynamic variables. However, often one is interested also in static- or dynamic-correlation functions and susceptibilities. When recalling the construction of the loop in Sec. 1.2, it is obvious that the propagation level  $l$  in the loop-operator update plays an analogous role to the imaginary time in a standard path integral. The exact relation can be obtained Taylor-expanding the time dependent correlation function [59]:

$$C_{i,j}(\Delta\tau) = \langle e^{\Delta\tau\hat{H}} \hat{O}_i e^{-\Delta\tau\hat{H}} \hat{O}_j \rangle \quad (1.19)$$

$$= \frac{1}{Z} \sum_{\alpha, n, m} \frac{(\Delta\tau - \beta)^n (-\Delta\tau)^m}{n! m!} \langle \alpha | \hat{H}^n \hat{O}_i \hat{H}^m \hat{O}_j | \alpha \rangle, \quad (1.20)$$

The indices  $i$  and  $j$  mark the operator type, for convenience the site labels  $r_1, r_2$  of  $C_{i,j}(\Delta\tau, r_1, r_2)$ ,  $\hat{O}_i(r_1)$  and  $\hat{O}_j(r_2)$  are dropped. In the next step one changes to a summation over index sequences and sums over all positions of  $\hat{O}_j$  in the operator product:

$$C_{i,j}(\Delta\tau) = \frac{1}{Z} \sum_{\alpha} \sum_{l=0}^L \sum_{m=0}^l \sum_{\{S_n\}} \frac{(-\Delta\tau)^m (\Delta\tau - \beta)^{l-m}}{(l-m)! m!} \times \\ \langle \alpha | \prod_{k=m+1}^L \hat{H}_{b_k}^{(a_k)} \hat{O}_i \prod_{h=1}^m \hat{H}_{b_h}^{(a_h)} \hat{O}_j | \alpha \rangle \quad (1.21)$$

Comparing Eq. (1.21) with Eq. (1.14) and replacing  $\hat{O}_i$  by its eigenvalue  $o_i(\alpha(l))$  ( $\langle \hat{O}_i | \alpha(l) \rangle = o_i(\alpha(l)) | \alpha(l) \rangle$ ), and hereby restricting ourselves to diagonal operators, leads to:

$$C_{i,j}(\Delta\tau) = \left\langle \sum_{l=0}^{L-1} \sum_{m=0}^l \frac{\Delta\tau^m (\beta - \Delta\tau)^{l-m}}{\beta^l} \frac{(l-1)!}{(l-m)! m!} o_i(l) o_j(l+m) \right\rangle_W. \quad (1.22)$$

The index  $W$  indicates, that the eigenvalues  $o_i(\alpha(l))$  must be sampled according to Eq. 1.14, what can be accomplished by simply summing them during the construction of a loop. Of course  $\hat{O}_i$  and  $\hat{O}_j$  are not necessarily diagonal, but also off-diagonal correlation functions can be calculated. Choosing  $\hat{O}_i = \hat{H}_{b_i}^{(a_i)}$  and  $\hat{O}_j = \hat{H}_{b_j}^{(a_j)}$  one obtains:

$$\langle \hat{H}_{b_i}^{(a_i)} \hat{H}_{b_j}^{(a_j)} \rangle(\Delta\tau) = \left\langle \sum_{m=0}^{L-2} \frac{(\Delta\tau)^m (\beta - \Delta\tau)^{L-m-2}}{\beta^L} \frac{(L-1)!}{(L-m-2)! m!} N(i, j; m) \right\rangle_W, \quad (1.23)$$

where  $N(i, j; m)$  is the number of times the operators  $\hat{H}_{b_i}^{(a_i)}$  and  $\hat{H}_{b_j}^{(a_j)}$  appear in the sequence  $S_n$  separated by  $m$  positions in the operator string  $S_n$ . From Eq. (1.23) it is straight forward to calculate also the susceptibility  $\chi_{i,j}$ ,

$$\chi_{i,j} = \int_0^\beta \langle \hat{O}_i(\tau) \hat{O}_j(0) \rangle d\tau. \quad (1.24)$$

Integrating  $\langle \hat{O}_i(\tau) \hat{O}_j(0) \rangle$  from 0 to  $\beta$  gives the Kubo integral. In the diagonal case the integral reads:

$$\int_0^\beta \langle \hat{O}_i(\tau) \hat{O}_j(0) \rangle d\tau = \left\langle \frac{\beta}{(n+1)n} \left[ \left( \sum_{l=0}^{L-1} o_i(l) \right) \left( \sum_{l=0}^{L-1} o_j(l) \right) + \sum_{l=0}^{L-1} o_i(l) o_j(l) \right] \right\rangle_W, \quad (1.25)$$

where the cyclic periodicity of the propagated states has been used. For the product  $\langle \hat{H}_{b_i}^{(a_i)}(\tau) \hat{H}_{b_j}^{(a_j)}(0) \rangle$ , considered above, the integral becomes:

$$\int_0^\beta \langle \hat{H}_{b_i}^{(a_i)}(\tau) \hat{H}_{b_j}^{(a_j)}(0) \rangle d\tau = \frac{1}{\beta} \left\langle \sum_{m=0}^{L-2} N(i, j; m) \right\rangle_W \quad (1.26)$$

### Including the Measurement of $C_{i,j}$ in the Update Scheme

Whereas the formulation of the measurement for a dynamic single-particle correlation functions is not difficult in a mathematical language, performing an actual measurement

poses some difficulties in the framework of the *SSE*. Measuring off-diagonal correlation functions, demands that non local changes have to be inserted in the world-lines. These insertions must sample all the distances in real space  $\Delta r = r_1 - r_2$ , as well as in the propagation dimension ( $\Delta l = l_1 - l_2$ ), and detailed balance must still be satisfied. When recalling the ‘off-diagonal’ update, as displayed in Fig. 1.3, one immediately notices, that the same requirements are already fulfilled by the *SSE* off-diagonal update mechanism. Hence  $C_{i,j}(\tau)$  can be recored during the construction of a loop. An example is given in Fig. 1.4. The matrix elements, i.e., the correlation functions  $C_{i,j}(r, \Delta l)$ , are

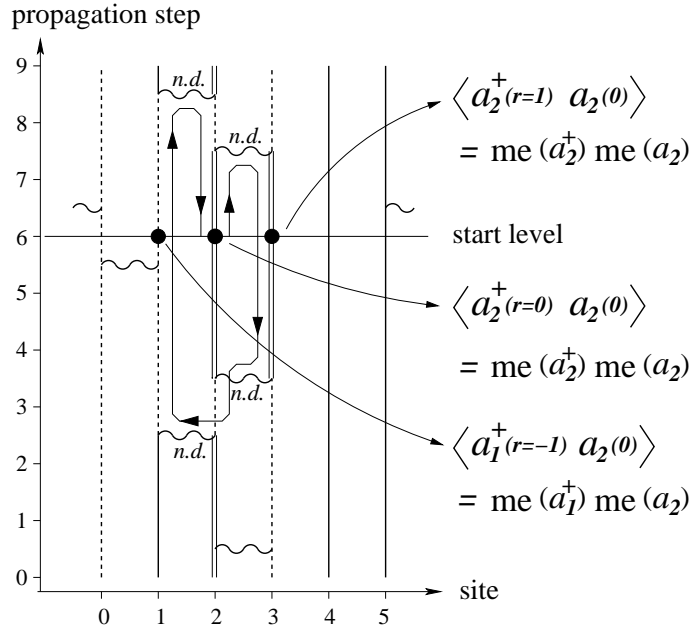


Figure 1.4: Recording of of the Green's function  $\langle a_2^\dagger(r, \Delta l) a_2(0, 0) \rangle$  and  $\langle a_1^\dagger(r, \Delta l) a_2(0, 0) \rangle$  during the construction of the loop as explained in Fig. 1.3.  $r$  is the distance between to sites (or world-lines) and  $\Delta l$  a propagation level distance. ‘ $me(a_t^{(\dagger)})$ ’ denotes the matrix element for annihilating (creating) a particle of type  $t$ .

recorded like usual Monte Carlo variables. But for a physical interpretation one mostly prefers a representation of  $C_{i,j}$  as function of momentum  $\vec{k}$  and energy  $\omega$ . Hence in a first step a Fourier transformation is necessary in order to obtain  $C_{i,j}(\vec{k}, \Delta l)$ , and in the next step formula (1.23) or (1.22), depending on the type of the operators, converts  $C_{i,j}(\vec{k}, \Delta l)$  to  $C_{i,j}(\vec{k}, \tau)$ . Finally, an inverse Laplace transformation yields  $C_{i,j}(\vec{k}, \omega)$ . The inverse Laplace transformation imposes some substantial difficulties, because  $C_{i,j}(\vec{k}, \tau)$  can only be calculated for discrete  $\tau = n \cdot \Delta\tau \mid n \in \mathbb{N}$ , further  $C_{i,j}(\vec{k}, n_1 \Delta\tau)$  is correlated with  $C_{i,j}(\vec{k}, n_2 \Delta\tau)$ . Different techniques can be used: Either one refers to

the *Maximum-Entropy Method* [60, 61] or to a recently proposed generalization of the *Maximum-Entropy Method* [62].

### Recent developments

So far measurements of correlation functions of two off-diagonal operators, that are not contained in the Hamiltonian have not been discussed. In principle, such a measurement is possible, but it cannot be recored during the construction of a loop, because inserting a local change, that cannot be expressed as a product of the elementary interactions in the Hamiltonian contradicts detailed balance. To the author's knowledge such a measurement has not been reported so far. One escape is to introduce for each measurement the off-diagonal operators under consideration and after the measurement one immediately removes them by the insertion of their inverse operators. Effectively this corresponds to adding the unit operator to the operator string. Thus, the physics of the system is not changed by this procedure. However, this procedure has to be performed after each loop, for all distances and propagation levels. Therefore, the advantage of measuring the correlation functions on the run is lost and the CPU-time for an entire simulation will increase significantly.

A more severe problem is, that the measurement of off-diagonal correlation functions has been restricted to 'one-particle correlation functions' so far. In principle also two-particle functions can be measured like described above, but then one has to insert and remove four operators instead of two.

However, the two-particle functions can also be recorded during the construction of a loop. For this purpose the concept presented in Sec. 1.3.2 can be extended to two-particle functions, at least in principle. But again one is restricted to the case where the operators  $\hat{O}_i$  are fundamental operators in the Hamiltonian  $\hat{H}_i^{(a_i)}$ . The problem occurs during an actual simulation: A measurement of some correlator  $C_{i,j,k,h}(r_1, r_2, \Delta l)$  is only possible if the loop-head passes each position  $(r_1, l_1)$  and  $(r_2, l_2)$  in the world-line space at least twice during the construction of the loop and if the four vertices changed at these positions during the loop correspond to the operators  $i, j, k$  and  $h$  that one wants to measure. The probability for the construction of such loops is rather low. Therefore, it seems more favorable to accept the disadvantage of introducing an extra measurement step and perform the measurements of the off-diagonal two-particle correlation functions after the construction of the loop.

## 1.4 Conclusions

The *Stochastic-Series Expansion* (SSE) in the Operator-Loop Update formulation is a very useful method for the simulation many particle problems on lattices. The SSE is in principle exact and allows to access a wide range of observables. Due to its conceptual simplicity it can be implemented very efficiently. A comparison with other methods can be found in [63]. A more vivid proof of the algorithm's capabilities is, that within this thesis it has been made possible to simulate for the first time a rather complicated hardcore boson model with more than 10000 lattice sites (see Chap. 4). Using these new possibilities in the investigation of many particle models allows, to extrapolate the results to the thermodynamic limes with an unprecedented precision.



# 2

## Effective Models

---

Solid-state physics aims at an understanding of the experimentally observed properties, based on a microscopic (i.e. quantum) description of the solid. This, however, in practice requires simplifications which lead to a model. One of the most popular models in the field of magnetism connected with localized and usually strongly interacting orbitals is the *Hubbard-model* [64]. Here the microscopic interactions in the solid are placed on a lattice model, containing electron hopping and on-site Coulomb interactions of the electrons. The second-quantized Hubbard Hamiltonian reads:

$$\hat{H}_{Hub} = \sum_{\langle i,j \rangle \sigma} t_{i,j} c_{i,\sigma}^\dagger c_{j,\sigma} + \sum_i U_i \hat{n}_i (\hat{n}_i - 1) \quad (2.1)$$

Here  $i, j$  are site indices,  $\langle i, j \rangle$  denotes the sum over pairs of neighbored sites,  $\hat{n}_i$  is the particle number operator on site  $i$ , and  $c_{i,\sigma}^{(\dagger)}$  annihilates (creates) a particle on site  $i$  with spin  $\sigma$ . The *Hubbard-model* has attracted considerable attention, especially after the discovery of the high-temperature superconductors in 1986 [4]. Despite its conceptual simplicity the *Hubbard-model* still awaits an exact solution in two and three dimensions, and quantitatively understanding the physics of the *Hubbard-model* is still a major challenge. This holds especially in the ‘strong-coupling’ case ( $U > t$ ), where typically the kinetic energy is of the same magnitude as the correlation energy and, therefore, perturbation theory fails. Various numerical techniques have been employed, especially Quantum-Monte-Carlo simulations [11, 65, 66]. But the ‘notorious sign problem’, considerably limits the system sizes and temperature ranges. This holds especially for doped systems, away from half filling ( $\langle \hat{n} \rangle \neq 1$ ). Unfortunately, the fermionic sign problem grows exponentially with inverse temperature  $\beta$  and the system size  $N_s$ . One ‘way-out’ from these difficulties is offered by a real-space normalization group technique, i.e., the Contractor-Renormalization group technique, which reformulates the physics of Eq. (2.1) in the subspace of the low-lying excitations of the underlying model. This procedure

yields an effective model, which in a subsequent step can be treated very efficiently by means of a bosonic *Quantum-Monte-Carlo* simulation (see Chap. 1).

## 2.1 Constructing an effective Hamiltonian via the Contractor-Renormalization Group Procedure

When aiming at an effective low-energy Hamiltonian one usually refers to renormalization group (RG) techniques, that integrate out the high energy degrees of freedom iteratively and thereby extract the low-energy physics. These iterations can be associated with an RG-flow, that may bring the system to a fix point. An improvement of this technique is the so called *Contractor-Renormalization Group* (CORE) [67, 68]. The CORE technique supplements the real-space renormalization group approach with a so called ‘contraction’. In the usual real-space renormalization group scheme, one first performs a coarse graining, i.e. one divides the infinite lattice into smaller cells, called plaquettes, that can be diagonalized exactly. After the diagonalization, one restricts to the lowest  $m$  eigenstates, and tries to find an approximation for the original Hamiltonian by coupling the plaquettes using the  $m$  eigenstates as a new basis. The difficulty is to find the matrix elements, for example to describe a quasiparticle propagation from one plaquette to another. Different ways of applying this method have been developed, for a review it is referred to Refs. [69, 70, 71].

In addition to the above procedure, the CORE requires a further diagonalization step. This ‘extra’ diagonalization ensures that the lowest  $m^r$  eigenstates of the resulting super cell Hamiltonian have the same eigenenergies as the initial (original) Hamiltonian on the same super cell, where  $r$  denotes the number of plaquettes the super cell is composed of. An example with  $r = 2$  is displayed in Fig. 2.1.

Performing a CORE calculation, for example, based on the *2D-Hubbard-model*, one starts dividing the sub-lattice in  $r$  equal blocks  $G_i$  (plaquettes), where the index  $i$  labels the plaquettes. Next, one diagonalizes the Hamiltonian for such a plaquette and retains only the lowest  $m$  eigenstates  $|\nu_0\rangle_i - |\nu_{m-1}\rangle_i$ , as in the usual real-space RG. In a second diagonalization, the whole sub-lattice has to be diagonalized. This is a crucial point, because it poses severe restrictions to the allowed maximum plaquette-size as well as to the number of plaquettes forming the sub-lattice.

The sub-lattice eigenstates  $|\epsilon_p\rangle$  can be written in terms of the product basis of all  $n$  plaquette-eigenstates, i.e.:

$$|\epsilon_p\rangle = \sum_{\alpha=0}^{n^r-1} v_{\alpha,p} |\nu_{\alpha_0}\rangle_0 \otimes |\nu_{\alpha_1}\rangle_1 \otimes \dots \otimes |\nu_{\alpha_{r-1}}\rangle_{r-1}, \quad 0 \leq \alpha_i < n, \quad \forall i \leq r. \quad (2.2)$$



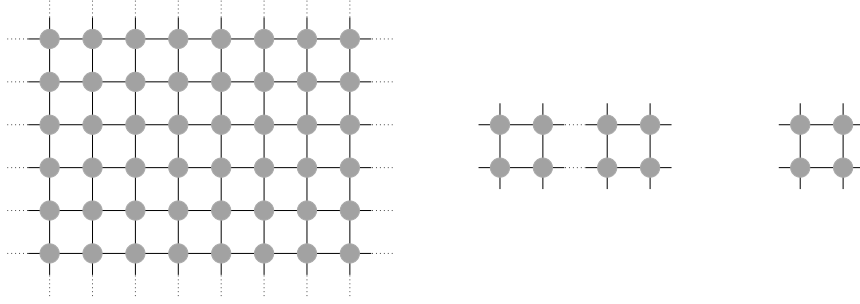


Figure 2.1: The infinite lattice (left), the supercell (middle), here composed out of  $r = 2$  plaquettes and a single plaquette (right). An infinite range supercell ( $r \rightarrow \infty$ ) would again lead to the infinite lattice, as well as an infinite plaquette size.

Next, one applies a suited projector  $P$  to the sublattice eigenstates, thereby the Hilbert space is reduced to  $m^r$  dimensions:

$$\begin{aligned}
 |\tilde{\epsilon}_p\rangle = P|\epsilon_p\rangle &= \sum_{\alpha=0}^{n^r-1} v_{\alpha,p} \sum_{j=0}^{m-1} |\nu_j\rangle_0 \langle \nu_j|_0 | \nu_{\alpha_0}\rangle_0 \otimes \sum_{j=0}^{m-1} |\nu_j\rangle_1 \langle \nu_j|_1 | \nu_{\alpha_1}\rangle_1 \otimes \\
 &\dots \otimes \sum_{j=0}^{m-1} |\nu_j\rangle_{r-1} \langle \nu_j|_{r-1} | \nu_{\alpha_{r-1}}\rangle_{r-1} \\
 &= \sum_{\alpha=0}^{m^r-1} v_{\alpha,p} | \nu_{\alpha_0}\rangle_0 \otimes | \nu_{\alpha_1}\rangle_1 \otimes \dots \otimes | \nu_{\alpha_{r-1}}\rangle_{r-1},
 \end{aligned} \tag{2.3}$$

where  $0 \leq \alpha_i < m$ ,  $\forall i \leq r$ . The projected Basis  $\{|\tilde{\epsilon}_p\rangle\}$  can next be orthogonalized, and the effective supercell Hamiltonian reads in the new orthonormal basis  $|\theta_\gamma\rangle$

$$\hat{H}_{eff} = \sum_{\gamma=0}^{m^r-1} |\theta_\gamma\rangle \epsilon_\gamma \langle \theta_\gamma|, \tag{2.4}$$

where the  $\epsilon_\gamma$  denote the supercell eigenenergies. This procedure can be applied in a subsequent step to the obtained effective Hamiltonian, corresponding to the first iteration step in an RG-sense. In order to study the CORE renormalization flow, the CORE method has been applied to the spin- $\frac{1}{2}$  Heisenberg chain by Morningstar and Weinstein [68]. They divide the lattice into three site blocks and carry out a range two ( $r = 2$ ) calculation. In the case of the Heisenberg spin chain the effective Hamiltonian is self-similar under the CORE procedure, and an analytic expression for the ground state energy is found. This permits to iterate the CORE algorithm until the ground-state energy converges. Morningstar and Weinstein obtain an accuracy of the ground-state energy per site of about

99% in comparison to the exact Bethe-Ansatz solution [72]. Also the antiferromagnetic (AF) properties are recovered by their calculation, i.e. no long-range AF order, but a massless spectrum.

Employing this method to the *Hubbard-model*, one first has to define the basic plaquette and the supercell. The resulting effective Hamiltonian will then describe the physics on a coarse-grained lattice, where each lattice point represents an original plaquette. In order to couple as much clusters as possible, one may be tempted to chose a dimer as plaquette. This Ansatz has been followed to construct effective Hamiltonians for spin-ladder systems [73, 74]. However, there is no hole pair binding for the *Hubbard-model* on a dimer, which is an important ingredient for superconductivity. Further, if one wishes to capture the experimentally observed the d-wave symmetry [6] of the hole-pair wave function, the basic cluster to start from, must at least have four-fold rotational symmetry. Hence the cluster chosen here is a four site ( $2 \times 2$ ) plaquette. By this choice the number of coupled clusters  $r$  is immediately restrict to be equal to two. Already selecting  $r = 3$  bears substantial numerical difficulties, because one would have to diagonalize a 12 site *Hubbard-model* in multiple geometric configurations, which is on the edge of what can be done, with the available computer resources. Altman and Auerbach carried out this so called ‘Range 2 CORE’ ( $r = 2$ ) for the *Hubbard-model*. The exact diagonalization of one single plaquette is straightforward, and one obtains the spectrum and the wavefunctions. The spectrum obtained by Altman and Auerbach is depicted in Fig. 2.2. Fortunately, the

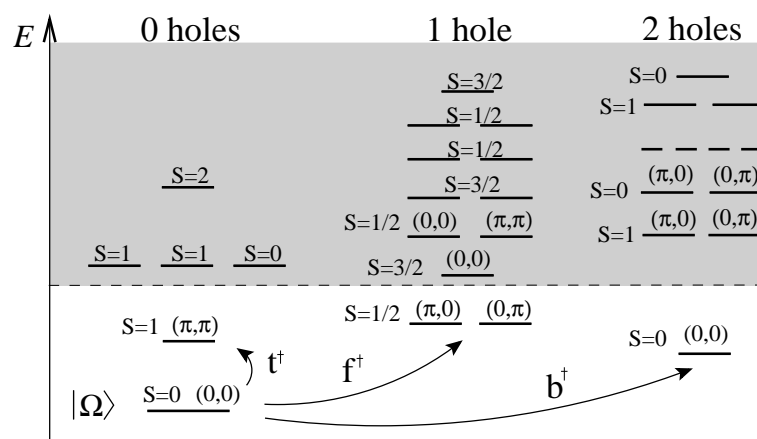


Figure 2.2: Low-energy spectrum of the 4 site Hubbard-model. The Eigenstates are labeled by their spin quantum number and by the associated plaquette momenta.

low-lying states have a bosonic character (total spin  $S = 0$  or  $S = 1$ ), hence restricting to the lowest five states ( $m = 5$ ) for each plaquette, will yield an effective Hamiltonian, that

contains only (hardcore-) bosons. As already stated above, such an effective Hamiltonian can be studied very efficiently using QMC.

In the following paragraphs the five lowest eigenstates of a single plaquette are discussed.

**The Ground State** The plaquette ground state of four site *Hubbard-model* at half filling  $|\Omega\rangle_i$  can be understood in the real-space representation as the resonating valence bond (RVB) ground state of the Heisenberg model, plus small contributions from doubly occupied sites. The product state of the plaquette ground states  $|\Omega\rangle_i$  defines the new vacuum state  $|\Omega\rangle$ ,

$$\prod_i |\Omega\rangle_i = |\Omega\rangle. \quad (2.5)$$

The second quantized operators  $b_i^\dagger$  and  $t_{\alpha,i}^\dagger$  connect the vacuum to the lowest lying eigenstates as shown in Fig. 2.2.

**The Triplet State** The  $S = 1$  triplet states describe the lowest lying magnon states, they are given by:

$$t_{\alpha,i}^\dagger = \frac{\hat{P}}{\sqrt{Z_t}} \sum_{\vec{Q},s} c_{\vec{Q},s}^\dagger \sigma_{s,s'} c_{\vec{Q}+(\pi,\pi),s'} |\Omega\rangle_i = |t_\alpha\rangle_i, \quad \alpha = x, y, z, \quad (2.6)$$

where the operator  $\hat{P}$  performs a partial Gutzwiller projection ( $\hat{P}(U/t)$ ),  $\sqrt{Z_t}$  normalizes the wave function  $|t_\alpha\rangle_i$  and the plaquette electron operator is defined as:

$$c_{\vec{Q},s}^\dagger = \frac{1}{2} \sum_{\eta} e^{i\vec{Q}\cdot\eta} c_{\eta,s}^\dagger. \quad (2.7)$$

The sum over  $\eta$  covers all sites on a plaquette, here the plaquette index has been dropped for convenience. These magnons have plaquette momentum  $\vec{Q} = (\pi, \pi)$  and their excitation energy is close to the superexchange energy  $J \approx 4t^2/U$ . Thus, a long-range correlation between the triplet states corresponds to long-range AF order in the original *Hubbard-model*. In Landau theory the formation of this AF state has a formal equivalence to Bose condensation. In this sense the triplets condense into the long-range AF ordered state, however, there is no transport associated with this condensation. From this point of view the condensation picture fails.

**The Hole Pair State** The operator  $b_i^\dagger$  creates a hole pair with internal d-wave symmetry, with respect to the vacuum:

$$b_i^\dagger |\Omega\rangle_i = \frac{\hat{P}}{\sqrt{Z_b}} c_{(0,0)\uparrow}^\dagger c_{(0,0)\downarrow} |0\rangle \quad (2.8)$$

As shown in [23] the two holes do not disintegrate into two fermions. The binding energy is generated dynamically on the lattice, because a correlated movement is energetically more favorable. A simplified sketch is depicted in Fig. 2.3. Binding hole pairs have been reported for a multitude of lattices, starting with the four-site plaquette [75, 76, 77]. In larger clusters hole binding has been observed up to 6 holes [78].

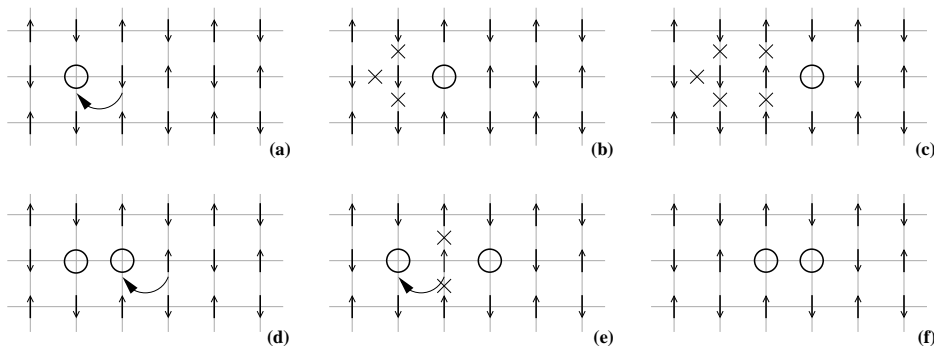


Figure 2.3: Sketch of the correlated movement of two holes for a 2-D Hubbard-model close to half filling. The upper three figures (a-c) display the movement of a single hole in an AF background. The arrows symbolize the electronic spins. If only a single hole moves, the system gains the hopping energy  $t$  but the AF order of the electronic spins is destroyed, this corresponds to an energy penalty of three times the superexchange energy  $J \approx 4t^2/U$ . The frustrated bonds are indicated by the three crosses in Fig. (b). If the hole keeps on moving it creates further two frustrated bonds (c). In this picture the movement of a single hole is connected with an energy penalty that grows linear with the distance covered by the hole. In contrast to that, the two holes in the lower row (d-f) form a ‘Cooper pair’ and can move in the plain, without such an energy penalty, as long as the Cooper pair does not disintegrate.

## 2.2 The effective Hamiltonian

The model constructed using a range 2 CORE, contains bilinear and quartic (interaction) terms of the quasiparticles discussed above [23]:

$$\hat{H}_{CORE} = \hat{H}_b + \hat{H}_t + \hat{H}_{b,t}^{int} \quad (2.9)$$

The bilinear terms read:

$$\hat{H}_b = (\Delta_c - 2\mu) \sum_i b_i^\dagger b_i - J_c \sum_{\langle i,j \rangle} (b_i^\dagger b_j + h.c.), \quad (2.10)$$

$$\hat{H}_t = \Delta_s \sum_i t_{\alpha,i}^\dagger t_{\alpha,i} + \sum_{\langle i,j \rangle} \left[ J_s (t_{\alpha,i}^\dagger t_{\alpha,j} + h.c.) + J_{ss} (t_{\alpha,i}^\dagger t_{\alpha,j}^\dagger + h.c.) \right]. \quad (2.11)$$

The higher order interaction terms are:

$$\begin{aligned} \hat{H}_{b,t}^{int} = & V_c \sum_{\langle i,j \rangle} \hat{n}_{c,i} \hat{n}_{c,j} + V_S \sum_{\langle i,j \rangle} (t_{\alpha,i} t_{\alpha,j})_S^\dagger (t_{\alpha,i} t_{\alpha,j})_S \\ & + J_\pi \sum_{\langle i,j \rangle, \alpha} (b_i^\dagger b_j t_{\alpha,j}^\dagger t_{\alpha,i} + h.c.) + V_\pi \sum_{\langle i,j \rangle, \alpha} (b_i^\dagger b_i t_{\alpha,j}^\dagger t_{\alpha,j} + h.c.). \end{aligned} \quad (2.12)$$

The bosonic quasiparticles obey a local hardcore constraint:

$$b_i^\dagger b_i + \sum_\alpha t_{\alpha,i}^\dagger t_{\alpha,i} \leq 1. \quad (2.13)$$

Here again  $\langle i, j \rangle$  denotes pairs of neighbored sites  $(i, j)$  and  $\alpha = x, y, z$ .  $(t_{\alpha,i} t_{\alpha,j})_S^\dagger$  creates triplets with total Spin  $S$  on sites  $i, j$  and  $\hat{n}_{c,i}$  is the particle number operator for the charge bosons on site  $i$ . The calculations of Altman and Auerbach showed that  $J_s$  and  $J_{ss}$  are very close within a wide range of the Hubbard  $U$  keeping  $t$  constant. Thus, for the further calculations it is justified to consider only the case  $J_{ss} := J_s$ , then  $\hat{H}_t$  takes a more convenient form:

$$\hat{H}_t = \Delta_s \sum_i t_{\alpha,i}^\dagger t_{\alpha,i} + J_s \sum_{\langle i,j \rangle} \hat{n}_{\alpha,i} \hat{n}_{\alpha,j}, \quad (2.14)$$

where  $\hat{n}_{\alpha,i} = (t_{\alpha,i}^\dagger + t_{\alpha,i})$ . The parameters in the model vary as a function of the Hubbard  $U$ , like it is depicted in Fig. 2.4. For  $U/t \approx 8$ , the model is close to a projected  $SO(5)$  symmetry point. It is known from numerically essential exact evaluations of the 2D *Hubbard-model*, that it reproduces salient features of the high-temperature superconductors precisely in this regime [79, 66]. Thus, the projected  $SO(5)$  symmetric point is obtained in this physically relevant regime. This issue will be discussed in more detail in Sec. 3.4.1.

## 2.3 Conclusions

In summary, the application of the CORE algorithm has shown that the low-lying states of the 2D *Hubbard-model* provide basic ingredients for a description of the physics in the copper-oxide layers of the high- $T_c$  superconductors [23]: Antiferromagnetism can be understood as a ‘‘condensation’’ of triplet magnons, and superconductivity as a condensation

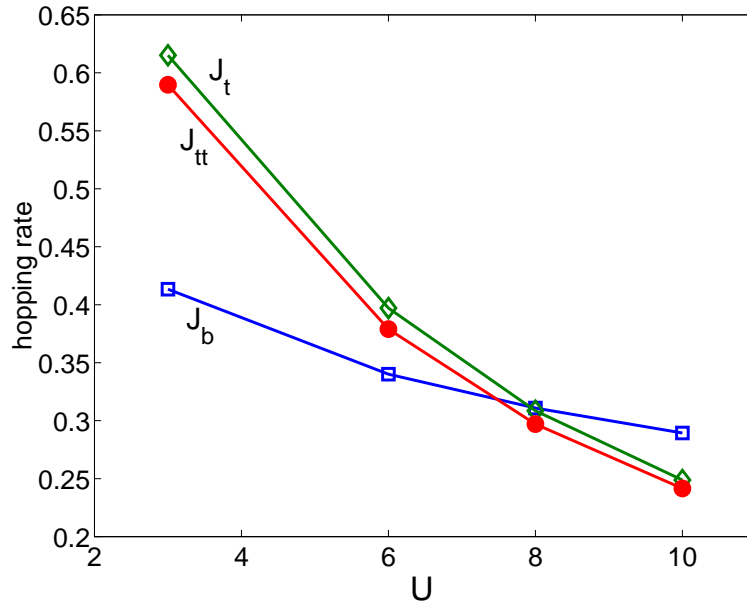


Figure 2.4: Boson hopping rates versus Hubbard  $U$ . The three lines intersect (nearly) at Hubbard  $U \approx 8t$ . This value of  $U$  is believed to be relevant for the high-temperature superconductors. The intersection region near  $U \approx 8t$  is close to the projected  $SO(5)$  point. Picture taken from [18]. The energies in the plot given are in units of  $t$ .

process of the hole pair bosons. These two excitations are the basic ingredients of the effective bosonic Hamiltonian. Further, the effective Hamiltonian fulfills a projected- $SO(5)$  symmetry in the parameter regime that is commonly believed to be relevant for the high- $T_c$  superconductors ( $U/t \approx 8$ ). An extensive numerical analysis of the obtained effective Hamiltonian is presented in Chap. 4 and Chap. 5.

# 3

## *SO*(5)-Theory

---

In the previous chapter the construction of a ‘coarse grained’ low-energy effective model using the Contractor-Renormalization Group technique has been discussed.. A complementary, approach to describe the physics of the high- $T_c$  superconductors is to employ symmetry principles. The latter can be motivated by experimental observations and impose constraints on the models. In the current chapter, the *SO*(5)-theory of high-temperature superconductivity will be discussed.

### 3.1 Introduction

Symmetry principles have been a very successful concept in physics. Symmetry unifies apparently different phenomena into a common framework. Well-known examples are the unification of the electric  $\vec{E}$  and the magnetic field  $\vec{B}$ , which is the result of the underlying relativistic space-time symmetry. Considering the high-temperature superconductors, the central question is how to unify the antiferromagnetic (AF) and superconducting (SC) phases, apparent in **all** high-temperature superconductors (see Fig. 3.1).

A new and detailed summary of the key ideas and results of the *SO*(5)-theory is presented in Ref. [18].

Zhang proposed 1997 [17] to combine the three-dimensional AF ( $\vec{N}_{Néel}$ ) and the two-dimensional SC order parameter ( $\vec{\Delta}_{SC}$ ) by introducing a five dimensional superspin  $\vec{n}$  (see Fig. 3.4). The superspin concept is only useful, if there is also some symmetry group acting on it. In order to avoid constraints, it is most natural to consider the most general rotation of the five dimensional order parameter. This most general rotation in a five dimensional parameter space is described by the *SO*(5) group. The *SO*(5)-symmetry is the lowest symmetry-group embedding the *SO*(3) AF spin rotational symmetry and the *U*(1) symmetry of charge conservation.

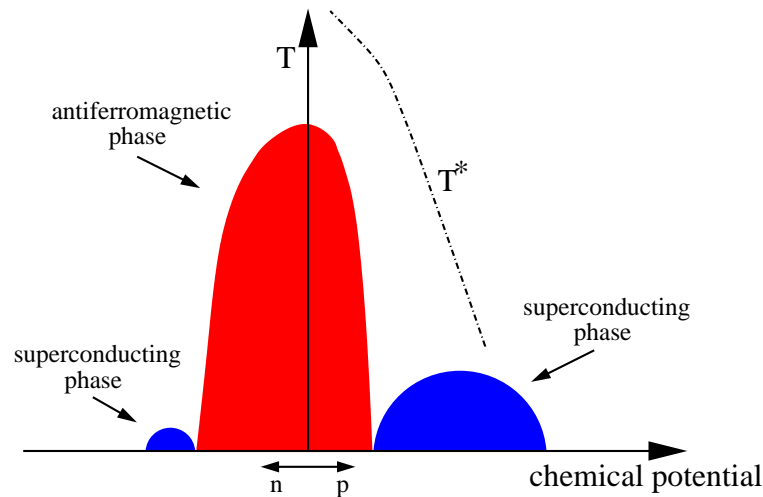


Figure 3.1: Generic temperature versus chemical potential phase diagram of the high-temperature superconductors. The chemical potential can be varied experimentally by different hole doping concentrations. ‘n’ and ‘p’ indicate electron and hole doping, respectively. The dashed-dotted ‘ $T^*$ ’ line indicates the pseudo gap temperature, below which the so called ‘pseudo-gap regime’ is located.

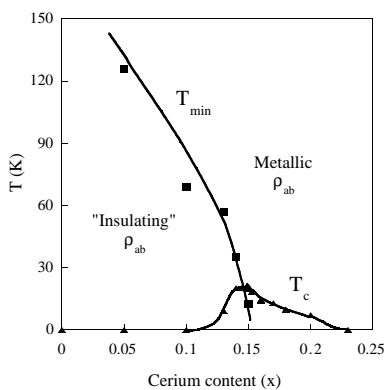


Figure 3.2: Phase diagram of the electron doped cuprate superconductor  $Pr_{2-x}Ce_xCuO_4$ .

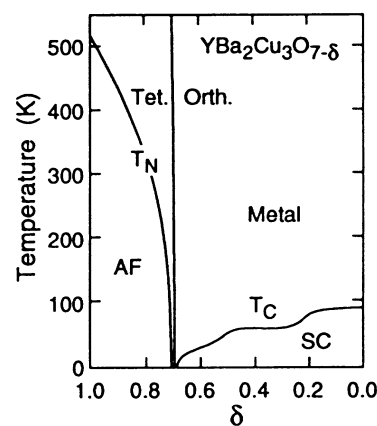


Figure 3.3: Phase diagram of the hole doped cuprate superconductor  $YBa_2Cu_3O_{7-\delta}$ .



$$\begin{array}{ccc}
 \vec{\Delta}_{SC} = \begin{pmatrix} \Delta_{Re} \\ \Delta_{Im} \end{pmatrix} & \longrightarrow & \vec{n} = \begin{pmatrix} \Delta_{Re} \\ N_x \\ N_y \\ N_z \\ \Delta_{Im} \end{pmatrix} \\
 \vec{N}_{Néel} = \begin{pmatrix} N_x \\ N_y \\ N_z \end{pmatrix} & \longrightarrow & 
 \end{array}$$

Figure 3.4: Combination of the AF (Néel) order parameter and the SC order parameter into a five dimensional superspin.

In a complete  $SO(5)$  symmetric system the superspin could rotate freely in a five dimensional sphere. One would thus expect also mixed states with coexistence of antiferromagnetism (AF) and superconductivity (SC). However, in the cuprates the  $SO(5)$ -symmetry is explicitly broken by the chemical potential, which plays an analogous role to the magnetic field in  $SO(3)$  symmetry of angular momentum. Similar to a magnetic field, which reduces the degeneracy of the angular momentum multiplet states (Zeeman effect), the chemical potential in the  $SO(5)$ -theory of high-temperature superconductivity induces an energetic anisotropy between AF and SC states, and thus lifts the degeneracy (for details see Ref. [?]).

## 3.2 Mathematical formulation

Following [17, 18, 80, 31], the ideas of the preceding section will be cast now into a mathematical formalism. Starting point of the  $SO(5)$ -theory is the  $SO(3)$  spin symmetry, which is broken in the AF state of the high-temperature superconductors and the  $U(1)$  symmetry of charge conservation, which is broken in the SC state. The AF order parameter  $\vec{N}_{Néel}$  is defined as:

$$\vec{N}_{Néel} = \sum_{\vec{k}, s, s'} c_{\vec{k}+(\pi, \pi), s}^\dagger \sigma_{s, s'}^\alpha c_{\vec{k}, s'}, \quad (3.1)$$

and the corresponding symmetry group is generated by the  $\alpha$  components of the spin operator:

$$\hat{S}_\alpha = \sum_{\vec{k}, s, s'} c_{\vec{k}, s}^\dagger \sigma_{s, s'}^\alpha c_{\vec{k}, s'}, \quad (3.2)$$

obeying the  $SO(3)$ -commutation relations:

$$[S_\alpha, S_\beta] = i\epsilon_{\alpha, \beta, \gamma} \cdot S_\gamma \quad \text{and} \quad [S_\alpha, N_\beta] = i\epsilon_{\alpha, \beta, \gamma} \cdot N_\gamma. \quad (3.3)$$

Here  $c_{\vec{k},s}^\dagger$  ( $c_{\vec{k},s}$ ) creates (annihilates) an electron with momentum  $\vec{k}$  and spin  $s$ ,  $\sigma^\alpha$  are Pauli matrices and  $\alpha, \beta, \gamma \in \{1, 2, 3\}$  denote a direction in the  $\mathbb{R}^3$  (x,y,z).

Let's recall also the corresponding quantities of the  $U(1)$  symmetry: The d-wave SC order parameter ( $\vec{\Delta}$ ), the  $U(1)$  symmetry generator ( $Q$ ) and their commutation relation:

$$\vec{\Delta} = \frac{1}{2} \sum_{\vec{k},s,s'} d(\vec{k}) c_{\vec{k},s}^\dagger \sigma^y c_{-\vec{k},s'} \Delta, \quad (3.4)$$

$$Q = \frac{N_{e^-} - N_o}{2}, \quad (3.5)$$

$$[Q, \Delta_i] = \epsilon_{i,j} \Delta_j. \quad (3.6)$$

$d(\vec{k})$  is the d-wave prefactor  $d(\vec{k}) = \cos(k_x) - \cos(k_y)$  and  $i, j \in \{1, 2\}$  label the real and the imaginary part of the order-parameter. The component wise combination of the upper order-parameters (defined in Eq. (3.1) and Eq. (3.4)) yields the new  $SO(5)$  superspin  $\vec{n}$  (depicted in Fig. 3.4).

A  $SO(n)$  group is composed out of  $n(n-1)/2$  different generators, thus the  $SO(5)$  group has 10 generators, specified in an antisymmetric matrix  $L_{ab} = -L_{ba}$ . The  $SO(5)$  group embeds the  $U(1)$  and the  $SO(3)$  group, so the spin and charge operators given in Eq. (3.2) and Eq. (3.5) are four generators of the  $SO(5)$  group. The missing six, so called  $\pi$  operators have been introduced by Demler and Zhang [81], and as discussed later, they connect AF and SC states. They have the form:

$$\pi_\alpha^\dagger = \sum_{\vec{k},s,s'} g(\vec{k}) c_{\vec{k}+(\pi,\pi),s}^\dagger (\sigma^\alpha \sigma^y)_{s,s'} c_{-\vec{k},s'}^\dagger \quad \text{and} \quad \pi_\alpha = (\pi_\alpha^\dagger)^\dagger. \quad (3.7)$$

$g(\vec{k})$  is the sign of the d-wave prefactor  $d(\vec{k})$ , i.e.  $g(\vec{k}) = \text{sign}(\cos(k_x) - \cos(k_y))$ . These six  $\pi_\alpha^{(\dagger)}$  operators together with the four operators  $\hat{S}_x, \hat{S}_y, \hat{S}_z$  and  $Q$  can be cast into the  $5 \times 5$  generator matrix:

$$L = \begin{pmatrix} 0 & -(\pi_x^\dagger + \pi_x) & -(\pi_y^\dagger + \pi_y) & -(\pi_z^\dagger + \pi_z) & -Q \\ \pi_x^\dagger + \pi_x & 0 & \hat{S}_z & -\hat{S}_y & i(\pi_x^\dagger - \pi_x) \\ \pi_y^\dagger + \pi_y & -\hat{S}_z & 0 & \hat{S}_x & i(\pi_y^\dagger - \pi_y) \\ \pi_z^\dagger + \pi_z & \hat{S}_y & -\hat{S}_x & 0 & i(\pi_z^\dagger - \pi_z) \\ Q & -i(\pi_x^\dagger - \pi_x) & -i(\pi_y^\dagger - \pi_y) & -i(\pi_z^\dagger - \pi_z) & 0 \end{pmatrix} \quad (3.8)$$

The generators  $L_{ab}$  form a Lie-Algebra: It is straightforward to show that they span a linear vector space. Further, there exists a commutator, obeying

$$[L_{ab}, L_{cd}] = -[L_{ba}, L_{dc}], \quad (3.9)$$

and the  $L_{ab}$  also fulfill the Jacobi-Identity:

$$[[L_{ab}, L_{cd}], L_{ef}] + [[L_{cd}, L_{ef}], L_{ab}] + [[L_{ef}, L_{ab}], L_{cd}] = 0. \quad (3.10)$$

Equation (3.9) follows immediately from the antisymmetric form of the  $SO(5)$  generator matrix and the Jacobi-Identity (Eq. (3.10)) from the basic  $SO(5)$  commutation relation:

$$[L_{ab}, L_{cd}] = -i(\delta_{ac}L_{bd} + \delta_{bd}L_{ac} - \delta_{ad}L_{bc} - \delta_{bc}L_{ad}). \quad (3.11)$$

The components of the five-dimensional superspin  $\vec{n}$  also obey commutation relations with the group's generators  $L_{ab}$ :

$$[L_{ab}, n_c] = -i\delta_{bc}n_a + i\delta_{ac}n_b. \quad (3.12)$$

Using the identities  $L_{2..4,1} = \pi_\alpha^\dagger + \pi_\alpha$  and  $n_{2..4} = N_\alpha$ , one obtains easily:

$$[\pi_\alpha^\dagger, N_\beta] = \frac{1}{2i}\delta_{\alpha,\beta} \Delta^\dagger \quad (3.13)$$

and

$$[\pi_\alpha, N_\beta] = \frac{1}{2i}\delta_{\alpha,\beta} \Delta. \quad (3.14)$$

Thus physically speaking, the  $\pi_\alpha^{(\dagger)}$  operators replace triplets by hole or electron pairs [18, 80, 81]. This corresponds to a rotation of the  $SO(5)$  order-parameter from the AF into the SC direction and vice versa. The  $L_{1\alpha}$  are the generators of the rotation, (see also Fig. 3.5):

$$e^{i\frac{\pi}{2}L_{1\alpha}} |AF\rangle = |SC\rangle \quad (3.15)$$

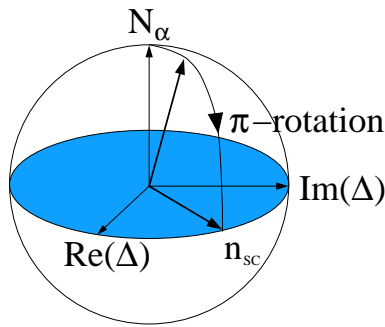


Figure 3.5: Sketch of the  $\pi$ -rotation: The  $\pi$ -operator rotates the an AFstate from the  $n_\alpha$  direction on the SC plane.

### 3.3 $SO(5)$ Symmetry in the Hubbard- and $t - J$ Model

In the previous section the mathematical formalism of the  $SO(5)$  group has been briefly reviewed. Whereas this theory was originally proposed as an effective field theory

description of the high-temperature superconductors, it turned out, that the  $SO(5)$ -symmetry, could be implemented also in microscopic models. Therefore, it was essential to test the models commonly accepted to be relevant for the description of the cuprate physics, i.e., the  $t - J$  and the *Hubbard-model*, about their relation with the  $SO(5)$ -symmetry group.

A microscopic model obeys a  $SO(5)$  symmetry, if the Hamiltonian commutes with the generators of the  $SO(5)$  group, i.e.

$$[\hat{H}, L_{ab}] = 0. \quad \forall a, b \in \{1, 2, \dots, 5\} \quad (3.16)$$

Obviously the  $\hat{S}_\alpha$  and the charge operators commute with the  $t - J$  and the *Hubbard-model*. But what about the  $\pi$  operators? These operators, defined in Eq. (3.7), do not commute with the Hubbard- or the  $t - J$  model. However, they satisfy a weaker condition:

$$[\hat{H}, \pi_\alpha^\dagger] \approx \omega_\alpha \pi_\alpha^\dagger. \quad (3.17)$$

The  $\pi$  operators are so called ‘approximate eigenoperators’, at least for small excitation energies  $\omega_\alpha$ . Applying an eigenoperator on an eigenstate of a Hamiltonian yields an other eigenstate. Subsequent application will generate a multiplet, that is not degenerate, but the energy levels are equally spaced by  $\omega_\alpha$ . This means that the dynamic auto-correlation function of the  $\pi_\alpha$  operators contains a sharp peak at energy  $\omega_\alpha$ . Although the  $SO(5)$  symmetry is explicitly broken in the Hubbard and  $t - J$  model, the  $SO(5)$  multiplet structure is still visible in the spectrum and can be sampled by ladder operators. Equation (3.17) has been tested using a T-matrix approximation [81], and an early numerical test of the  $SO(5)$ -symmetry can be found in [82], where the dynamic auto-correlation function has been calculated. In Ref. [80] the relation of the  $t - J$  model with the  $SO(5)$ -theory has been studied, and it been shown that low-lying states of the  $t - J$  model fit nicely into a  $SO(5)$ -multiplet structure.

In conclusion one may state, that the *Hubbard-model*, as well as the  $t - J$  model, show clear signatures of an approximate  $SO(5)$ -symmetry. This is also supported by exact diagonalization results on finite clusters [82, 80, 31]. A more detailed discussion of this issue can be found in [18].

### 3.4 The projected $SO(5)$ -theory

The  $SO(5)$ -theory turned out to be a very successful approach towards salient properties of the high-temperature superconductors [18]. One success of  $SO(5)$ -theory is based on the prediction of a collective excitation, the so called ‘ $\pi$ -resonance mode’, the

Goldstone mode for the spontaneous symmetry breaking. This  $\pi$ -resonance mode offers a natural explanation for the neutron resonance mode observed in wide range of cuprate superconductors [83, 84, 85, 86, 87, 88, 89, 90, 91, 92]. This resonance mode has been observed at energy  $\omega_0 = 41meV$  and wave vector  $\vec{k} = (\pi, \pi)$ , in the SC state and vanishes above  $T_c$ . Beyond the  $\pi$ -resonance mode the  $SO(5)$ -theory makes a number of further experimental predictions, such as the existence of AF and then, necessarily, SC states [93, 94, 95, 96]. However, despite its success the  $SO(5)$ -theory in its original formulation [17] cannot describe the Mott physics, experimentally observed in the cuprate superconductors at half-filling [82, 97, 98, 99]. The origin of this problem is inherent in the  $SO(5)$ -symmetry itself: In a fully  $SO(5)$  symmetric system a hole pair and an electron pair, require to have the same (zero) excitation energy as a collective spin-wave excitation. In other words, the  $SO(5)$  multiplets are energetically degenerated. In the real cuprates however, at half filling the formation of an electron pair on one lattice site is connected with an energy penalty of order  $U$ , originating from the Coulomb repulsion of the electrons (see Fig. 3.6).

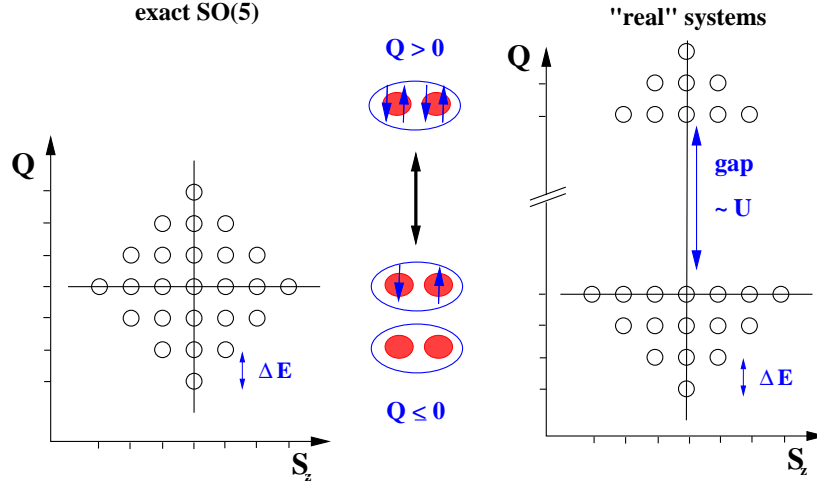


Figure 3.6: Exemplary multiplet for a fully  $SO(5)$  symmetric (ladder) model (left). A transition from a state represented by  $\circ$  to another state can be performed without a change in energy. However, if the exact  $SO(5)$ -symmetry is explicitly broken, for example by a chemical potential, then the states with neighbored charge quantum numbers  $Q$  are separated by a constant energy gap  $\Delta E$ . In realistic physical systems, electron-electron excitations above half filling are unfavorable due to the Coulomb repulsion, which causes a large energy gap of the order of the Hubbard  $U$ .

One escape from this situation is to start from an  $SO(5)$ -symmetric Hamiltonian and to break explicitly the  $SO(5)$ -symmetry, by projecting out the double occupancies, i.e. the electron pairs. This so called ‘Gutzwiller projection’ can be justified by straight-forward physical means: The Mott-Hubbard gap in the copper-oxide superconductors is of the order of several  $eV$ , this corresponds to temperatures higher than 10000K. This energy scale is far beyond the energy scale of the physics under consideration, namely antiferromagnetism and superconductivity, taking place at substantially lower temperatures  $T_N$  and  $T_c$ . Therefore, states containing on-site pairing of electrons should not be important for an understanding of the cuprate physics. Due to the extremely high energy penalty, they do not even need to be taken into account as intermediate states in scattering processes.

The resulting models that implement the Gutzwiller constraint are called ‘projected  $SO(5)$ ’ models or simply ‘ $pSO(5)$ ’ models. When constructing such a projected- $SO(5)$  model, one has to make sure to shift the chemical potential to the edge of the lower band. This restores the energetic degeneracy of hole-pair and spin-excited states in hole doped systems (see Fig. 3.7).

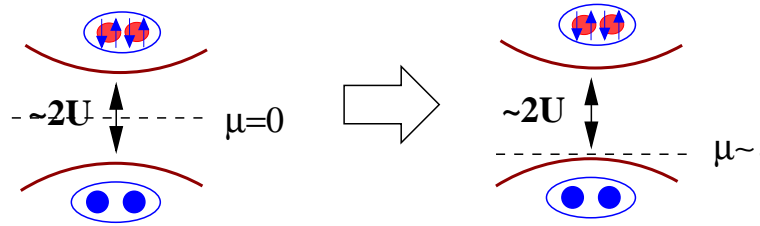


Figure 3.7: By shifting the chemical potential to the lower band, the projected- $SO(5)$  models can account for the degeneracy of hole-pair and spin excited states. The electron pairs become irrelevant for the microscopic description due to the large Mott-Hubbard gap. Figure by A. Dorneich.

### 3.4.1 The projected $SO(5)$ Model

In Ref. [100] Zhang, Hu, Arrigoni, Hanke and Auerbach constructed a model, where the Gutzwiller constraint of no double occupancy is implemented exactly. Their model reads:

$$\hat{H} = \Delta_s \sum_{x, \alpha=2,3,4} t_\alpha^\dagger(x) t_\alpha(x) + (\Delta_c - 2\mu) \sum_x t_h^\dagger(x) t_h(x) \quad (3.18)$$

$$- J_s \sum_{\substack{\langle x x' \rangle \\ \alpha=2,3,4}} n_\alpha(x) n_\alpha(x') - J_c \sum_{\langle x x' \rangle} \left( t_h^\dagger(x) t_h(x') + h.c. \right).$$

The operators  $t_\alpha^{(\dagger)}$  annihilate (create) an  $\alpha$  triplet ( $\alpha \in \{x, y, z\}$ ),  $t_h^{(\dagger)}$  annihilates (creates) a hole pair excitation and  $n_\alpha = \frac{1}{\sqrt{2}} (t_\alpha^\dagger + t_\alpha)$ . The  $x$  and  $x'$  label the lattice sites. This model is defined on a coarse grained lattice, where each site corresponds to a four-site electronic system. The vacuum state corresponds to the ground state of the underlying electronic system. The operators obey a local hard-core constraint:

$$t_h^\dagger(x)t_h(x) + \sum_{\alpha=2,3,4} t_\alpha^\dagger(x)t_\alpha(x) \leq 1. \quad (3.19)$$

The Gutzwiller projection in the limit  $U \rightarrow \infty$  simply reduces the Hilbert space such that  $t_p^\dagger(x)|vac\rangle = 0$ , where  $t_p^\dagger(x)$  would create a local electron-electron pair in the full Hilbert space. The Hamiltonian (Eq. (3.18)) is equivalent to the effective bosonic low energy model discussed in Sec. 2.2, if one neglects the quartic terms of Eq. (2.9) and considers the strong coupling case of  $U \approx 8t$ .

### 3.4.2 Properties of the projected $SO(5)$ Model

The projected- $SO(5)$  model on a two-dimensional lattice has been studied for the first time numerically by Dorneich and coworkers. Their results reproduce many salient features of the high-temperature superconductors [20, 56] and revealed, that the projected- $SO(5)$  model incorporates many ingredients, essential for a correct description of the high-temperature superconductors. However, a number of open questions could not be addressed by simulations of a two dimensional system. For example, it is impossible to observe AF order at finite temperatures (see Sec. 5.2), making it impossible to compare the generic phase diagram (see Fig. 3.1) with the simulations. Another open question is revealed by mean-field results [100]: The energy difference between a hole and a local spin excitation (see Sec. 3.4.1) can be compensated by adjusting the chemical potential  $\mu$ . In this case the mean-field ground state recovers **exact**  $SO(5)$  symmetry at  $J_c = 2J_s$  and  $\Delta_s = \Delta_c$  [100]. But on the other hand, the Casimir operator of the  $SO(5)$  group does not commute with the projected  $SO(5)$  Hamiltonian. These results bring up the question about the relevance of  $SO(5)$  symmetry in the projected- $SO(5)$  model. Is there a point in the phase diagram where the  $SO(5)$  symmetry is restored also ‘dynamically’? In a classical  $SO(5)$  symmetric system symmetry restoration can indeed be observed, if the symmetry breaking terms have an appropriate sign [101]. But this is in contrast to the results from the  $\epsilon$ -expansion [102], that predict a fluctuation induced first-order transition. In the following chapter these questions will be addressed by means of an accurate Quantum-Monte-Carlo analysis.

# 4

## Numerical Analysis of the projected $SO(5)$ Model

---

In this chapter the different ideas and results discussed in chapter 2 and chapter 3 are merged with the technique presented in chapter 1, i.e., the *Stochastic-Series Expansion* is applied to the effective bosonic Hamiltonian motivated by the  $SO(5)$ -theory and by the Contractor-Renormalization Group analysis of the one-band *Hubbard-model*. This combination allows to test salient ideas underlying the projected- $SO(5)$  model, and in addition, the results should reflect the low-energy properties of the *Hubbard-model*, like discussed in chapter 2.

### 4.1 Phase Diagram

Starting point of the analysis is the phase diagram of the 3D-projected  $SO(5)$  model (see Eq. 3.18) for the “symmetric” case  $J_s = J_c/2 = J$  in Fig. 4.1. This choice of parameters is called “symmetric”, because the model has a static  $SO(5)$ -symmetry on a mean field level [100], this static  $SO(5)$ -symmetry is broken only by quantum fluctuations [103].

Fig. 4.1 shows an AF and a SC phase extending to finite temperatures. Furthermore, the two phase transition lines merge into a multicritical point (at  $T_b = 0.960 \pm 0.005$  and  $\mu_b = -0.098 \pm 0.001$ ). The line of equal correlation decay of hole-pairs and triplet bosons also merges into this multicritical point  $P$ . Unlike the corresponding phase in the classical  $SO(5)$ -model, which has been studied by Hu [104], the SC phase extends only over a finite  $\mu$  range; this is due to the hardcore constraint of the hole-pair bosons and agrees with experimentally determined phase diagrams of the cuprates. In this sense, the quantum mechanical projected- $SO(5)$  model is more physical than the classical  $SO(5)$  model.



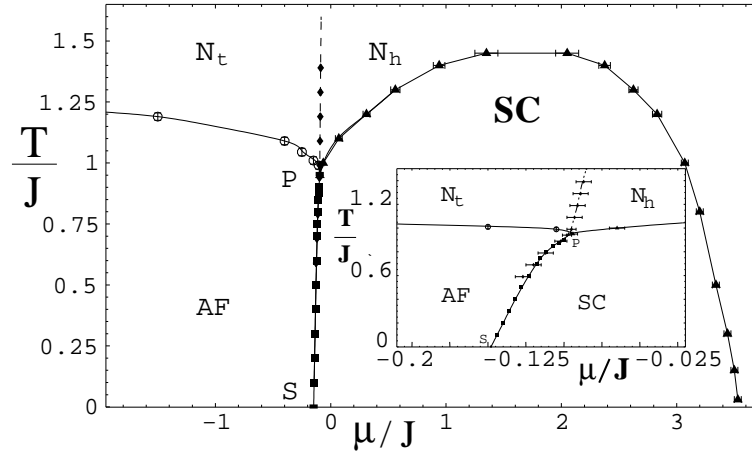


Figure 4.1: Phase diagram  $T(\mu)$  of the three-dimensional  $pSO(5)$  model with  $J = J_s = J_c/2$  and  $\Delta_s = \Delta_c = J$ .  $N_h$  and  $N_t$  are, respectively, the hole-pair and the magnon-dominated regions of the disordered phase. The separation line between  $N_h$  and  $N_t$  is the line of equal spatial correlation decay of hole-pairs and bosons. The inset shows a detailed view of the region near the multicritical point.

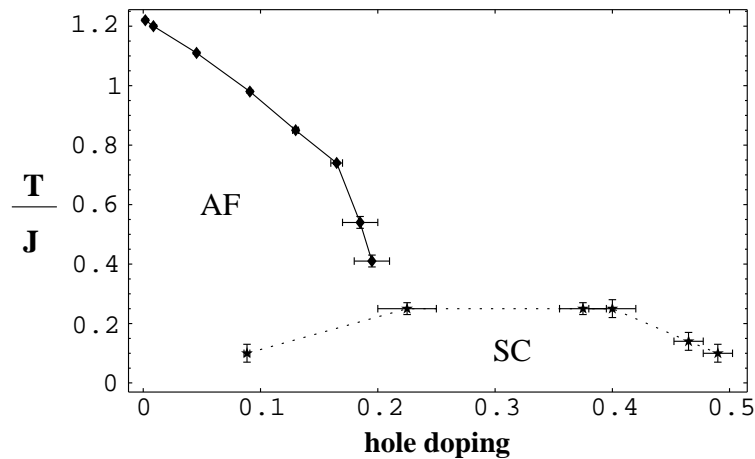


Figure 4.2: Phase diagram for  $J_c/(2J_s) = 0.225$  as a function of the hole doping  $\delta$ . The ratio  $T_n/T_c$  has the same order of magnitude like in the real cuprates.

However, in real copper-oxide superconductors the ratio between the maximum SC temperature  $T_c$  and Néel temperature  $T_N$  is about 0.17 to 0.25, whereas in the p $SO(5)$  model the values are:  $T_c/J = 1.465 \pm 0.008$  at  $\mu_{opt}/J \approx 1.7$  and  $T_N/J = 1.29 \pm 0.01$ , hence  $T_c$  is slightly larger than  $T_N$ . In order to obtain more realistic values for the transition temperatures, it is necessary to relax the *static*  $SO(5)$  condition and take a smaller value for the ratio  $J_c/(2J_s)$ , which breaks  $SO(5)$  symmetry even on a mean field level. The phase diagram with  $J_c/(2J_s) = 0.225$  is plotted in Fig. 4.2. As one can see, this gives a more realistic ratio of  $T_N/T_c \approx 0.2$ . However, it is pointed out that the numerical effort to treat such different values of  $J$  is order of magnitudes larger than considering  $J_c$  and  $J_s$  of the same order of magnitude, as presented in Fig. 4.1. Thus, for  $J_c/(2J_s) = 0.225$  the precision of the phase diagram is not sufficient to extract the scaling behavior. Therefore, in Sec. 4.2.2 a system with  $J_c = J_s = 1$  will be considered, for which also the static  $SO(5)$  symmetry is broken. For the same reason, the  $c$ -axis anisotropy is neglected here in favor of an isotropic 3D model.

Before the scaling behavior for the different sets of parameters is considered, first an analysis of the critical properties for the static  $SO(5)$ -symmetric case ( $J_c/(2J_s) = 1$ ) is presented. A closer look to the phase transition line between the points  $S$  and  $P$  reveals (inset of Fig. 4.1) that this line is not vertical as in the classical  $SO(5)$  model but slightly inclined. This indicates that a finite latent heat is connected with the AF-SC phase transition. Moreover, this means that in contrast to the classical model,  $\mu$  is not a scaling variable for the bicritical point  $P$ .

## 4.2 Scaling Analysis

### 4.2.1 Case $J_s = J_c/2$ , static $SO(5)$ -symmetry

Now, the problem of symmetry restoration is addressed, or in other words: Is the  $SO(5)$ -symmetry restored dynamically close to the multicritical point in the phase diagram? Hu performed a scaling analysis similar to the one presented here in a classical  $SO(5)$  model in which an additional quartic anisotropy term has been included [104]. Classical Monte Carlo calculations are by orders of magnitude easier to perform and less resource demanding than QMC simulations, hence very large system sizes can be simulated and highly accurate data are obtained. For this reason Hu could carry out a detailed analysis of the AF-SC phase diagram and of the critical behavior. In contrast to his work, here a quantum system is studied. In order to determine the phase diagram (for  $J_c/(2J_s) = 1$ ) the antiferromagnetic- (AF) and superconducting- (SC) order parameters are calculated for systems of up to  $18^3 = 5096$  lattice sites, what allows to perform an accurate finite size scaling: On the SC side, the finite-size scaling to extract the order parameter and the

SC transition temperature turns out to be quite reliable. On the other hand, on the AF side, the fluctuations in the particle numbers of the three triplet bosons slightly increase the statistical errors of the SSE results and make the finite-size scaling more difficult.

First, the form of the  $T_N(\mu)$  and  $T_c(\mu)$  curves in the vicinity of the bicritical point is determined. For crossover behavior with an exponent  $\phi > 1$  one would generally expect that the two curves merge tangentially into the first-order line. However, this holds for the scaling variables, therefore, one should first perform a transformation from the old  $\mu$  axis to a new  $\mu'$  axis defined by  $\mu'(T) = \mu - (T - T_b)/m$ , where  $m \approx 0.11$  is the slope of the first order line below  $T_b$ .

After this transformation, the transition curves  $T_N(\mu')$  and  $T_c(\mu')$  are quite well described by the crossover behavior (the prime is dropped for convenience)

$$\begin{aligned} \frac{T_c(\mu)}{T_b} - 1 &= B_2 \cdot (\mu - \mu_b)^{1/\phi} \\ \text{and} \quad \frac{T_N(\mu)}{T_b} - 1 &= B_3 \cdot (\mu_b - \mu)^{1/\phi} \end{aligned} \quad (4.1)$$

The fit to this behavior is shown in more detail in Fig. 4.3. However, the value of  $\phi$  obtained here

$$\phi \approx 2.35, \quad (4.2)$$

is considerably larger than the value expected from the  $\epsilon$ -expansion. It should be noted that the above determination of  $\phi$  is not very accurate: the data points in Fig. 4.3 are the result of a delicate finite-size scaling, even if the precision of this scaling would be sufficient, the error introduced by the subsequent transformation from  $\mu$  to  $\mu'$  again increases the numerical error bars significantly. For this reason it cannot be excluded, that the accumulation of statistical errors, finite size effects and the errors introduced by the transformation are responsible for the difference in the  $\phi$  values. Therefore, a more accurate evaluation of  $\phi$  is employed below.

The critical exponents for the onset of AF and SC order as a function of temperature for various chemical potentials can be extracted from Fig. 4.3.

Far into the SC range, at  $\mu = 1.5$ , the SC helicity modulus [105] can be described using:

$$\Upsilon \propto (1 - T/T_c)^\nu \quad \text{with} \quad \nu = 0.66 \pm 0.02, \quad (4.3)$$

which matches very well the values obtained by the  $\epsilon$ -expansion and by numerical analyses of a 3D-XY model. On the AF side, error bars are larger, as discussed above. The AF-order parameter scales like:

$$C_{AF}(\infty) \propto (1 - T/T_c)^{\beta_3} \quad \text{with} \quad \beta_3 = 0.35 \pm 0.03, \quad (4.4)$$

for  $\mu = -2.25$ , also in accordance with the value expected for a 3D classical Heisenberg model.

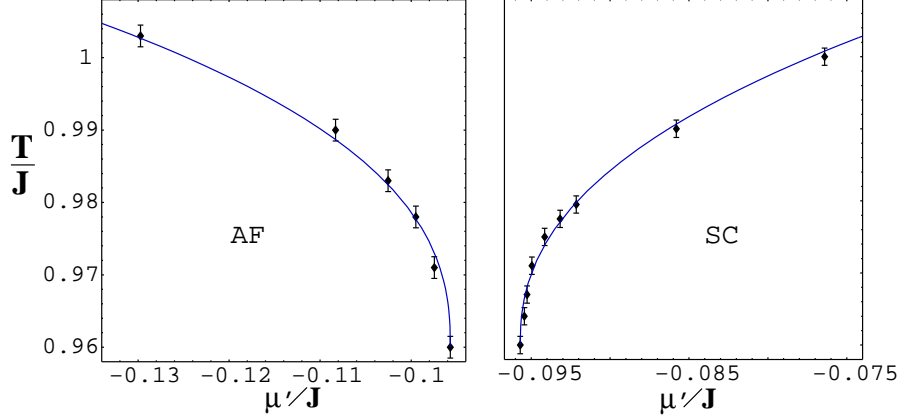


Figure 4.3: Plot of the AF (left) and SC (right) critical lines in the vicinity of the multicritical point.

In order to determine  $\nu$  and  $\phi$  more accurately in the crossover regime, two expressions derived from the scaling behavior are used (cf. Ref. [104]).

$$\Upsilon(T_b, \mu)/\Upsilon(T_b, \mu'') = ((\mu - \mu_b)/(\mu'' - \mu_b))^{\nu_5/\phi}. \quad (4.5)$$

and

$$\phi = \frac{\ln\left(\frac{\mu_2 - \mu_b}{\mu_1 - \mu_b}\right)}{\ln\left(\frac{\partial \Upsilon(T, \mu_1)/\Upsilon(T, \mu'_1)}{\partial T} \Big|_{T=T_b} / \frac{\partial \Upsilon(T, \mu_2)/\Upsilon(T, \mu'_2)}{\partial T} \Big|_{T=T_b}\right)} \quad (4.6)$$

where  $\mu_1, \mu'_1, \mu_2,$  and  $\mu'_2$  are related by  $(\mu_1 - \mu_b)/(\mu'_1 - \mu_b) = (\mu_2 - \mu_b)/(\mu'_2 - \mu_b) > 0$ . The result is shown in Fig. 4.4, the ratio is:

$$\nu_5/\phi = 0.52 \pm 0.01, \quad (4.7)$$

which is in excellent agreement with the results of the  $\epsilon$ -expansion and other numerical analyses [104].  $\phi$  is then obtained by using Eq. (4.6). Eq. (4.6) has been applied onto 9 different combinations of  $(\mu_1, \mu'_1 = \mu_2, \mu'_2)$  values with  $\mu_1/\mu'_1 = \mu_2/\mu'_2 = 0.5$ . The result is

$$\phi = 1.43 \pm 0.05, \quad (4.8)$$

which is again in good agreement with the  $\epsilon$ -expansion for a  $SO(5)$  bicritical point and with the results of Ref. [104].

#### 4.2.2 Case $J_s = J_c$

This agreement between the critical exponents obtained in the previous section may not come completely as a surprise, since the  $SO(5)$  symmetry is only broken by quantum

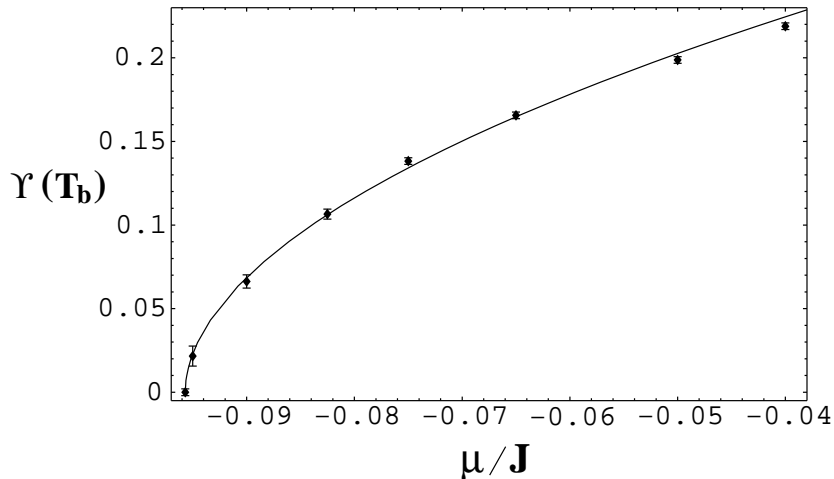


Figure 4.4: Helicity  $\Upsilon$  as a function of the chemical potential  $\mu$  at  $T = T_b$ . From this function, the value of  $\nu_5/\phi$  can be extracted via Eq. (4.5).

fluctuations for the parameters chosen here. The question addressed now, is whether  $SO(5)$  symmetry is also asymptotically restored for a more realistic set of parameters for which the static  $SO(5)$  symmetry is broken as well. As already mentioned above, the case, where the phase diagram of the cuprates is qualitatively well reproduced ( $J_c/(2J_s) = 0.225$ , see Fig. 4.2), is too difficult to address numerically, so that the critical exponents cannot be determined with sufficient precision in this case. Therefore, the analysis is repeated for the model in an intermediate regime ( $J_c = J_h$ ), which is not so realistic but for which the static  $SO(5)$  symmetry is broken as well. One could hope that if  $SO(5)$  symmetry is restored also here, then it might be also restored for the case  $J_c/(2J_s) = 0.225$ , although one may expect that the asymptotic region in which this occurs will be less extended. Also one has to consider that eventually one should expect the system to flow away from the  $SO(5)$  fixed point, although in a very small critical region, as pointed out by Aharony [106].

The phase diagram for  $J_c = J_h$  is presented in Fig. 4.5 and a detailed view of the region close to the bicritical point is plotted in Fig. 4.6. Here, the points in the plots were obtained by a finite-size scaling with lattices up to 5032 ( $18^3$ ) sites. In some cases, it has been possible to simulate lattices up to 10648 ( $22^3$ ) sites. An example of the finite-size scaling is shown in Fig. 4.7. Our analysis yields  $T_b = 0.682 \pm 0.005$  and  $\mu_b = 0.548 \pm 0.0005$ . Here the line of equal correlation decay is vertical within the error bars, so the transformation from  $\mu$  to  $\mu'$  is not necessary and the error bars are not increased by the transformation.

This allows to determine the critical exponents by fitting the data points visible in Fig. 4.6 against  $T(\mu) = T_b * \left(1 + (B_2 + B_3 * \text{Sign}[\mu_b - \mu]) * |x - \mu_b|^{\frac{1}{\phi}}\right)$ . The result reads:

$$B_2 = 0.47 \pm 0.07, \quad (4.9)$$

$$B_3 = 0.11 \pm 0.04, \quad (4.10)$$

$$\phi = 1.49 \pm 0.18, \quad (4.11)$$

$$Tb = 0.683 \pm 0.004, \quad (4.12)$$

$$\frac{B_2}{B_3} = 1.67, \pm 0.36 \quad (4.13)$$

Since points further away from the bicritical point are expected to show a larger deviation from the bicritical behavior, also a weighted fit has been performed, which takes this fact into account. Here, data points closer to the bicritical point are weighted more than the ones further away. Specifically, in both the SC and the AF phase, the point closest to the bicritical point is weighted six times the one with the largest distance to the bicritical point. The second closest is weighted 5 times and so on. The results are, within the error bars, quite similar to the ones obtained without this different weighting procedure:

$$B_2 = 0.46 \pm 0.05, \quad (4.14)$$

$$B_3 = 0.11 \pm 0.03, \quad (4.15)$$

$$\phi = 1.53 \pm 0.12 \quad (4.16)$$

$$Tb = 0.682 \pm 0.003 \quad (4.17)$$

$$\frac{B_2}{B_3} = 1.61 \pm 0.23 \quad (4.18)$$

The agreement between the equations (4.9) - (4.13) and equations (4.15) - (4.18) suggests that the data points, that have been considered are still controlled by the bicritical point, In order to test whether alternatively proposed fixed points may be excluded, a least-square fit of our data to the decoupled fixpoint behavior is carried out ( $\phi = 1, B_2, B_3$  and  $T_b$  arbitrary). The results are shown in Fig. 4.6 (dashed-dotted line). As one can see from the curve, the data does not support this hypothesis in the numerically accessible region.

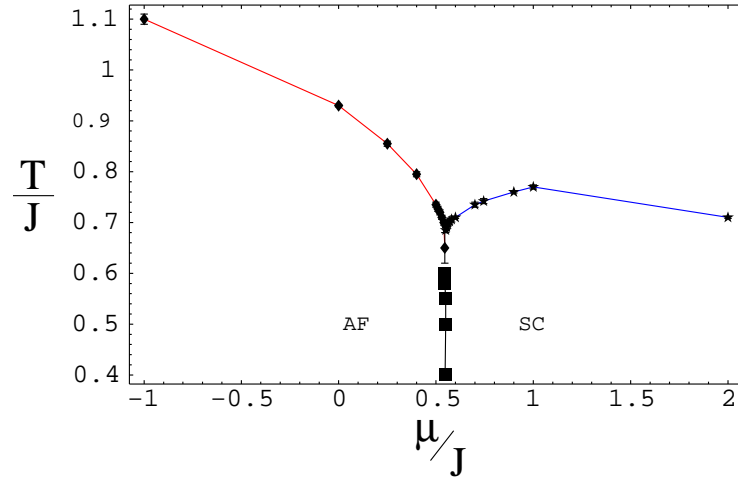


Figure 4.5: Phase diagram of the 3D-projected-SO(5) model as a function of the chemical potential for  $J_c = J_h = 1$ , the lines are guides to the eyes.

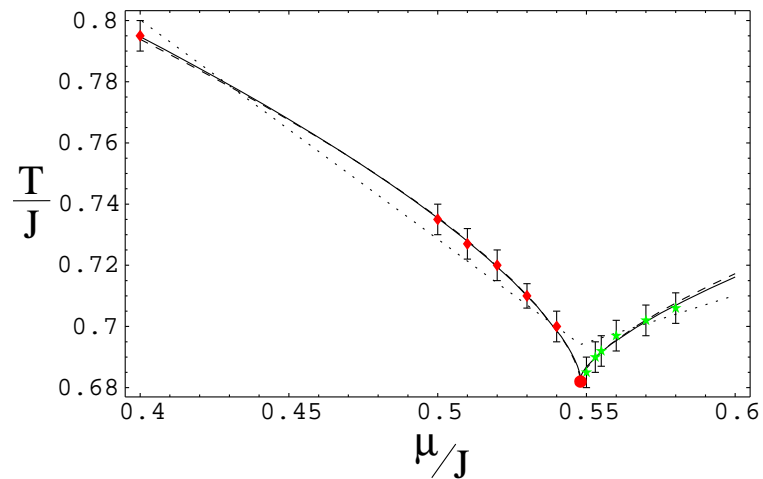


Figure 4.6: Detailed view of the phase diagram depicted in Fig. 4.5, as a function  $\mu$  ( $J_c = J_h = 1$ ). The two lines have been obtained by fits to  $T(\mu) = T_b * \left(1 + (B_2 + B_3 * \text{Sign}[\mu_b - \mu]) * |\mu - \mu_b|^{\frac{1}{\phi}}\right)$ . The continuous (dashed) line is the ‘normal’ (‘weighted’) fit. The decoupled fit point case is plotted as a dashed-dotted line.

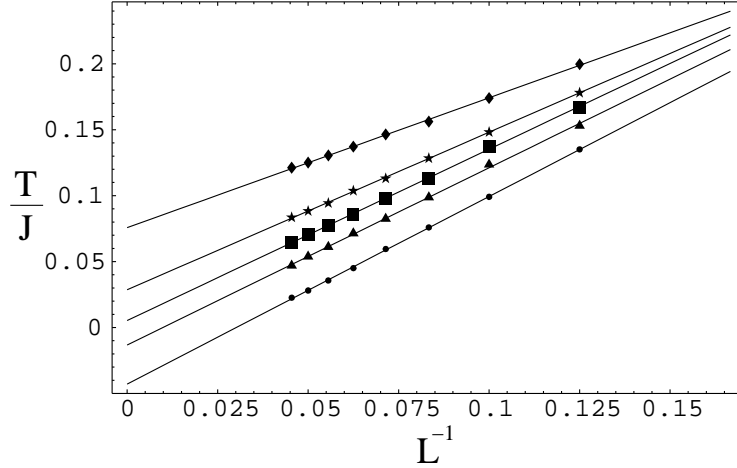


Figure 4.7: Finite size scaling of the AF order parameter for  $\mu = 0.5$ , the temperatures cover  $0.72J$  (lozenge),  $0.73J$  (star),  $0.735$  (square),  $0.74J$  (triangle) and  $0.75$  (circle). The lattice size was varied from  $216$  ( $8^3$ ) upto  $10648$  ( $22^3$ ) sites, scanning all cubes with even edge length.

### 4.3 Validity of the Crossover Exponents obtained by the numerical Analysis

Altogether, the scaling analysis of the 3D-projected  $SO(5)$  model has produced a crossover exponent which matches quite well with the corresponding value obtained from a classical  $SO(5)$  model and from the  $\epsilon$ -expansion. This gives convincing evidence that the static correlation functions at the p $SO(5)$  multicritical point is controlled by a fully  $SO(5)$  symmetric point in a large parameter region which is relevant experimentally and in the numerically accessible region. However, one should point out that within the statistical and finite-size error, as well as within the error due to the extrapolation of the  $\epsilon$ -expansion value to  $\epsilon = 1$ , one cannot exclude that the actual fixed point that is approached is the biconical one, which has very similar exponents to the isotropic  $SO(5)$  one. On the other hand, the biconical fixed point should be accompanied by a AF+SC coexistence region (as a function of chemical potential), which is not observed. As discussed above, one can certainly exclude in this transient region the *decoupled* fixed point for which  $\phi = 1$ . Of course, our limited system sizes cannot tell which fixed point would be ultimately stable in the deep asymptotic region. Here, Aharony's exact statement shows that the decoupled fixed point should be ultimately the stable one in the deep asymptotic region [106].



The discrepancy between the numerically observed dynamical restoration of  $SO(5)$ -symmetry and Aharony's arguments can be solved: To do so, the scale at which the instability of the  $SO(5)$  fixed point could be detectable is estimated, based on  $\epsilon$  expansion. This estimate holds for the case in which one has a "static"  $SO(5)$  symmetry at the mean-field level ( $J_s = J_2/2$ ). The symmetry-breaking effects due to quantum fluctuations have been estimated in Ref. [103] and are given by Eq. (36) there. By replacing the initial conditions for the bare couplings in terms of the microscopic parameters of the Hamiltonian (cf. equation. 26 of Ref. [103]), and projecting along the different scaling variables around the  $SO(5)$  fixed point, one obtains a quite small projection along the variable that scales away from the fixed point. Combined with the fact that the exponent for these scaling variables are quite small ( $\lambda = 1/13$  at the lowest-order in the  $\epsilon$  expansion, although more accurate estimates [107, 108, 109] give a somewhat larger value of  $\lambda \approx 0.3$ ), an estimate for the scaling region in which the  $SO(5)$  fixed point is replaced by another is obtained – e.g. the biconical or the decoupled – fixed point at  $t \equiv (T_b - T)/T_b \sim 10^{-10}$  if one takes the  $O(\epsilon)$  result for the exponent. Notice that taking the result of Ref. [108] for the exponent, one obtains a quite larger value  $t \approx 2 \cdot 10^{-3}$ . However, since the multi-critical temperatures of relevant materials (organic conductors, and, more recently,  $YBa_2Cu_3O_{6.35}$ ) are around  $10 K$ , the critical region is still basically inaccessible experimentally as well as with our *quantum* simulation. The situation is depicted schematically in Fig. 4.8.

On the other hand, the other scaling variables, although being initially of the order of 1, rapidly scale to zero due to the large, negative, exponents. Therefore, the  $SO(5)$  regime starts to become important as soon as the AF and SC correlation lengths become large and continues to affect the scaling behavior of the system basically in the whole accessible region.

## 4.4 Conclusions

Employing the essentially exact numerical Stochastic Series Expansion it has been shown, that the  $pSO(5)$  model, which combines the idea of  $SO(5)$  symmetry with a *realistic* treatment of the Mott-Hubbard gap, reproduces salient features of the cuprates' phase diagram. The model shows long-range ordered AF and SC phases, and the generic phase diagram (see Fig. 3.1) is reproduced qualitatively, if not even on a semiquantitative level. Furthermore, the scaling properties of the projected- $SO(5)$  model have been studied and it turned out that this model is controlled by a  $SO(5)$ -symmetric bicritical point, at least within a large transient region. A remarkable fact is, that this holds for a case in which the  $SO(5)$  symmetry is explicitly broken at the Hamiltonian level. Possible flow away

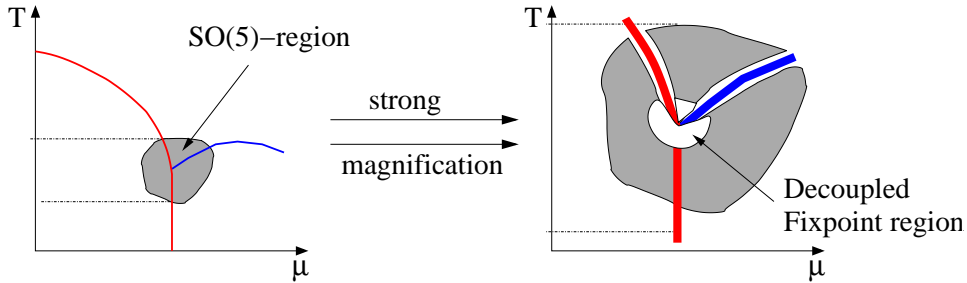


Figure 4.8: Schematic representation of the area where  $SO(5)$ -symmetry restoration takes place and where decoupled fixpoint behavior is predicted. The left plot is a schematic representation of our numerical results. The data obtained by the QMC simulations display an area close to the bicritical point, where  $SO(5)$ -symmetry is dynamically restored. This region is represented by the shaded area. The right plot shows a fixpoint zoom of the left plot with the bicritical point in its center. In this extremely magnified view the resolution is sufficient to observe also a region governed by the decoupled fixpoint behaviour, like stated by Aharony. However, a resolution like the one obtained by the fixpoint zoom here, cannot be achieved at present, not in the experiments nor with numerical simulations.

from the  $SO(5)$ -symmetric fix point occurs only within an extremely narrow region in reduced temperature, making it more or less impossible to observe this experimentally nor numerically. This last facet of our results is of course unsatisfactory as it cannot be falsified with the available techniques. However, this is very similar to many other examples in condensed-matter physics. The ubiquitous Fermi-liquid fix point is strictly speaking always unstable because of the Kohn-Luttinger effect [110]. But for most metals this instability occurs only at extremely low temperatures, and is practically irrelevant. Another example is the transition of an “ordinary” superconductor to normal-state at  $T_c$ . Strictly speaking, coupling to the fluctuating electromagnetic field renders this fix point unstable [111]. However, this effect has never been observed experimentally, since the associated critical region is too small. Therefore, irrespective of the question of ultimate stability, one can conclude that the  $SO(5)$  fix point is a robust one in a similar sense, and it controls the physics near the AF and SC transitions.

# 5

## Extension of the projected- $SO(5)$ Model

---

In the previous chapter a detailed study of the phase diagram of the projected- $SO(5)$  model in three dimensions has been presented. The results were encouraging: The projected- $SO(5)$  model reproduces salient features of the high-temperature superconductors' phase diagram. In addition, the idea of  $SO(5)$ -symmetry gets reinforced by the finding of symmetry restoration close to the bicritical point, although the  $SO(5)$ -symmetry is manifestly broken on the Hamiltonian level. However, the generic phase diagram depicted in Fig. 3.1 is simplified. Especially in the pseudo-gap regime, many different possible phases have been reported, such as a spin-glass phase or magnetic stripes [112, 113, 114]. This regime is characterized by a partial gapping of the low-energy density of states (DOS), which is detected below a characteristic temperature  $T^*$ . A possible interpretation of the pseudo-gap state is to consider it as a departure from the Fermi-liquid picture [115]. Two main routes have been followed to understand the pseudogap-physics of high- $T_c$  superconductors. One attempt is the so called 'preformed-pair scenario', where it has been proposed that superconducting pairing fluctuations persist above  $T_c$  up to  $T^*$  in the underdoped regime [116]. This idea has been supported by numerous experimental results, i.e.: The pseudogap evolves smoothly into the SC gap [117], the Nernst effect [118, 119] and an anomalous high-frequency conductivity [120]. According to the second attempt, the pseudogap regime can be characterized by a strong propensity for ordering. Several types of order have been proposed, including antiferromagnetism [121] and stripe order [115, 122] as well as charge density waves [123], to name only the most prominent. Recently scanning tunneling microscopy (STM) has been used to examine the electronic states of the cuprate superconductors at an atomic scale in the pseudogap state [27, 26]. These experiments show spatial modulations of the DOS, which are oriented along the Cu-O bond directions. Whereas in Ref. [27] these modulations have an incommensurate periodicity of  $\approx 4.7a_0$  (here  $a_0$  denotes the Cu-

Cu distance), in Ref. [26] commensurate periodicities of  $4a_0$ ,  $4/3a_0$  and  $a_0$  are reported (see Fig. 5.1). Chen, Zhang and coworkers, proposed, that these experiments may be interpreted in terms of a checkerboard pair-density wave [124, 125]. In the frame of the projected- $SO(5)$  model, such a state would correspond to a rotationally symmetric state where hole pair occupied plaquettes alternate with empty plaquettes (see Fig. 5.9). However, these spatial modulations have not been reproduced by the original projected- $SO(5)$  model. But, as presented in this chapter, the projected- $SO(5)$  model can be extended in a natural way, in order to incorporate also charge ordering.

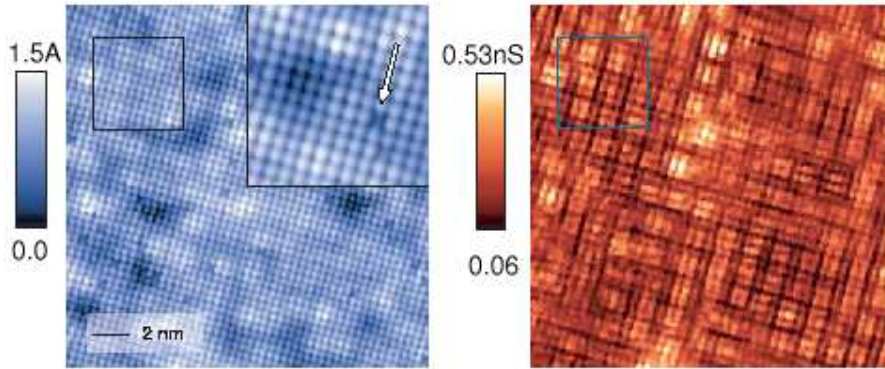


Figure 5.1: STM picture of underdoped  $Ca_{2-\delta}Na_{\delta}CuO_2Cl_2$  ( $\delta = 0.1$ ). **Left:** High resolution topograph of the cleaved  $CaCl$  plane of a crystal with  $\delta = 0.1$ . The perfect square lattice without discernible bulk or crystal reconstructions is seen. **Right:** The conductance map at  $E = 24meV$  in the field of view of the left picture. One can clearly identify strong modulations with  $4a_0 \times 4a_0$  commensurate periodicity plus equally intense modulations at  $4a_0/3 \times 4a_0/3$  and strong modulations at  $a_0 \times a_0$ . Pictures taken from Ref. [26].

## 5.1 The extended projected $SO(5)$ Model

Motivated by the experimental finding of charge-ordered states, it appears quite natural to add further (longer-ranged Coulomb) interactions to the projected- $SO(5)$  model, that may account for these additional phases. Recalling the results from Chap. 2, it appears indeed natural to add the quartic terms defined in Eq. (2.12) and, thereby, recover the full effective Hamiltonian (see Eq. (2.9)) constructed using the Contractor-Renormalization Group analysis [23]. On the other hand, adding further interactions to a Hamiltonian

can deeply change its physics and thereby may have an unexpected influence on the phase diagram. From this point of view, it seems desirable to add the further extensions to the projected- $SO(5)$  model ‘step by step’. The advantage is obvious: The origin of additional phases and effects in the phase-diagram can be understood in terms of the extra interactions and their competition with the interactions of the ‘pure’ model. For this reason, only the longer-ranged repulsion of the hole pairs is added here, which can physically be motivated by the fact that the Coulomb interaction decays only like  $1/r$ . The Hamiltonian studied in this chapter then reads [30]:

$$\begin{aligned} \hat{H} = & (\Delta_c - 2\mu) \sum_i b_i^\dagger b_i + \Delta_s \sum_i t_{\alpha,i}^\dagger t_{\alpha,i} \\ & - J_c \sum_{\langle i,j \rangle} (b_i^\dagger b_j + h.c.) + \sum_{\langle i,j \rangle} J_s (t_{\alpha,i}^\dagger + t_{\alpha,i}) (t_{\alpha,j}^\dagger + t_{\alpha,j}) \\ & + V_c \sum_{\langle i,j \rangle} \hat{n}_{c,i} \hat{n}_{c,j} + V'_c \sum_{\langle\langle i,j \rangle\rangle} \hat{n}_{c,i} \hat{n}_{c,j} \end{aligned} \quad (5.1)$$

This model is named ‘extended projected- $SO(5)$  model’ (or briefly *ep* $SO(5)$  model). The same conventions as introduced in Chap. 2 are used. These are:  $b_i^\dagger$  ( $b_i$ ) creates (annihilates) a hole pair boson on lattice site  $i$  and  $t_{\alpha,i}^\dagger$  ( $t_{\alpha,i}$ ) creates (annihilates) a triplet with spin projection  $\alpha$  on site  $i$ , here  $\hat{n}_{c,i}$  is the hole-pair number operator on site  $i$ . Sums indexed with  $\langle i, j \rangle$  ( $\langle\langle i, j \rangle\rangle$ ) cover all pairs of (next-) nearest neighbor sites ( $i, j$ ). The quasi-particles obey a local hardcore constraint (see Eq. (2.13)).

In this chapter, the studies are focused on the ground-state properties of the extended projected- $SO(5)$  model on a two-dimensional square lattice. Again, the *Stochastic Series Expansion* (SSE) is applied. Unfortunately, the SSE does not allow to access the ground state directly. As a consequence one has to make sure that the temperature in the simulations is sufficiently low, i.e., the thermal fluctuations are mainly frozen out, and do not affect the system’s behavior substantially. In this case the quantum fluctuations dominate and the physics is governed by the ground-state properties. In order to determine the necessary temperature regime, one may consider the energy per site ( $E$ ) as a function of the inverse temperature  $\beta$ . If  $E(\beta)$  is converged with increasing inverse temperature, one may be optimistic to be in the relevant temperature regime (see Fig. ??). This is, of course not, sufficient. As it will be shown in Sec. 5.3.2, the low-energy states can be quasi-degenerate, hence an infinitesimal change in  $E$  can be accompanied by a change in the order parameters. Thus, it is essential to make sure that the order parameter under consideration, as a function of  $\beta$ , is converged. In an additional step (like in the preceding chapter), a finite-size scaling has to be performed in order to obtain the results for a system with infinite size, necessary for spontaneous symmetry breaking. A differ-

ence in the analysis is introduced by the change from a 3D- to a 2D-system, because the Mermin-Wagner theorem [126] does not allow spontaneous symmetry breaking in 2D for continuous symmetries at finite temperatures. Therefore, before presenting the numerical results, a brief discussion how to access the different phases with the SSE technique, is provided.

## 5.2 Excuse: Phase Transitions in 2D-Systems

### 5.2.1 Detecting Superconductivity in 2D-Systems

As already mentioned above, the Mermin-Wagner theorem states, that one cannot observe spontaneous symmetry breaking of a continuous symmetry in 2D at finite temperatures. In addition, Hohenberg [127] specified the statement, proving that the expectation value of the superfluid-order parameter for one- and two-dimensional superfluids is zero (at  $T > 0$ ), if the  $f$ -sum rule [128] is valid. However, he does not make any statement about the existence of a phase transition. In a subsequent work, Kosterlitz and Thouless (KT) associated a change in the decay behavior of a  $U(1)$  correlation function  $C(i)$  from exponential ( $C(\vec{r}) \propto e^{-a|\vec{r}|}$ ) to power-law decay ( $C(\vec{r}) \propto |\vec{r}|^{-\tau}$ ) in 2D-systems with a phase transition [129], later referred to as a KT-transition or KTB-transition.<sup>1</sup> It is pointed out here that a power-law decaying correlation function does not imply a non-vanishing order parameter (if  $\tau \geq 2$ ). This becomes obvious when recalling the definition of an order parameter  $\Delta$  as a function of its corresponding correlation function  $C(i)$ :

$$\Delta = \lim_{N_s \rightarrow \infty} \frac{1}{N_s} \sum_i^{N_s} C(i), \quad (5.2)$$

where  $N_s$  is the volume of the system, and the  $i$  label the lattice sites. Therefore, a KT-phase transition does not conflict with the Mermin-Wagner theorem, because a power-law decaying correlation function results in a vanishing order parameter, thus no symmetry-breaking appears.

In the case of the  $epSO(5)$  model on a square lattice, the existence of a SC phase can be detected via a KT-transition, i.e, by measuring the decay behavior of the SC correlation function  $C_h(r_i)$ , defined as

$$C_h(r_i) = \left( b_i^\dagger - b_i \right) \left( b_0^\dagger - b_0 \right). \quad (5.3)$$

If  $C_h(\vec{r}_i)$  decays like  $|\vec{r}_i|^{-\tau}$ , with  $\tau > 0$  the system is SC, if  $C_h(\vec{r}_i)$  decays like  $e^{-a|\vec{r}_i|}$  the system is not. Here  $|\vec{r}_i|$  denotes the distance between the sites  $i$  and 0. A reliable distinction

<sup>1</sup>KTB stands for Kosterlitz, Thouless and Berezinskii, the later published [130] his results three years before Kosterlitz and Thouless.

between these two behaviors requires a finite-size scaling of large system sizes as well, as efficient estimators for  $C_h(\vec{r}_i)$ . A more accurate determination of the KT transition can be accomplished using the fact that a KT transition, apart from the change in the decay behavior, also shows a jump in the superfluid density to some finite value. This simplifies the distinction between the two phases considerably, because the superfluid density can be measured in an extremely efficient way via SSE by simply counting the charge winding number [131].

### 5.2.2 Antiferromagnetic Order in 2D-Systems

Long-range antiferromagnetic (AF) order, also breaks a continuous symmetry (namely  $SO(3)$ ) and can, therefore, not occur in two-dimensional systems at finite temperature. The argumentation of Kosterlitz and Thouless applies to U(1) order parameters. But, one can ‘cure’ this by regarding the inverse temperature  $\beta$  as third dimension. If one recalls, that the numerical effort of the SSE simulations scales with  $\beta \cdot \prod_{\alpha} L_{\alpha}$ , where the  $L_{\alpha}$  denote the edge lengths of the lattice, it becomes clear that the inverse temperature  $\beta$  has a significance similar to the space directions, i.e., the simulation time scales like the volume of the hypercube space spanned by the cluster edges and the inverse temperature.

Considering the inverse temperature as a dimension is very convenient, when aiming at the ground-state properties of the 2D extended projected- $SO(5)$  model: The limit  $T \rightarrow 0$  corresponds to  $\beta \rightarrow \infty$ , thus by considering the ground-state properties one performs the step to the infinite system ‘automatically’, thereby fulfilling the other condition to observe spontaneous symmetry breaking.

In conclusion, a phase transition to a long-range AF ordered state can be detected, if  $\beta$  as well as the lattice size, determined by the  $x$  and  $y$  edge lengths of the lattice are scaled to infinity. A schematic representation is shown in Fig. 5.2.

Plotting the AF order as a function of the inverse temperature, yields a nice convergence already in the numerically accessible temperature regime. An example is shown in Fig. 5.3. Therefore, in this chapter the measured values for the AF-correlation function at sufficiently low temperatures have been taken directly as  $T = 0$  extrapolated data. In a subsequent step, a finite size scaling (e.g. in Fig. 5.6) is used to extrapolate the system to the thermodynamic limit. Even if the AF-correlation function seems to be converged at  $\beta = 5J_s^{-1}$ , the results presented in this chapter have been obtained choosing  $10 \leq \beta J_s \leq 20$ . This makes sure, that the thermal fluctuations are frozen out as numerically possible.

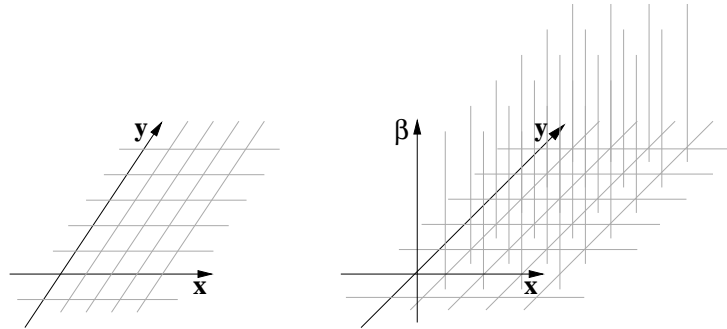


Figure 5.2: In two dimensional systems spontaneous symmetry breaking of the  $SO(3)$  symmetry is not possible, as stated by the Mermin-Wagner theorem. However, the inverse temperature  $\beta$  plays a role analogous to a third dimension and in the limit of  $\beta, x$  and  $y \rightarrow \infty$  the system can undergo a phase transition into a state with broken  $SO(3)$  symmetry.

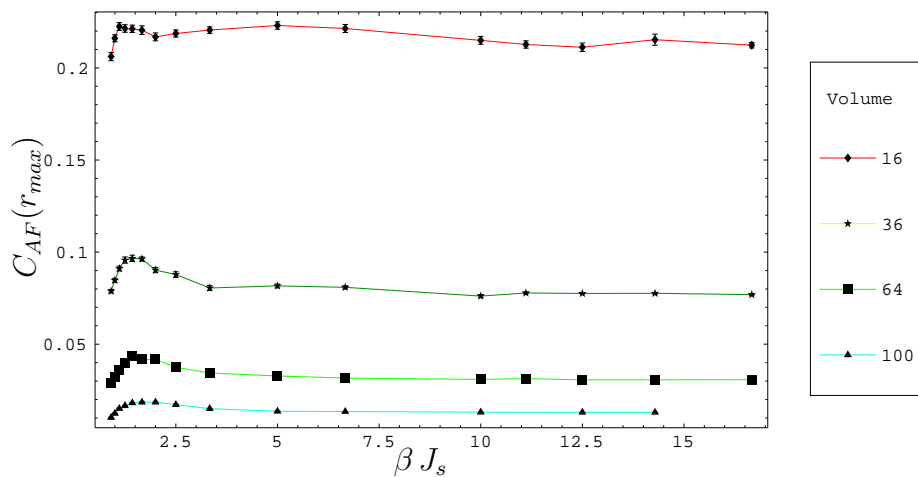


Figure 5.3: Plot of the AF-correlation function as a function of the inverse temperature  $\beta$ . As one can see, convergence is reached already at moderate temperatures. The results presented in this chapter have been obtained choosing  $\beta J_s$  equal to 10 or 20.



There exists also a more mathematical way to show that, for  $T = 0$ , AF order can occur. Requiring only the validity of the  $f$ -sum rule and bosonic commutation relations, Hohenberg showed [127] that:

$$\langle a_{\vec{k}}^\dagger a_{\vec{k}} \rangle \geq -\frac{1}{2} + \frac{T m n_0}{\vec{k}^2 n}, \quad (5.4)$$

where  $a_{\vec{k}}^\dagger$  ( $a_{\vec{k}}$ ) creates (annihilates) a boson with momentum  $\vec{k}$ .  $\hat{n}_0$  ( $\hat{n}_{\vec{k}}$ ) is the number operator for particles with momentum 0 ( $\vec{k}$ ),  $n$  the total boson number and  $m$  denotes their mass. For finite temperature  $T$  and  $D \leq 2$ , this expression is incompatible with:

$$\Omega^{-1} \sum_{\vec{k} \neq 0} \hat{n}_{\vec{k}} = \frac{1}{2\pi} \int d^s k_s \hat{n}_{\vec{k}} = n - n_0. \quad (5.5)$$

This is due to the fact, that insertion of  $n_{\vec{k}}$  from Eq. (5.4) in Eq. (5.5) yields a diverging integral ( $s$  is the dimensionality), i.e. the particle number conservation is violated. For  $T = 0$  the situation is different, because now the second term on the right hand side of Eq. (5.4) vanishes and in 2D the compatibility of the two equations is restored.

This argumentation holds also for superconductivity ( $\vec{k} = 0$ ), i.e., at  $T = 0$  also real long-range superconducting (SC) order can occur in 2D, however due to the possibility of a Kosterlitz-Thouless type of transition already at finite temperature, the scaling  $\beta \rightarrow \infty$  is less crucial. However, one should keep in mind, that looking for the ground-state properties, one has to ensure, that the SC-order parameter is converged as well.

### 5.3 Phase Diagram of the $epSO(5)$ Model in 2D

This section is dedicated to a presentation of the numerical results for the  $epSO(5)$  model. The results have been obtained on two-dimensional square lattices for very low temperatures ( $T \leq 0.1J_s$ ). The finite-size scaling has been performed using lattice sizes ranging from 16 up to 144 sites. The numerical analysis starts, using the parameters proposed in Ref. [30]:

$$\Delta_s = 4.8J_s, \quad \Delta_c = 0, \quad V_c = 4.101J_s, \text{ and } V'_c = 3.6329J_s. \quad (5.6)$$

The energy unit is chosen to be  $J_s$ . For the physically relevant strong-coupling case (Hubbard- $U \approx 8t$ )  $J_s$  can be identified with about  $0.3t$ , i.e.,  $J_s$  is of the order of  $120meV$  (see Fig. 2.4).

In Fig. 5.4, the  $T \rightarrow 0$ , i.e.,  $\beta \rightarrow \infty$  extrapolated phase diagram is plotted. Apart from the AF phase, the results presented here agree well (within error bars) with the data obtained in Ref. [30]. What is the reason for the discrepancy in measuring long-range

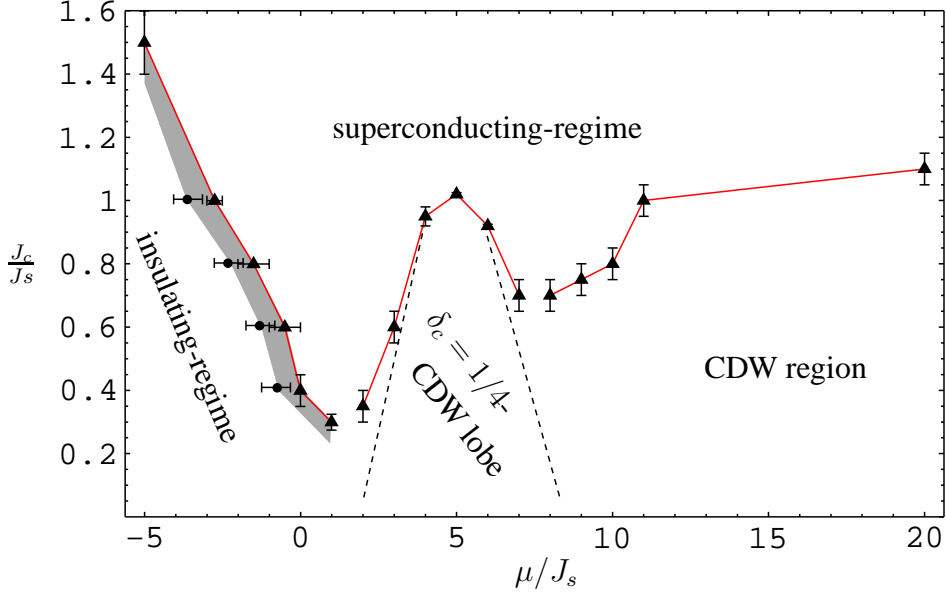


Figure 5.4:  $T=0$  phase diagram of the  $epSO(5)$  model. Below the “ $\delta_c = 1/4$ -CDW lobe”, indicated by the dashed lines, the system shows “checkerboard”-charge order (defined in Eq. 5.9) with a filling of  $\delta_c = 1/4$ . The dashed lines are approximate and are guides to the eyes. In the shaded area, a small but finite hole-pair density is observed, indicating “metallic” behavior. The solid lines connect the data.

AF order? In Ref. [30], the spin-stiffness was measured by counting winding numbers. However, in Appendix A, it is shown that the triplet-winding number cannot be accessed in the framework of the operator-loop-update mechanism [63], used here. Therefore, in the present chapter, the static AF-correlation function  $C_{AF}(r_i)$  for the maximum possible distance ( $r_{max}$ ) in each lattice is calculated. Subsequently, a finite-size scaling to infinite-system sizes is performed. The correlator  $C_{AF}(r_i)$ , where  $r_i$  denotes the distance between sites 0 and  $i$ , reads:

$$C_{AF}(r_i) = \sum_{\alpha=x,y,z} \left\langle \left( t_{\alpha,i}^\dagger + t_{\alpha,i} \right) \left( t_{\alpha,0}^\dagger + t_{\alpha,0} \right) \right\rangle \Big|_{\Delta\tau=0} \quad (5.7)$$

If  $(\lim_{r_i \rightarrow \infty} C_{AF}(r_i)) > 0$ , then the AF-order parameter  $|\vec{N}_{\text{Néel}}|$ , defined as

$$|\vec{N}_{\text{Néel}}| = \frac{1}{N_s} \sum_i C_{AF}(r_i), \quad (5.8)$$

does not vanish. An example for such a finite size scaling is depicted in Fig. 5.6. This figure shows that AF order is obtained only for  $\Delta_s \lesssim 4J_s$ .

But why is long-range AF order not established for  $\Delta_s \gtrsim 4J_s$  and, thus, also for the parameters of Ref. [30], i.e.,  $\Delta_s = 4.8J_s$ ?

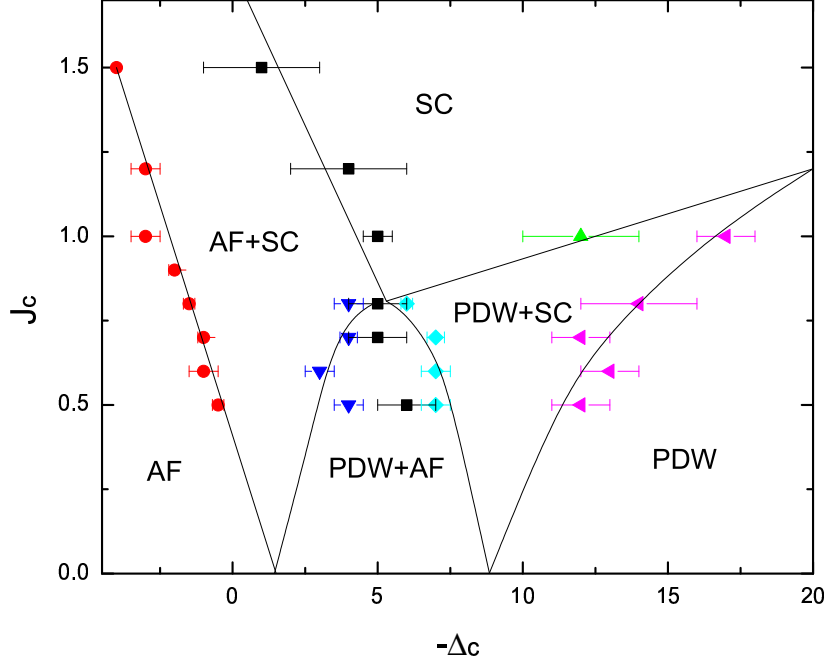


Figure 5.5: Ground state phase diagram of the  $epSO(5)$  model as a function of  $\mu$  and  $J_c$ , obtained by Chen and coworkers [30]. They claim to have found also an AF phase, that has not been reproduced by the calculations presented in Fig. 5.4. The energies are in units of  $J_s$  and PDW is an abbreviation for ‘pair-density wave’.

The numerical results in Refs. [20, 19] and the mean-field results of Chen, Capponi et al. [30] strongly suggest that the  $epSO(5)$  model should display long-range AF order, in the case of a negligible hole pair density ( $\mu < 0$ ,  $J_c < 1J_s$ ). In this case, the  $epSO(5)$  model and the projected- $SO(5)$  model should show exactly the same behavior, i.e., AF order. However, a closer look at the parameters chosen for the simulations of the  $epSO(5)$  model reveals that at  $\Delta_s = 4.8J_s$  the triplet density  $\delta_s = \sum_{\alpha} \langle t_{i,\alpha}^{\dagger} t_{i,\alpha} \rangle$  is rather low ( $\delta_s \approx 0.048$ ). Thus, only every  $\approx 20^{th}$  site is occupied by some triplet and the missing AF order can be reduced to the simple explanation, that the mean distance between two triplets is bigger than the range of the effective interaction. This is documented in Fig. 5.6, which shows that the AF-correlation function  $C_{AF}(r)$  scales to zero for  $\Delta_s = 4.8J_s$ . On the other hand, long-range AF order is found for triplet densities larger than 0.05 (see Fig. 5.7).

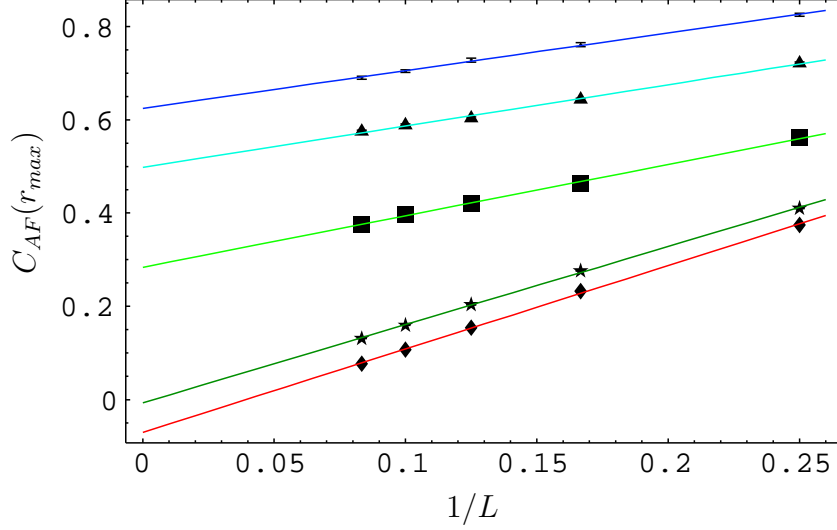


Figure 5.6: Finite-size scaling of  $C_{AF}(\vec{r}_{max})$  for several chemical magnon potentials  $\Delta_s \in \{2, 3, 4, 4.8, 5\}$ , keeping  $J_c = 0.4$ ,  $\mu = 0$  and  $T = 0.1$ . The lines are a least square fits of  $C_{AF}(\vec{r}_{max})$ . The symbols indicate  $\Delta_s$  as follows:  $\bullet$  : 2,  $\blacktriangle$  : 3,  $\blacksquare$  : 4,  $\star$  : 4.8,  $\blacklozenge$  : 5. Here all energies are given in units of  $J_s$ , the error bars are smaller than the symbols.

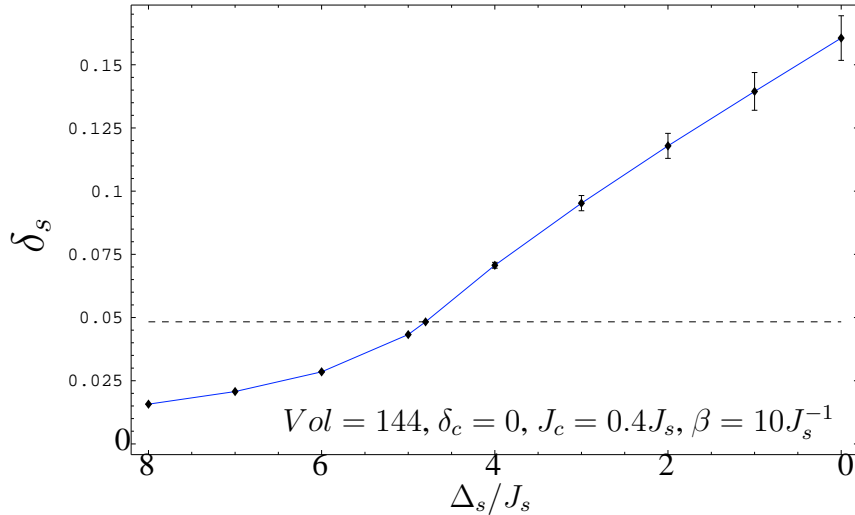


Figure 5.7: Triplet density as a function of  $\Delta_s$ . If the error bars are not explicitly drawn, they are smaller than the size of the symbols. The dashed line indicates the critical triplet density, above which long-range AF order is observed. The solid line connects the data.

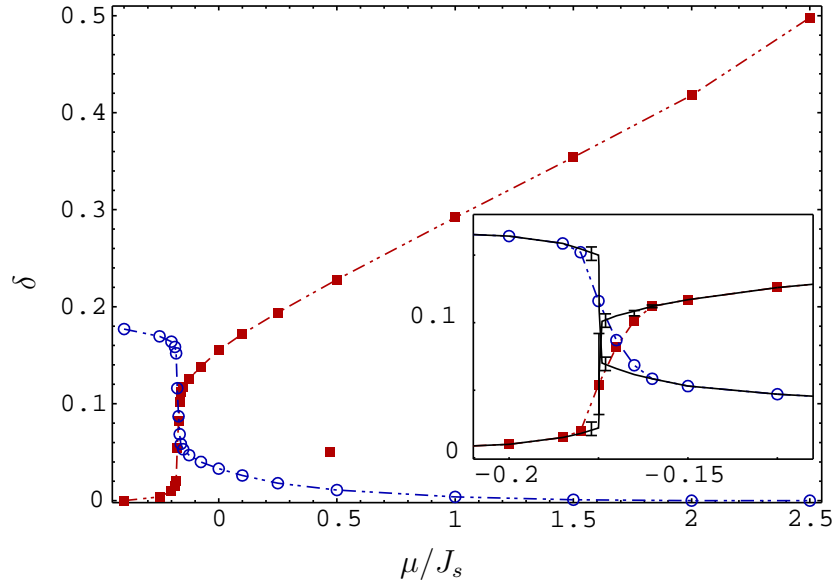


Figure 5.8: Hole concentration  $\delta_{hole} = \delta_c/2$  (filled squares) and magnon density  $\sum_{\alpha} \frac{1}{2} \langle t_{\alpha}^{\dagger} t_{\alpha} \rangle$  (circles) as a function of the chemical potential  $\mu$  at  $T/J = 0.03$  for the projected- $SO(5)$  model (see Eq. (3.18)). The plotted points result from a finite-size scaling with lattice sizes  $V = 10 \times 10$ ,  $14 \times 14$  and  $20 \times 20$ . The small inlay shows a detailed view to the  $\mu$  region in which the hole-pair density jumps to a finite value. The additional solid lines with error bars are  $T = 0$  data obtained from a simultaneous scaling of  $\beta \rightarrow \infty$  and  $V \rightarrow \infty$  (with lattice sizes of  $V = 8 \times 8$ ,  $10 \times 10$ ,  $12 \times 12$ ,  $16 \times 16$ ,  $20 \times 20$  and  $\beta = 4.8, 7.5, 10.8, 19.6$ , and 30). Data taken from Ref. [56].

To conclude this issue: The  $epSO(5)$  model shows long-range AF order like expected, but only if the triplet density is larger than 0.05 and not for the choice of parameters suggested in [30].

In the following sections, the parameter regime defined in Eq. (5.6) is considered, i.e., in the studies of the checkerboard order, the AF ordered state is not explicitly taken into account. This is justified by earlier studies in Ref. [20], which demonstrate that the magnon density decays rather rapidly with increasing charge carrier density beyond the AF regime [100, 20]. For the ranges of  $\delta_c$  studied in this chapter, the magnon density is extremely small and thus negligible (see Fig. 5.8). Within mean-field this is automatically fulfilled, since then the magnon density  $\delta_s = \langle t_{\alpha,i}^\dagger t_{\alpha,i} \rangle$  vanishes identically at some  $\mu_c$ , where  $\mu_c$  marks the onset of finite  $\delta_c$  [100].

### 5.3.1 Doping Dependence of the Checkerboard Order

The recently reported checkerboard order in the  $epSO(5)$  model [30], offers a natural explanation of the scanning tunneling microscopy (STM) results of on  $\text{Bi}_2\text{Sr}_2\text{CaCu}_2\text{O}_{8+\delta}$  and  $\text{Ca}_{2-x}\text{Na}_x\text{CuO}_2\text{Cl}_2$  compounds [29, 28, 27, 25]. These experiments show rotationally symmetric  $4a_0 \times 4a_0$  charge ordering patterns. As depicted in Fig. 5.9, the charge modulations on the original copper-oxide plane correspond to checkerboard order in terms of the coarse-grained boson-plaquette model [23], if one colors a plaquette occupied with a hole pair white and all other possible occupations black [30]. Starting from a charge-ordered checkerboard state, one can iteratively construct new checkerboard ordered states for a variety of dopings by simply coloring half of the “white” (i.e., Cooper-pair) plaquettes black. The new state obtained by such an iteration has a new hole-pair density  $\delta'_c = 1/2 \delta_c$ . Starting, for example, with a checkerboard state associated to hole-pair doping  $\delta_c = 1/2$  (equivalent to a hole doping of  $1/4$  in the original copper-oxide plane) the newly generated state has  $\delta'_c = 1/4$  ( $1/8$ ). The process of painting half of the “white” plaquettes black can be repeated and in the next step one obtains again a checkerboard state with half of the previous Cooper-pair density. But there exists also a second possibility of generating checkerboard states: One can simply paint half of the newly colored black squares white again. In the example chosen above, starting at  $\delta_c = 1/4$ , this leads to commensurate hole pair doping of  $3/8$  (equiv. to hole doping of  $3/16$ ).

Recently, Komiya and coworkers measured systematically the doping dependence of the charge carrier mobility [33]. Their observations suggest that at particular doping levels the hole pair motion seems to be hindered. They identify these doping levels with exactly the fractions (or ‘magic numbers’), for which one can construct the checkerboard states, i.e.,  $\delta_{hole} = 1/16, 3/32, 1/8$  and  $3/16$ , Komiya et al. suggest that charge ordering is

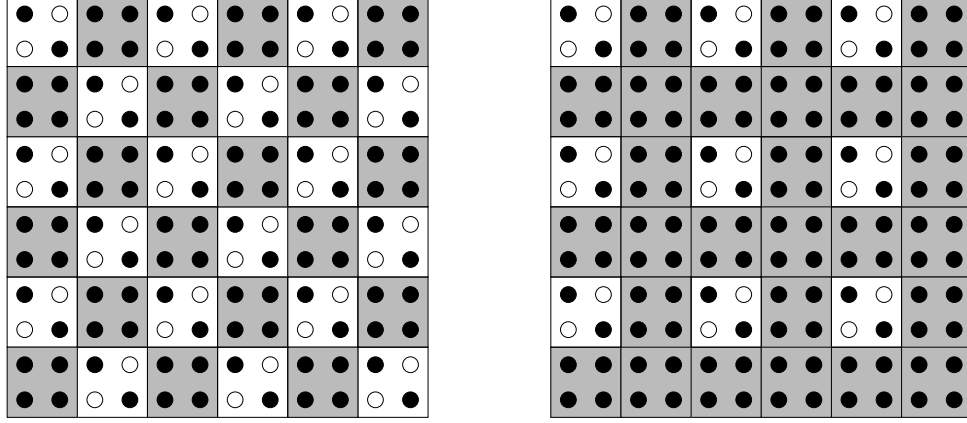


Figure 5.9: Rotationally symmetric  $4a_0 \times 4a_0$  charge modulation, in terms of the boson-plaquette model. The grey boxes represent plaquettes in the half-filled singlet ground state, and the white boxes the Cooper-pair plaquettes. In the left lattice, half of the white plaquettes have been replaced by black ones, leading again to a checkerboard ordered state.

the mechanism behind the reduced Cooper-pair mobility. In principle, 1D-stripes as well as 2D-checkerboard order could explain the commensurate doping fractions, but the 1D-stripes would lead to  $2a_0 \times 2pa_0$  charge unit cells, where  $p$  is two times the hole doping. However, the STM experiments observe a rotationally invariant  $4a_0 \times 4a_0$  charge ordering, thus the 1D-stripe case can be excluded.

Motivated by these findings checkerboard order is here studied as function of  $\mu$  for  $J_c = 0.3J_s$ , using the static charge-density wave (CDW) correlation function  $C_{CDW}(\vec{k})$ :

$$C_{CDW}(\vec{k}) = \langle \hat{n}_c, \hat{n}_c \rangle(\vec{k}) \Big|_{\Delta\tau=0}, \quad (5.9)$$

checkerboard order corresponds to  $\vec{k} = (\pi, \pi)$ , and stripe order to  $\vec{k} = (0, \pi)$  as well as  $\vec{k} = (\pi, 0)$ . As shown in Fig. 5.10, which plots  $C_{CDW}(\vec{k} = (\pi, \pi))$ , it is found that the checkerboard order parameter is peaked around the commensurate dopings of  $\delta_c = 1/2$  ( $\mu \approx 17.5J_s$ ),  $1/4$  ( $\mu \approx 5J_s$ ),  $1/8$  ( $\mu \approx 1.2J_s$ ) and  $3/8$  ( $\mu \approx 12.5J_s$ ).

Besides the ‘domes’ or maxima in the checkerboard-order parameter in Fig. 5.10, also plateaus in the density against the chemical potential  $\mu$  are found (see Fig. 5.11). These plateaus are, in principle, similar to the plateaus observed in the density (as a function of the chemical potential) of ‘true’ bosons in the Bose-Hubbard model. In the Bose-Hubbard model, the plateaus are observed at integer fillings and indicate Mott insulating behavior. The reason for the Mott insulating regime in the Bose-Hubbard model is the huge on-site interaction, causing an energy penalty of the order of the Hubbard- $U$  for delocalization at integer filling factors. The situation is rather different for the extended hardcore-boson

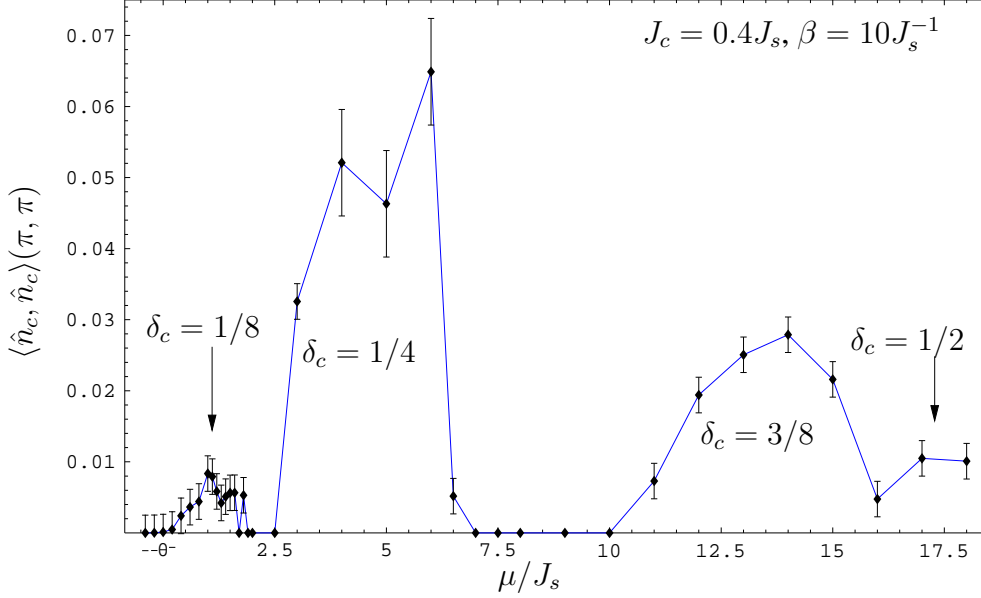


Figure 5.10: Checkerboard-order parameter as function of the chemical potential  $\mu$ , for the parameters  $J_c = 0.3J_s$ ,  $\Delta_s = 4.8J_s$  and  $T = 0.1J_s$  extrapolated to the infinite system. The sizeable error bars are due to the rather low value of  $J_c$  (where the autocorrelation time grows significantly). However, for small  $\mu \approx 1.2J_s$  corresponding to  $\delta_c \approx 1/8$ , one can clearly identify a peak in the particle-particle correlation function  $\langle \hat{n}_c, \hat{n}_c \rangle(\pi, \pi)$ . Also checkerboard order for chemical potentials corresponding to  $1/2$ ,  $1/4$  as well as  $3/8$  doping is observed. The line connects the data.

projected- $SO(5)$  model, studied here: In this case, the off-site potentials  $V$  and  $V'$  are the reason for the reduced hole-pair mobility. For example, if  $\delta_c = 1/2$ , the energy penalty for one particle to leave the energetically optimized checkerboard configuration is  $\approx V - V'$ . At lower doping fractions, this penalty of leaving the checkerboard configuration can be even higher: At  $\delta_c = 1/4$  the energy penalty for delocalization is equal to  $V$  or  $V'$  depending on the new position. When also  $\delta_c = 1/8$  is considered, the situation changes again: The average free path for a particle, before it approaches to another particle and gets effectively ‘pushed’ back to its energetically optimized position in the charge ordered pattern, is bigger than for higher doping fractions. Thus, the propensity for checkerboard ordering at  $\delta_c = 1/8$  is lower than it is for higher doping fractions. This is supported by the results in Fig. 5.10, showing that the order parameter is much lower for  $\delta_c = 1/8$  than it is for  $\delta_c = 1/4$ .

In conclusion, the calculation of the checkerboard-order parameter as a function of the chemical potential reproduces salient features of the experimental findings by Komiya



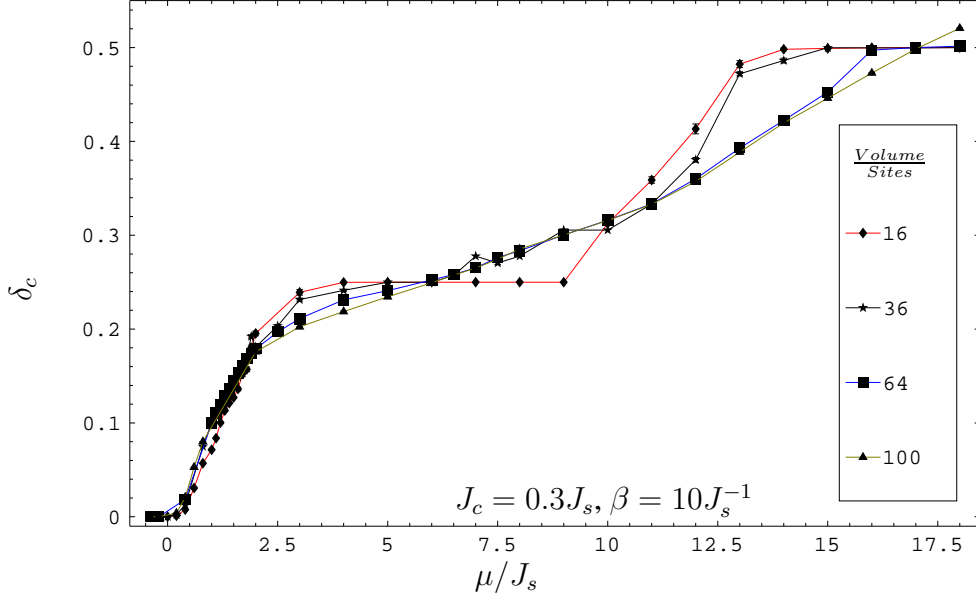


Figure 5.11: Hole pair density vs.  $\mu$  for the same parameters as in Fig. 5.10. The plateaus indicate Mott insulating behavior. The notion of a Mott insulator is usually restricted to insulating behavior caused by on-site interaction at integer filling factors. But as discussed in Refs. [30, 23], the  $epSO(5)$  model can be interpreted as an effective Hamiltonian generated from the one band Hubbard model. In this sense, the plateaus indicate correlation induced insulating ‘Mott’ phases. A more precise discussion is provided in the text.

and coworkers [33]: Insulating lobes at commensurate doping fractions  $\delta_c = 1/2, 1/4, 1/8$  and  $3/8$  with non-vanishing checkerboard order are found. In terms of the copper-oxide plane, these doping fractions  $\delta_c$  correspond to half of the original hole-doping fraction  $\delta_{hole}$ , i.e.,  $\delta_{hole} = 1/4, 1/8, 1/16$  and  $3/16$  observed experimentally. In addition, the  $epSO(5)$  model permits a microscopic understanding of the insulating plateaus at commensurate dopings levels.

### 5.3.2 Detailed Investigation of the CDW to SC Transition on Top of the $\delta_c = 1/4$ insulating Lobe

In this section, a detailed discussion of the properties of the  $\delta_c = 1/4$  insulating lobe (see Fig. 5.4) is provided. The top of this lobe is of special interest, because it is a possible candidate for  $SO(5)$ -symmetry restoration [30], if the chemical potential of the triplets ( $\Delta_s$ ) is chosen appropriately. Here, like discussed in Sec. 5.3, the case without long-range AF order ( $\Delta_s = 4.8J_s$ ) is considered. First, the phase transition from checkerboard to SC

order is classified. In the second part, the temperature dependence of the checkerboard-order parameter is studied.

### Nature of the phase transition

The distinction between first- and higher-order phase transitions based on numerical simulations is a cumbersome issue. This is, because the autocorrelation time increases close to phase transitions, thereby reducing the achievable precision. On the other hand, the type of a phase transition in a model Hamiltonian is an important information, which can be checked experimentally in some cases. Therefore, in Fig. 5.12 the SC- and the checkerboard-order parameters, obtained by an extrapolation to the infinite system, keeping  $\mu = 5J_s$  and  $T = 0.1J_s$  constant, are plotted against  $J_c$ . Thereby, the behavior of the order parameters passing the phase transition on top of the  $1/4^{th}$  insulating lobe (see Fig. 5.4) is studied. In order to compare both order parameters in one graph, the checkerboard-order parameter has been scaled by a factor of 200. Both order parameters seem to emerge continuously, indicating a second or higher-order phase transition. Unfortunately, the first order case cannot be safely excluded (on the basis of the results of Fig. 5.12 only), due to the statistical errors of the SSE simulation and the errors introduced by the subsequent finite-size scaling.

For this reason also a second criterion to distinguish between a first- and second-order phase transition is considered, i.e, the continuity of the first derivative of the free energy  $\frac{\partial F}{\partial J_c}$  (Ehrenfest criterion). It is straight-forward to show that,

$$\frac{\partial F}{\partial J_c} = \left\langle \frac{\partial \hat{H}}{\partial J_c} \right\rangle = \sum_{\langle i,j \rangle} \langle b_i^\dagger b_j + h.c. \rangle . \quad (5.10)$$

Thus, measuring the static correlation function  $\langle b_i^\dagger b_j + h.c. \rangle$ , ( $\langle i, j \rangle$  as usual denotes pairs of next-neighbor sites) allows to access directly  $\frac{\partial F}{\partial J_c}$ . The results are shown in Fig. 5.13. Even if the slope gets steeper with increasing system size, it converges within the accessible regime, and a continuous behavior of  $\frac{\partial F}{\partial J_c}$  is observed, indicating indeed a second-order (or higher) phase transition.

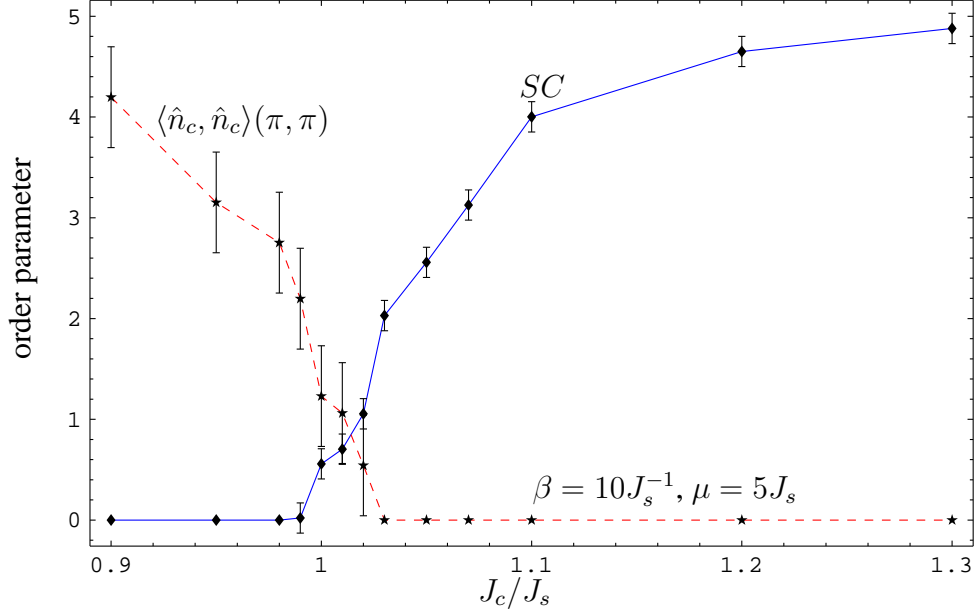


Figure 5.12: Superconducting (charge-winding number) and checkerboard-order parameter extrapolated to the infinite lattice as a function of  $J_c$ . The error bars are estimates obtained from the finite size scaling. The checkerboard-order parameter has been scaled by factor of 200. ( $\beta J_s = 10, \mu = 5J_s$ ) Lines are guides to the eyes.

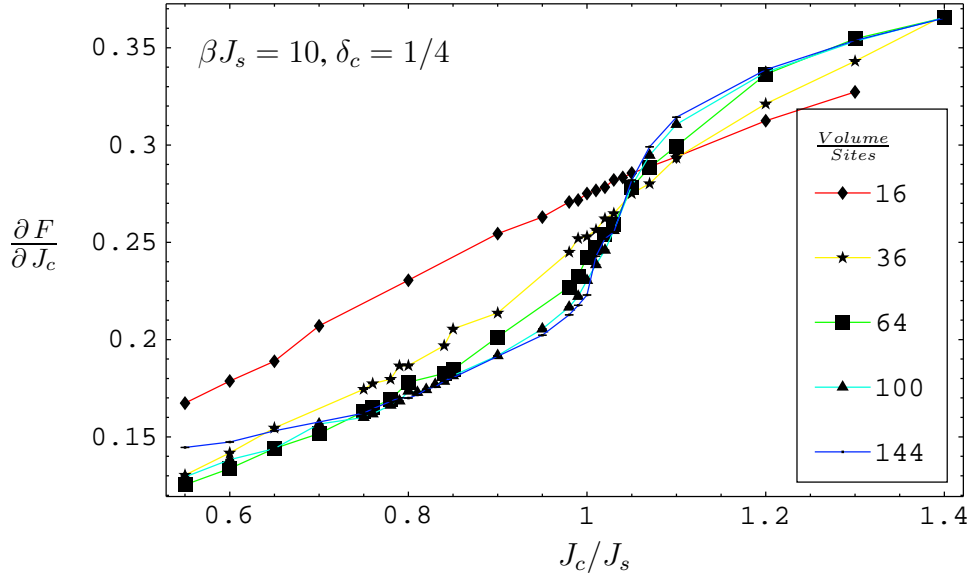


Figure 5.13: Scan of  $\frac{\partial \hat{F}}{\partial J_c}$  as a function of  $J_c$  for lattice sizes listed in the inset, choosing  $\mu = 5J_s$  corresponding to  $\delta_c = 0.25$ . The continuity of  $\frac{\partial \hat{F}}{\partial J_c}$  excludes a first-order phase transition. The lines are guides to the eyes.

### Reentrance behavior

Next, the temperature dependence of the checkerboard-order parameter is presented. In order to keep  $\delta_c = 1/4$  constant, canonical calculations at  $J_c = 1.05J_s$  are employed. Thus, the parameters are chosen such that the system is simulated exactly above the  $1/4^{\text{th}}$  insulating lobe, where a SC ground state is found (see Fig. 5.4).

With increasing temperature (i.e. approaching  $\beta J_s < 10$  from the right-hand side in Fig. 5.14), the checkerboard order grows in the limit of infinite-system size, until it reaches a maximum. With further increase in temperature ( $\beta J_s < 3$ ), the order parameter disappears again, like it is depicted in Fig. 5.14.

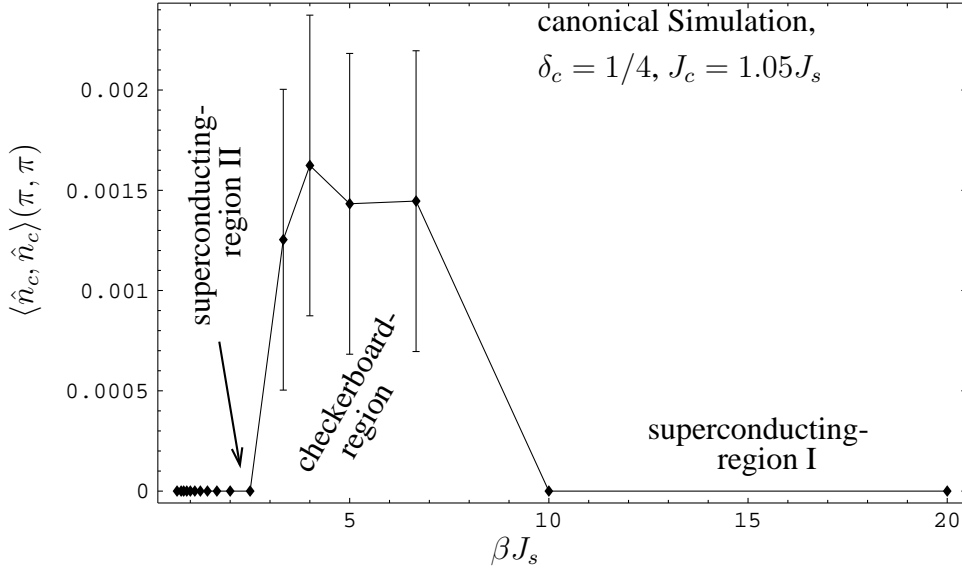


Figure 5.14: Checkerboard-order parameter as a function of  $\beta$ , extrapolated to the infinite lattice. The results have been obtained performing canonical simulations keeping  $\delta_c = 0.25$  and  $J_c = 1.05J_s$ . The line connects the data. When considering low temperatures (i.e.,  $\beta J_s \geq 10$ ) the system is superconducting (see Fig. 5.4). With increasing temperature checkerboard order is observed ( $3 < \beta J_s < 10$ ), which disappears again with further increase of the temperature. From the temperature studies in Sec. 5.2 it is known that SC critical inverse temperature ( $\beta_c$ ) is of about  $2J_s^{-1}$ , thus the checkerboard order disappears in favor of SC.

However, the finite-size scaling of the checkerboard-order parameter is much more difficult here than it is for the AF-correlation function. This causes the significant error bars in Fig. 5.14. In order to nevertheless corroborate the results, also the checkerboard-order parameter is plotted as a function of temperature  $T$  for the finite lattices for which the

calculations have been performed. The curves in Fig. 5.15 all show a maximum, located in the temperature range, where in Fig. 5.14 finite checkerboard-order parameter is observed. This maximum gets more pronounced with increasing system size. Thus, the finite checkerboard-order parameter in Fig. 5.14, located at  $3.3 \lesssim \beta J_s \lesssim 10$ , is not due to statistical errors or finite-size effects, but a consequence of the temperature behavior of the checkerboard-order parameter. These simulations have been performed canonically. Unfortunately, when keeping the hole-pair number fixed, it is not possible to calculate the SC-order parameter. However, from the calculations presented in Fig. 5.4 it is known, that the system has a SC-ground state, i.e., for  $\beta J_s \geq 10$  the system is SC. Furthermore, it is known from the temperature studies discussed in Sec. 5.2, that the SC critical temperature  $T_c$  in that parameter range is of the order of  $\approx 0.5J_s$  (i.e.,  $\beta J_s \approx 2$ ). This is in accordance with calculations presented in Ref. [35]. Based on this argumentation, it is plausible that the SC state recovers when increasing the temperature above the “melting” point of the checkerboard order. A coexistence of checkerboard and superconducting order can be excluded because, according to Ref. [132], such a coexistence is thermodynamically unstable.

This sequence of transitions from SC to checkerboard order and back to SC order as a function of temperature is called “reentrance” behavior. For a related, but simpler bosonic model, this sequence of transitions has also been reported [35].

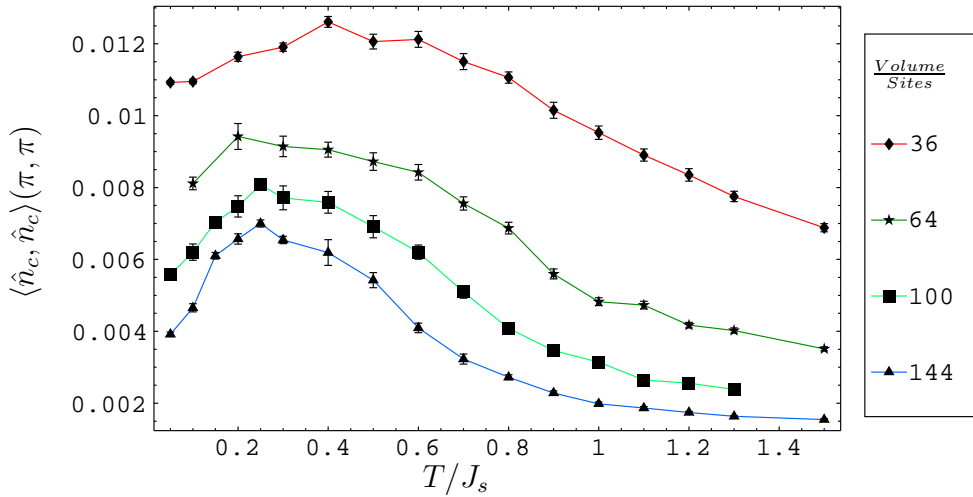


Figure 5.15: Checkerboard-order parameter for different lattice sizes as a function of temperature. The results have been obtained performing canonical simulations, keeping  $\delta_c = 0.25$  and  $J_c = 1.05J_s$ . Here the order parameter is plotted as a function of  $T$ , in order to better display the peak in the temperature regime  $0.15J_s \leq T \leq 0.3$ . The peak structure develops with increasing system size. The lines are guides to the eyes.

### 5.3.3 Beyond HTSC: Supersolid Phase

So far the studies of the  $epSO(5)$  model revealed a variety of different phases: superconducting, antiferromagnetic as well as charge-ordered phases. Originally, the motivation to study the Hamiltonian Eq. (5.2) stems from the physics of the high-temperature superconductors. However, the model can be considered as a more general toy model. The identification of  $b_i^\dagger$  and  $t_{\alpha,i}^\dagger$  with Cooper pairs and magnons is not the only possible interpretation. Identifying the hardcore bosons with different quasi-particles may result in a wider range of applicability for the present  $epSO(5)$  model. One can even go beyond the restriction of representing quasiparticles by the hardcore bosons and identify, for example, the  $b_i^\dagger$  with  ${}^4\text{He}$  atoms. Of course  ${}^4\text{He}$  atoms are ‘true’ bosons, thus multiple particles can have the same quantum numbers, e.g. multiple atoms can occupy the same position. However, the atoms interact strongly. Their interaction has been modeled successfully by the repulsive Lennard-Jones potential, which diverges if the distance between two atoms vanishes. Thus, also here the approximation of representing  ${}^4\text{He}$  by “hardcore” bosons is justified. Moreover,  ${}^4\text{He}$  is believed to be well represented by Jastrow states [133], implying that  ${}^4\text{He}$  has a hard core, is bounded below and has finite range. These properties can be represented well by the  $b_i^\dagger$  bosons in the  $epSO(5)$  model. Recently the research considering  ${}^4\text{He}$  has gained a lot of attraction, caused by experiments of Kim and Chan. They reported that **solid**  ${}^4\text{He}$  can behave like a superfluid [36, 37]. These studies have renewed the interest in a long-standing question: can a supersolid phase – with simultaneous diagonal (i.e., solid) and off-diagonal (i.e., superfluid) long-range order – exist in a bosonic system. Does the  $epSO(5)$  model also provide a supersolid phase? Whereas the checkerboard ( $C_{CDW}(\vec{k} = (\pi, \pi))$ ) supersolid was recently found to be unstable in the specific case of hardcore bosons, a striped supersolid phase with  $C_{CDW}(\vec{k} = (\pi, 0))$  was shown to be stabilized by next-nearest neighbor interactions [132]. Therefore, one may expect a  $C_{CDW}(\vec{k} = (\pi, 0))$  supersolid phase in the  $epSO(5)$  model.

If one changes the interpretation of  $b_i^\dagger$ , such that  $b_i^\dagger$  creates a  ${}^4\text{He}$  atom, one also has to rename the order parameters: superconductivity corresponds to superfluidity and charge order has to be translated into crystalline order. That is in our ‘familiar’ language of HTSC, one would call the coexistence of superconductivity and charge order a supersolid state.

As a matter of fact, the results of the calculation show that the  $epSO(5)$  model contains a supersolid phase: These results are shown in Fig. 5.16, where the SC- and stripe-order parameters are plotted after their extrapolation to the thermodynamic limit for  $\mu = 6J_s$  and  $J_c = 1J_s$  as a function of  $\beta$ . In the accessible temperature regime, the system is “supersolid” for inverse temperature  $\beta J_s \gtrsim 3.3$ . As shown in Fig. 5.17, phase separation can be excluded.

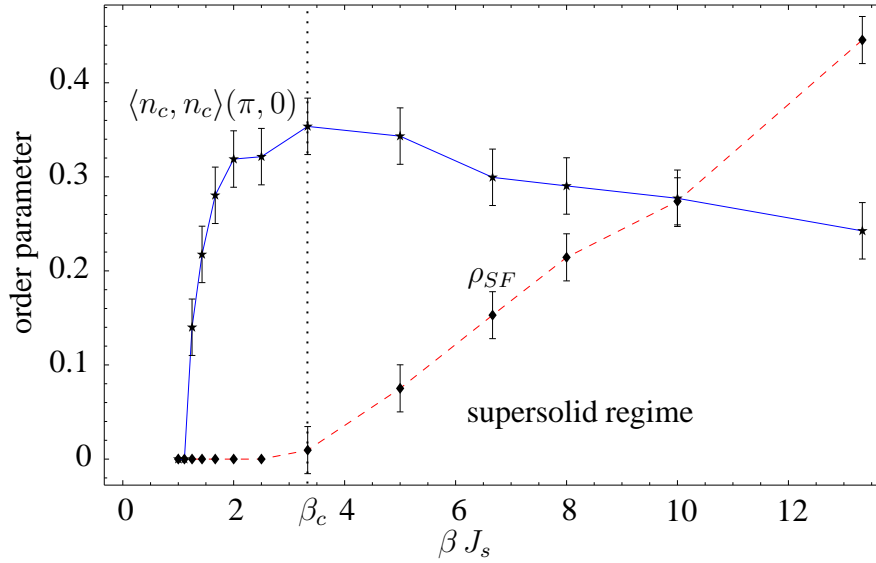


Figure 5.16: Superfluid density ( $\rho_{SF}$ ) and CDW (Stripe) order parameters extrapolated to infinite system size. The dashed line connects the data points of the superconducting order parameter and the continuous line connects data for the CDW order parameter. The lines are guides to the eyes. Again the CDW order parameter has been scaled ( $\times 20$ ), in order to present both order parameters in one graph. The  $\beta$ -range, where both order parameters are finite, i.e.,  $\beta > \beta_c$ , marks the region where the  $epSO(5)$  model shows supersolid behavior. As shown in Fig. 5.17, phase separation can be excluded.

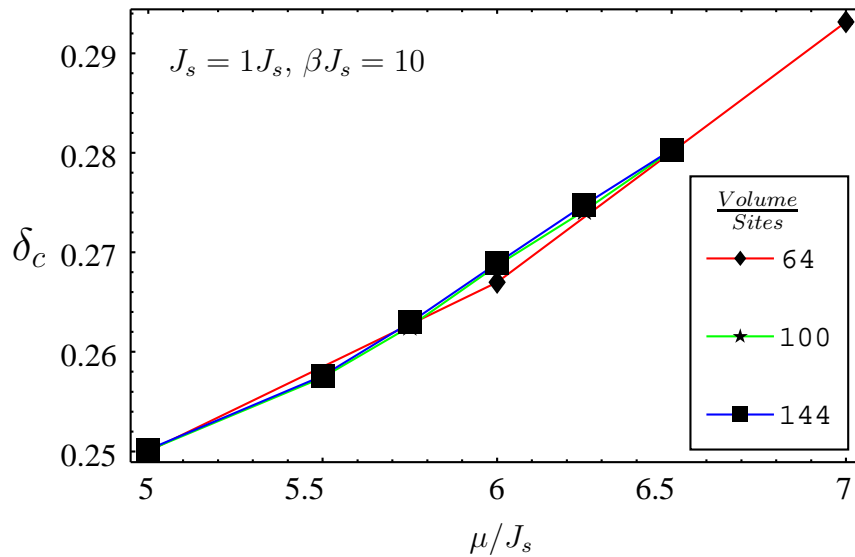


Figure 5.17: Charge carrier density  $\delta_c$  as a function of the chemical potential  $\mu$ . Within the error bars there are no finite size effects. If the coexistence of CDW and SC in Fig. 5.16 would correspond to phase separation,  $\frac{\partial \delta_c}{\partial \mu}$  would vanish, which is not observed here. Therefore, phase separation can be excluded. The lines are guides to the eyes.



## 5.4 Conclusions

In this chapter, a detailed study of the  $epSO(5)$  model's ground state and finite-temperature phase diagram has been presented. First the AF behavior has been clarified, i.e., the model contains long-range AF order only for triplet dopings typically larger than  $\approx 5\%$ . Next, the checkerboard-order parameter as function of doping (for a small value of  $J_c$ ) has been studied. The results show qualitative agreement with experimental data presented in Ref. [33]. In the framework of the  $epSO(5)$  model, a microscopic explanation of the reduced charge mobility has been given. A classification of the transition from checkerboard to SC order as second- (or higher-) order phase transition has been presented. When studying the temperature dependence of these two competing phases, an unusual reentrance behavior was found: the system displays a SC-ground state, while it shows checkerboard order in a finite temperature regime, above which the SC state is restored.

Finally, in Sec. 5.3.3 the  $epSO(5)$  model is considered as more general effective Hamiltonian, where the  $b_i^\dagger$  bosons model  ${}^4\text{He}$  atoms. In this interpretation the  $epSO(5)$  model shows "supersolid" behavior, i.e., coexistence of crystalline order and superfluidity, or diagonal and simultaneously off-diagonal order. This phascinating issue is discussed in the context of the experiments reported in Refs. [36, 37].

# 6

## Summary

---

This thesis contains two major parts: The first part introduces the reader into three independent concepts of treating strongly correlated many body physics. These are, on the analytical side the  $SO(5)$ -theory (Chap. 3), which poses the general frame. On the numerical side these are the Stochastic Series Expansion (SSE) (Chap. 1) and the Contractor Renormalization Group (CORE) approach (Chap. 2). The central idea of this thesis was to combine these above concepts, in order to achieve a better understanding of the high- $T_c$  superconductors (HTSC). The results obtained by this combination can be found in the second major part of this thesis (chapters 4 and 5).

After a brief introduction, the first chapter is dedicated to the SSE technique, on which the numerical analysis of the effective-bosonic Hamiltonians in the second part of this work is based on. This technique belongs to the Quantum-Monte-Carlo approaches, but in contrast to algorithms that rely on a discretization in imaginary time, the SSE is in principle exact. The central ideas and advantages of the *Stochastic-Series Expansion* are pointed out and the operator-loop update is discussed. A central position takes the measurement of correlation functions. Based on the concepts developed by Dorneich and Troyer [63], the measurement of single-particle correlation functions has been enhanced considerably within this thesis. Due to these optimizations, the accessible system sizes grew by one order of magnitude (from  $\approx 5000$  sites at  $T \approx 1J_c$  to  $\approx 10000$  sites at  $T \approx 0.5J_c$ ) [21, 22]. This was a necessary condition to obtain the results presented in chapter 4 and chapter 5, especially when studying the restoration of the  $SO(5)$ -symmetric scaling behavior close to the multicritical-critical point in the global phase diagram (see Sec 4.2).

In addition, in section 1.3.2 a substantial extension of the capabilities of the operator-loop update has been proposed. The implementation of these concepts will make it possible to

measure arbitrary single-particle as well as two-particle correlation functions.

In chapter 2, a fundamentally different approach has been described: The iterative Contractor-Renormalization Group (CORE) technique, which, in spirit, is related to the real-space renormalization group scheme [67, 68]. Its application to the one-band *Hubbard-model* yields in the first step an effective Hamiltonian [23], that captures the low-energy physics of the *Hubbard-model* in terms of its low-lying bosonic excitations, i.e., triplets and hole-pair bosons. This further motivates why these excitations can be considered as necessary ingredients, when aiming for a description of the physics in the copper-oxide planes of the high- $T_c$  superconductors (see Sec. 2.1).

The last chapter of the first part introduces the elegant concept of the  $SO(5)$ -theory of high- $T_c$  superconductivity [17, 18]. It is explained how symmetry principles can be employed to ‘unify’ antiferromagnetism and superconductivity. These two, at first glance, different phases, which are apparent in all high- $T_c$  superconductors, are connected by rotations of a five dimensional superspin. The generators of these rotations are members of the  $SO(5)$ -Lie group. The  $SO(5)$ -theory makes a number of predictions, that can be tested experimentally, e.g., the global phase-diagram and the neutron resonance mode [18]. Unfortunately, the original exact  $SO(5)$ -theory [17] (i.e. on the Hamiltonian level) cannot account for the Mott physics near half-filling, which has been observed experimentally in the high- $T_c$  superconductors. This is due to the energetic degeneracy of states describing hole- and electron-pair quasi-particles in the exact  $SO(5)$ -theory. One escape is to explicitly break the  $SO(5)$ -symmetry on the Hamiltonian level by projecting out the doubly occupied states. This symmetry-breaking on the Hamiltonian level may have been expected, because the Hamiltonian itself does not need to be  $SO(5)$  invariant. The central question is  $SO(5)$ -symmetry restoration, to be possibly detected in the scaling behavior of the order parameters at the low energy level ( $\approx k_B T_c$ ) close to a multicritical point. Already in Zhang’s original exact  $SO(5)$ -theory [17] the  $SO(5)$ -symmetry was explicitly broken by the chemical potential. Zhang, Hu, Hanke, Arrigoni and Auerbach constructed a model, where the Gutzwiller projection has been implemented exactly [100]. Interestingly, the resulting projected- $SO(5)$  model has a large similarity to the effective model motivated by the CORE analysis in chapter 2 (in the physically relevant, strongly interacting parameter regime (Hubbard- $U \approx 8t$ )).

In the second major part of this thesis, these three different approaches towards the physics of the copper-oxide superconductors are combined. The generalized  $SO(5)$ -Hamiltonian (the projected- $SO(5)$  model), that has been motivated by the  $SO(5)$ -theory as well as by the CORE technique, is studied numerically using the *Stochastic-Series*

*Expansion.* In chapter 4, the finite-temperature phase diagram is presented. There, it is shown that the projected- $SO(5)$  model reproduces salient features of the high- $T_c$  superconductors' phase diagram, i.e., an antiferromagnetic Mott insulating phase for low doping and a superconducting phase for larger doping. Even the correct ratio of the Néel and the SC-critical temperature can be reproduced, when adjusting the ratio of the parameters  $J_c$  and  $J_s$  ( $J_c/(2J_s) = 0.225$ ).

In addition, the question of symmetry restoration has been addressed, and the scaling properties of the critical lines close to the bicritical point, where antiferromagnetic (AF) and superconducting- (SC) transition lines meet, have been studied. Although the  $SO(5)$ -symmetry has been broken on the Hamiltonian level, this symmetry is indeed restored in a rather large transient region of the bicritical point [19, 24]. In the present work numerical quantum simulations of lattices of more than 10.000 lattice sites have been made possible, in particular for the projected- $SO(5)$  model. The precision of these calculations and the obtainable system sizes have been necessary prerequisites in order to determine the critical exponents close to the bicritical point.

Motivated by the success of the projected- $SO(5)$  model, this model was further extended by the inclusion of longer ranged Coulomb interactions [30] in order to account also for the competing and experimentally observed charge-order patterns [25, 26, 27, 28, 29]. This extension was studied numerically in chapter 5). It evolves naturally from the CORE analysis [30] and also from the  $SO(5)$ -theory [31]. The numerical analysis of the extended projected- $SO(5)$  model ( $epSO(5)$  model) starts with the calculation of the 2D ground-state phase diagram. The phase diagram contains in addition to the AF and SC also charge-ordered phases. These charge-ordered 'checkerboard states' offer a natural explanation for the recent scanning-tunneling microscopy results of on  $Bi_2Sr_2CaCu_2O_{8+\delta}$  and  $Ca_{2-x}Na_xCuO_2Cl_2$  compounds [25, 26, 27, 28, 29]. The AF phase is not stabilized for the model parameters previously considered in Ref. [30]. The reason for the initially missing AF order has been explained by the fact, that the range of the effective triplet-triplet interaction is lower than the mean distance between triplets. An explanation of the difference between the results presented here and the data given in Ref. [30] has been provided, i.e., the spin stiffness cannot be calculated in the way presented in Ref. [30] (see App. A).

Furthermore, the 'checkerboard-order' parameter as a function of doping has been studied. The results show qualitative agreement with experimental data presented in Ref. [33], namely that the  $epSO(5)$  model shows a propensity for checkerboard ordering at commensurate filling factors of  $\delta_c = 1/2, 1/4, 3/8$  and  $1/8$  ('magic doping fractions' in Ref. [33]). This may account for the experimentally observed reduced charge-carrier mobility, found at exactly these doping fractions. In the framework of the  $epSO(5)$  model, a microscopic explanation of the reduced charge-carrier mobility has been

presented. When studying the temperature dependence of these two competing phases (superconductivity and checkerboard order), for parameters where a SC-ground state has been observed, the calculations show that for a small finite-temperature regime the checkerboard ordering restores.

In section 5.3.3, the  $epSO(5)$  model is considered as a more general effective Hamiltonian: This model permits to interpret the charge bosons  $b_i^\dagger$  also as  ${}^4\text{He}$  atoms. The calculation shows that the model contains coexistence of superfluidity and crystalline order, also referred to as a ‘supersolid state’. Experimentally, a possible observation of supersolid  ${}^4\text{He}$  has recently been reported by Kim and Chan [36, 37].

The main idea of this thesis, i.e., to combine the  $SO(5)$ -theory with the capabilities of bosonic Quantum-Monte Carlo simulations and those of the Contractor-Renormalization Group approach, has been proven to be a very successful Ansatz. Two different approaches, one based on symmetry and one on renormalization-group arguments, motivate an effective bosonic Hamiltonian. In a subsequent step the effective Hamiltonian has been simulated efficiently using the *Stochastic-Series Expansion*. The results reproduce salient experiments on high- $T_c$  superconductors, as explained above. In addition, it has been shown that the model can be extended to capture also charge ordering. These results also form a profound basis for further studies, for example one could address the open question of  $SO(5)$ -symmetry restoration at a multicritical point in the  $epSO(5)$  model, where longer ranged interactions are included.

Although this effective bosonic description has been quite successful it should be pointed out, that the purely bosonic nature of the effective Hamiltonian has still to be further justified. Neglecting fermionic-quasi particles in the simulations may eventually restrict the validity of the studied Hamiltonians as a microscopic attempt towards the theory of high- $T_c$  superconductivity. In the author’s opinion this bosonic approach is justified from a pragmatic point of view, i.e., by its success in describing the global phase diagram as well as other salient features (e.g. neutron-scattering resonance, see Ref. [18]) of the high- $T_c$  superconductors. There is hope that future algorithms and computer techniques might even permit to simulate coupled bosonic-fermionic Hamiltonians at comparable temperatures and system sizes and, thereby, overcome the problems mentioned.

# A

## Detecting Antiferromagnetic Order in SSE-Simulations of the extended-projected $SO(5)$ Model

---

In this section an explanation for the difference between the results presented in Ref. [30] and the results obtained by our QMC calculations (see Sec. 5.3) is provided. The reason for this difference can be explained by two different procedures of measuring antiferromagnetism. In contrast to the procedure employed in this thesis, i.e. measuring directly the antiferromagnetic (AF) -correlation function, Chen and coworkers tried to detect antiferromagnetism using the spin stiffness  $\rho_s$  as an order parameter by counting the triplet-winding number. In the following it will be shown, that in SSE simulations of the  $epSO(5)$  model the triplet-winding number cannot be measured directly, like one usually does for Hamiltonians containing Heisenberg spin-spin interaction.

Starting point of the calculation is the definition of the spin stiffness  $\rho_s$ :

$$\rho_s = \frac{-1}{\beta L^{d-2}} \left. \frac{\partial^2}{\partial \phi^2} \ln(Z(\phi)) \right|_{\phi=0}, \quad (\text{A.1})$$

where  $Z$  denotes the partition function,  $d$  the dimension and  $\phi$  the torsion angle between the spins. Because here only in the spin properties of the  $epSO(5)$  model are of interest, it is sufficient to consider instead of the full Hamiltonian its spin-triplet term  $\hat{H}_{Tri}$ :

$$\hat{H}_{Tri} = J_s \sum_{\langle i,j \rangle, \alpha} n_i^\alpha n_j^\alpha, \text{ where } n_i^\alpha = t_{i,\alpha}^\dagger + t_{i,\alpha}, \quad (\text{A.2})$$

Next, one introduces a twist in the boundary, lets say in the x-direction, keeping the periodic boundary conditions for the y-direction. Using the canonical transformation,

$$n_i := \hat{R}(\vec{e}, -\frac{\phi}{L} \vec{e}_x) \tilde{n}_i, \text{ where } \tilde{n}_i = (n_i^x, n_i^y, n_i^z)^T \quad (\text{A.3})$$

and  $\hat{R}$  being the rotation operator, the twist may be eliminated from the boundary condition, to appear explicitly in the Hamiltonian. Setting the rotation axis  $\vec{e}$  to the  $\vec{e}_z$ -axis yields:

$$\begin{aligned} \hat{H}_{Tri} &= J_s \sum_i n_i^z n_{i+a_x}^z \\ &+ J_s \sum_i \frac{1}{2} \left( e^{i\phi \frac{a}{L}} n_i^+ n_{i+a_x}^- + e^{-i\phi \frac{a}{L}} n_i^- n_{i+a_x}^+ \right) \\ &+ J_s \sum_{\substack{i,\alpha \\ \alpha \neq x}} \left( n_i^z n_{i+a_\alpha}^z + \frac{1}{2} \left( n_i^- n_{i+a_\alpha}^+ + n_i^+ n_{i+a_\alpha}^- \right) \right), \end{aligned} \quad (\text{A.4})$$

where  $n_i^+$  and  $n_i^-$  are defined in formal equivalence to the  $S = \frac{1}{2}$  ladder operators  $\hat{S}_i^+$  and  $\hat{S}_i^-$ :

$$n_i^+ = n_i^x + i n_i^y, \text{ and } n_i^- = n_i^x - i n_i^y. \quad (\text{A.5})$$

The combination of the upper equations with the SSE formulation of the partition function (see Eq. (1.6)),

$$Z = \sum_{n, \{S_n\}} (\beta J_s)^n \frac{(M-n)!}{M!} \langle \alpha | H_{b_M, r_M}(\phi) \cdots H_{b_1, r_1}(\phi) | \alpha \rangle, \quad (\text{A.6})$$

yields the spin stiffness  $\rho_s$ :

$$\rho_s = \frac{1}{Z} \sum_{n, S_n} (\beta J_s)^n \frac{(M-n)!}{M!} \cdot \langle \alpha | H_{b_M, r_M}(\phi) \cdots H_{b_1, r_1}(\phi) | \alpha \rangle \rho_s(S_n), \quad (\text{A.7})$$

with:

$$\rho_s(S_n) = \frac{-1}{\beta L^{d-2}} \sum_{p,i} \langle \alpha_p | \frac{\partial^2}{\partial \phi^2} \left( e^{i\phi \frac{a}{L}} n_i^+ n_{i+a_x}^- + e^{-i\phi \frac{a}{L}} n_i^- n_{i+a_x}^+ \right) \Big|_{\phi=0} | \alpha_{p-1} \rangle, \quad (\text{A.8})$$

here  $p$  labels the propagation in the loop update, and is  $i$  the site index. After introducing a winding number  $W_x$  such that:

$$\rho_s(S_n) = \frac{1}{\beta L^d} W_x(S_n)^2, \quad (\text{A.9})$$

it is now sufficient to calculate the winding number  $W_x(S_n)$  to detect an AF phase. The definition of the winding number follows by inserting Eq. (A.8) in Eq. (A.9) and reads:

$$W_x(S_n)^2 = \sum_{p,i} L^2 \langle \alpha_p | \frac{\partial^2}{\partial \phi^2} \left( e^{i\phi \frac{a}{L}} n_i^+ n_{i+a_x}^- + e^{-i\phi \frac{a}{L}} n_i^- n_{i+a_x}^+ \right) \Big|_{\phi=0} | \alpha_{p-1} \rangle (\text{A.10})$$

Evaluating expression (A.10) yields:

$$W_x(S_n) = \sum_{p,i} c \cdot \langle \alpha_p | n_i^+ n_{i+a_x}^- - n_i^- n_{i+a_x}^+ | \alpha_{p-1} \rangle \quad (\text{A.11})$$

For simplicity the constant  $c$  unifies all other prefactors. To access  $W_x$  in an actual SSE simulation, one has to rewrite it in terms of  $t_{\alpha,i}$  and  $t_{\alpha,i}^\dagger$  and  $W_x(S_n)$  becomes:

$$\begin{aligned}
W_x(S_n) = \sum_{p,i} c \cdot & \left( \langle \alpha_p | t_{y,i}^\dagger t_{x,i+a_x}^\dagger - t_{x,i}^\dagger t_{y,i+a_x}^\dagger | \alpha_{p-1} \rangle \right. \\
& + \langle \alpha_p | t_{y,i}^\dagger t_{x,i+a_x} - t_{x,i}^\dagger t_{y,i+a_x} | \alpha_{p-1} \rangle \\
& + \langle \alpha_p | t_{y,i} t_{x,i+a_x}^\dagger - t_{x,i} t_{y,i+a_x}^\dagger | \alpha_{p-1} \rangle \\
& \left. + \langle \alpha_p | t_{y,i} t_{x,i+a_x} - t_{x,i} t_{y,i+a_x} | \alpha_{p-1} \rangle \right)
\end{aligned} \tag{A.12}$$

Apparently this is different from what one usually refers to as a ‘winding number’ in the context of world-line based update schemes. In the latter case the winding number describes the expectation value of a twist in the world line, that are extremely easy to access numerically. For example, if the spin interaction in some Hamiltonian is described by a Heisenberg term  $J \sum_{\langle i,j \rangle} \hat{S}_i \hat{S}_j$ , one can replace the operators  $n_i^+$  and  $n_i^-$  in Eq. (A.11) by their Heisenberg counterparts  $\hat{S}_i^+$  and  $\hat{S}_i^-$ , and the winding number reads:

$$W_x^{Heis}(S_n) = \sum_{p,i} c \cdot \langle \alpha_p | \hat{S}_i^+ \hat{S}_{i+a_x}^- - \hat{S}_i^- \hat{S}_{i+a_x}^+ | \alpha_{p-1} \rangle. \tag{A.13}$$

The operators on the right hand side of Eq. A.13 are parts of the Heisenberg Hamiltonian, i.e., they are contained in the operator-loop update, represented by vertices. Therefore, in models containing Heisenberg spin interactions, the spin stiffness can very easily be measured by simply counting the winding numbers.

Unfortunately during a simulation of the Hamiltonian Eq. (5.2), the spinstiffness cannot be calculated from the twist of the worldlines, because the Hamiltonian does not contain interaction terms between different spin projections, i.e, no terms  $t_{\alpha,i} t_{\alpha',i+a_x}^\dagger$ , for  $\alpha \neq \alpha'$ . As a consequence, measuring a twist in the worldline of some triplet is not equivalent to measuring the winding number given by Eq. (A.12) (like it would be for the Heisenberg case). In addition, measuring off-diagonal correlation functions, of operator sequences that are not contained in the Hamiltonian poses (to our knowledge) an unsolved problem in the framework of the SSE operator loop update scheme. However, as explained in Sec. 1.3.2, these kind of correlation functions can be accessed in an extra measuring step after the construction of the loop.

In order to make sure, that the above argumentation explains the difference between the results of Chen’s and our calculations, also the expectation value of the twists ( $\langle TW \rangle$ ) in the triplet-world lines have been recorded and evaluated ‘naively’ using Eq. (A.9), i.e., setting  $W_x = \langle TW \rangle_x$ . This procedure indeed reproduces the results of Ref. [30], and therefore one can be sure, that the incompatibility of their and our results is due to an invalid way of determining the spin stiffness in Ref. [30].



# Bibliography

---

- [1] H. K. Onnes, *Akad. van Wetenschappen* **14**, 818 (1911).
- [2] A. L. Fetter and J. D. Walecka, *Quantum Theory of Many-Particle Systems* (Mc Graw-Hill, New York, 1971).
- [3] J. Bardeen, L. N. Cooper, and J. R. Schrieffer, *Phys. Rev. B* **108**, 1175 (1957).
- [4] J. G. Bednorz and K. A. Müller, *Zeit. Phys. B* **64**, 189 (1986).
- [5] P. Dai, B. Chakoumakos, G. Sun, K. Wong, y. Xin, and D. Lu, *Physca C* **243**, 201 (1995).
- [6] A. Damascelli, Z.-X. Shen, and Z. Hussain, *Rev. Mod. Phys.* **75**, 473 (2002).
- [7] C. Tsuei and J. Kirtley, in *The Physics of Superconductors*, edited by K. Bennemann and J. Ketterson (Springer, Berlin, Heidelberg, New York, 2002), Vol. 1, Chap. 9, pp. 648–723.
- [8] T. P. Devereaux, T. Cuk, Z.-X. Shen, and N. Nagaosa, *Phys. Rev. Lett.* **93**, 117004 (2004).
- [9] T. Cuk, F. Baumberger, D. H. Lu, N. Ingle, X. J. Zhou, H. Eisaki, N. Kaneko, Z. Hussain, T. P. Devereaux, N. Nagaosa, and Z.-X. Shen, *Phys. Rev. Lett.* **93**, 117003 (2004).
- [10] G. Dopf, J. Wagner, P. Dieterich, A. Muramatsu, and W. Hanke, *Phys. Rev. Lett.* **68**, 2082 (1992).
- [11] R. Preuss, A. Muramatsu, W. von der Linden, F. F. Assaad, and W. Hanke, *Phys. Rev. Lett.* **73**, 732 (1994).

- [12] R. Preuss, W. Hanke, and W. von der Linden, *Phys. Rev. Lett.* **75**, 1344 (1995).
- [13] R. Preuss, W. Hanke, C. Gröber, and H. G. Evertz, *Phys. Rev. Lett.* **79**, 1122 (1997).
- [14] C. Gröber, R. Eder, and W. Hanke, *Phys. Rev. B* **62**, 4336 (2000).
- [15] P. W. Anderson, *Science* **235**, 1196 (1987).
- [16] P. W. Anderson, P. A. Lee, M. Randeria, T. M. Rice, N. Trivedi, and F. C. Zhang, *J Phys. Condens. Matter* **16**, R755 (2004).
- [17] S.-C. Zhang, *Science* **275**, 1089 (1997).
- [18] E. Demler, W. Hanke, and S.-C. Zhang, *Rev. Mod. Phys.* **76**, 909 (2004).
- [19] M. Jöstingmeier, A. Dorneich, E. Arrigoni, W. Hanke, and S.-C. Zhang, *Phys. Rev. B* **68**, 245111 (2003).
- [20] A. Dorneich, W. Hanke, E. Arrigoni, M. Troyer, and S. C. Zhang, *Phys. Rev. Lett.* **88**, 057003 (2002).
- [21] A. Dorneich, M. Jöstingmeier, E. Arrigoni, W. Hanke, and M. Troyer, in *NIC Symposium 2004 - Proceedings*, Vol. 20 of *NIC Series*, edited by D. Wolf, G. Münster, and M. Kremer (NIC-Directors, Jülich, 2004).
- [22] A. Dorneich, M. Jöstingmeier, E. Arrigoni, C. Dahnken, T. Eckl, W. Hanke, S. C. Zhang, and M. Troyer, in *Proceedings of the First Joint HLRB and KONWIHR Result and Reviewing Workshop, Garching, Oct. 2002*, edited by S. Wagner, W. Hanke, A. Bode, and F. Durst (Springer, Berlin, Heidelberg, New York, 2003).
- [23] E. Altman and A. Auerbach, *Phys. Rev. B* **65**, 104508 (2002).
- [24] M. Jöstingmeier, A. Dorneich, E. Arrigoni, W. Hanke, and S.-C. Zhang, in *High Performance Computing in Science and Engineering, Munich 2004*, edited by E. Krause and W. Jäger (Springer Verlag, Berlin, 2004), p. to appear.
- [25] K. McElroy, D.-H. Lee, J. E. Hoffman, K. M. Lang, J. Lee, E. W. Hudson, H. Eisaki, and S. U. J. Davis, cond-mat/0406491 (unpublished).
- [26] T. Hanaguri, C. Lupien, D.-H. Lee, M. Azuma, M. Takano, H. Takagi, and J. Davis, *Nature* **430**, 1001 (2004).
- [27] M. Vershinin, S. Misra, S. Ono, Y. Abe, Y. Ando, and A. Yazdani, *Science* **303**, 1995 (2004).

- 
- [28] C. Howald, H. Eisaki, N. Kaneko, M. Greven, and A. Kapitulnik, *Phys. Rev. B* **67**, 014533 (2003).
- [29] J. E. Hoffman, E. W. Hudson, K. M. Lang, V. Madhavan, H. Eisaki, S. Uchida, and J. C. Davis, *Science* **295**, 466 (2002).
- [30] H.-D. Chen, S. Capponi, F. Alet, and S.-C. Zhang, *Phys. Rev. B* **70**, 024516 (2004).
- [31] R. Eder, A. Dorneich, M. G. Zacher, W. Hanke, and S.-C. Zhang, *Phys. Rev. B* **59**, 561 (1999).
- [32] M. Jöstingmeier, W. Hanke, S. Capponi, and S. Zhang, cond-mat/0412??? (unpublished).
- [33] S. Komiyama, H.-D. Chen, S.-C. Zhang, and Y. Ando, cond-mat/0408483 (unpublished).
- [34] D. P. Landau, *Phys. Rev. B* **17**, 4164 (1977).
- [35] G. Schmid, S. Todo, M. Troyer, and A. Dorneich, *Phys. Rev. Lett.* **88**, 167208 (2002).
- [36] E. Kim and H. W. Chan, *Nature* **427**, 225 (2004).
- [37] E. Kim and H. W. Chan, *Science* **305**, 1941 (2004).
- [38] T. Maier, M. Jarrell, T. Pruschke, and M. Hettler, cond-mat/0404055 (unpublished).
- [39] M. Suzuki, *Prog. Theor. Phys.* **65**, 1454 (1976).
- [40] J. E. Hirsch, R. L. Sugar, D. J. Scalapino, and R. Blankenbecler, *Phys. Rev. B* **26**, 5033 (1982).
- [41] H. G. Evertz, G. Lana, and M. Marcu, *Phys. Rev. Lett.* **70**, 875 (1993).
- [42] H. Evertz and M. Marcu, in *Lattice 92*, edited by M. Suzuki (World Scientific, Singapore, 1994), p. 65.
- [43] H. Evertz and M. Marcu, *Nucl. Phys. B. (Proc Suppl.)* **30**, 277 (1993).
- [44] U. Wiese and H.-P. Ying, *Phys. Rev. Lett. A* **168**, 143 (1992).
- [45] U. Wiese and H.-P. Ying, *Z. Phys. B* **93**, 147 (1994).
- [46] N. Kawashima, J. Gubernatis, and H. Evertz, *Phys. Rev. B* **50**, 136 (1994).

- 
- [47] N. Kawashima and J. Gubernatis, *Phys. Rev. Lett.* **73**, 1295 (1994).
- [48] N. Kawashima, *J. Stat. Phys.* **82**, 131 (1996).
- [49] N. Kawashima and J. Gubernatis, *J. Stat. Phys.* **80**, 169 (1995).
- [50] H. Evertz, in *Numerical Methods for Lattice Quantum Many Body Problems, Frontiers in Physics*, edited by D. Scalapino (Edison Wesley, New York, 1998).
- [51] M. Kohno and M. Takahashi, *Phys. Rev. B* **56**, 3212 (1997).
- [52] A. W. Sandvik, *Phys. Rev. B* **59**, R14157 (1999).
- [53] A. W. Sandvik, *Phys. Rev. B* **56**, 11678 (1997).
- [54] F. F. Assaad, W. Hanke, and D. J. Scalapino, *Phys. Rev. B* **50**, 12835 (1994).
- [55] M. Takasu, S. Miyashita, and m. Suzuki, *Prog. Theor. Phys.* **75**, 1254 (1986).
- [56] A. Dorneich, New computational techniques for strongly correlated electron systems, PhD Thesis, Universität Würzburg, 2001.
- [57] O. F. Syljusen and A. W. Sandvik, *Physical Review E (Statistical, Nonlinear, and Soft Matter Physics)* **66**, 046701 (2002).
- [58] A. W. Sandvik, R. R. P. Singh, and D. K. Campbell, *Phys. Rev. B* **56**, 14510 (1997).
- [59] A. W. Sandvik, *J. Phys. A* **25**, 3667 (1992).
- [60] W. von der Linden, *Appl. Phys. A* **60**, 155 (1995).
- [61] W. von der Linden, R. Preuß, and W. Hanke, *J. Phys. Condens. Matter* **8**, 3881 (1996).
- [62] K. S. D. Beach, cond-mat/0403055 (unpublished).
- [63] A. Dorneich and M. Troyer, *Phys. Rev. E* **64**, 066701 (2001).
- [64] J. Hubbard, *Proc. R. Soc. London* **276**, 238 (1963).
- [65] C. Gröber, R. Eder, and W. Hanke, *Phys. Rev. B* **62**, 4336 (2000).
- [66] M. Imada, A. Fujimori, and Y. Tokura, *Rev. Mod. Phys.* **70**, 1039 (1998).
- [67] C. J. Morningstar and M. Weinstein, *Phys. Rev. Lett.* **73**, 1873 (1994).
- [68] C. Morningstar and M. Weinstein, *Phys. Rev. D* **54**, 4131 (1996).

- [69] K. G. Wilson, *Rev. Mod. Phys.* **47**, 773 (1975).
- [70] L. P. Kadanoff, in *Phase Transitions and Critical Phenomena*, edited by C. Domb and M. Green (Academic, London, 1974), Vol. 5a, Chap. 1, pp. 1–33.
- [71] J. Cardy, in *Scaling and Renormalization in Statistical Physics* (Cambridge University Press, U.K., 1996), Chap. 8.
- [72] H. A. Bethe, *Z. Phys.* **71**, 205 (1931).
- [73] S. Sachdev and R. N. Bhatt, *Phys. Rev. B* **41**, 9323 (1990).
- [74] S. Gopalan, T. M. Rice, and M. Sigrist, *Phys. Rev. B* **49**, 8901 (1994).
- [75] J. E. Hirsch, S. Tang, E. Loh, and D. J. Scalapino, *Phys. Rev. Lett.* **60**, 1668 (1988).
- [76] J. A. Riera and A. P. Young, *Phys. Rev. B* **39**, 9697 (1989).
- [77] R. M. Fye, M. J. Martins, and R. T. Scalettar, *Phys. Rev. B* **42**, 6809 (1990).
- [78] E. Dagotto, A. Moreo, F. Ortolani, D. Poilblanc, and J. Riera, *Phys. Rev. B.* **45**, 10741 (1992).
- [79] E. Dagotto, *Rev. Mod. Phys.* **66**, 763 (1994).
- [80] R. Eder, W. Hanke, and S.-C. Zhang, *Phys. Rev. B* **57**, 13781 (1998).
- [81] E. Demler and S.-C. Zhang, *Phys. Rev. Lett.* **75**, 4126 (1995).
- [82] S. Meixner, W. Hanke, E. Demler, and S.-C. Zhang, *Phys. Rev. Lett.* **79**, 4902 (1997).
- [83] H. F. Fong, B. Keimer, P. W. Anderson, D. Reznik, F. Dogan, and I. A. Aksay, *Phys. Rev. Lett.* **75**, 316 (1995).
- [84] H. A. Mook, M. Yethiraj, G. Aeppli, T. E. Mason, and T. Armstrong, *Phys. Rev. Lett.* **70**, 3490 (1993).
- [85] P. Dai, M. Yethiraj, H. A. Mook, T. B. Lindemer, and F. Dogan, *Phys. Rev. Lett.* **77**, 5425 (1996).
- [86] P. Dai, H. A. Mook, and F. Dogan, *Phys. Rev. Lett.* **80**, 1738 (1998).
- [87] P. Bourges, Y. Sidis, H. F. Fong, L. P. Regnault, J. Bossy, A. Ivanov, and B. Keimer, *Science* **288**, 1234 (2000).

- 
- [88] H. A. Mook, P. Dai, S. M. Hayden, G. Aeppli, T. G. Perring, and F. Dogan, *Nature* (London) **395**, 580 (1998).
- [89] C. Stock, W. J. L. Buyers, R. Liang, D. Peets, Z. Tun, D. Bonn, W. N. Hardy, and R. J. Birgeneau, *Phys. Rev. B* **69**, 014502 (2004).
- [90] H. F. Fong, P. Bourges, Y. Sidis, L. P. Regnault, J. Bossy, A. Ivanov, D. L. Milius, I. A. Aksay, and B. Keimer, *Phys. Rev. Lett.* **82**, 1939 (1999).
- [91] H. He, P. Bourges, Y. Sidis, C. Ulrich, L. P. Regnault, S. Pailhes, N. S. Berzigiarova, N. N. Kolesnikov, and B. Keimer, *Science* **295**, 1045 (2002).
- [92] H. He, Y. Sidis, P. Bourges, G. D. Gu, A. Ivanov, N. Koshizuka, B. Liang, C. T. Lin, L. P. Regnault, E. Schoenherr, and B. Keimer, *Phys. Rev. Lett.* **86**, 1610 (2001).
- [93] Y. Bazaliy, E. Demler, and S.-C. Zhang, *Phys. Rev. Lett.* **79**, 1921 (1997).
- [94] D. P. Arovas, A. J. Berlinsky, C. Kallin, and S.-C. Zhang, *Phys. Rev. Lett.* **79**, 2871 (1997).
- [95] E. Demler, A. J. Berlinsky, C. Kallin, G. B. Arnold, and M. R. Beasley, *Phys. Rev. Lett.* **80**, 2917 (1998).
- [96] D. E. Sheehy and P. M. Goldbart, *Phys. Rev. B* **57**, 8131 (1998).
- [97] M. Greiter, *Phys. Rev. Lett.* **79**, 4898 (1997).
- [98] G. Baskaran and P. W. Anderson, *J. Phys. and Chem. Solids* **59**, 1780 (1998).
- [99] S.-C. Zhang, *Journal of Physics and Chemistry of Solids* **59**, 1774 (1998).
- [100] S.-C. Zhang, J.-P. Hu, E. Arrigoni, W. Hanke, and A. Auerbach, *Phys. Rev. B* **60**, 13070 (1999).
- [101] X. Hu, *Phys. Rev. Lett.* **87**, 057004 (2001).
- [102] J. M. Kosterlitz, D. R. Nelson, and M. E. Fisher, *Phys. Rev. B* **13**, 412 (1976).
- [103] E. Arrigoni and W. Hanke, *Phys. Rev. B* **62**, 11770 (2000).
- [104] X. Hu, *Phys. Rev. Lett.* **87**, 057004 (2001).
- [105] M. E. Fisher, M. N. Barber, and D. Jasnow, *Phys. Rev. A* **8**, 1111 (1973).
- [106] A. Aharony, *Phys. Rev. Lett.* **88**, 059703 (2002).

- [107] P. Calabrese, A. Pelissetto, and E. Vicari, cond-mat/0203533 (unpublished).
- [108] P. Calabrese, A. Pelissetto, and E. Vicari, Phys. Rev. B **67**, 054505 (2002).
- [109] A. Pelissetto and E. Vicari, Phys. Rep. **368**, 549 (2000).
- [110] W. Kohn and J. M. Luttinger, Phys. Rev. Lett. **15**, 524 (1965).
- [111] B. I. Halperin, T. C. Lubensky, and S.-K. Ma, Phys. Rev. Lett. **32**, 292 (1974).
- [112] K. Yamada, C. H. Lee, K. Kurahashi, J. Wada, S. Wakimoto, S. Ueki, H. Kimura, Y. Endoh, S. Hosoya, G. Shirane, R. J. Birgeneau, M. Greven, M. A. Kastner, and Y. J. Kim, Phys. Rev. B **57**, 6165 (1998).
- [113] S. Wakimoto, R. J. Birgeneau, M. A. Kastner, Y. S. Lee, R. Erwin, P. M. Gehring, S. H. Lee, M. Fujita, K. Yamada, Y. Endoh, K. Hirota, and G. Shirane, Phys. Rev. B **61**, 3699 (2000).
- [114] S. Wakimoto, R. J. Birgeneau, Y. S. Lee, and G. Shirane, Phys. Rev. B **63**, 172501 (2001).
- [115] J. Zaanen and O. Gunnarsson, Phys. Rev. B **40**, 7391 (1989).
- [116] V. J. Emery and S. A. Kivelson, Nature (London) **374**, 434 (1995).
- [117] M. R. Norman and H. Ding, Phys. Rev. B **57**, R11089 (1998), cond-mat/9712116.
- [118] Y. Wang, Z. A. Xu, T. Kakeshita, S. Uchida, S. Ono, Y. Ando, and N. P. Ong, Phys. Rev. B **64**, 224519 (2001).
- [119] Y. Wang, N. P. Ong, Z. A. Xu, T. Kakeshita, S. Uchida, D. A. Bonn, R. Liang, , and W. N. Hardy, Phys. Rev. Lett. **88**, 257003 (2002).
- [120] J. Corson, R. Mallozzi, J. Orenstein, J. N. Eckstein, and I. Bozovic, Nature (London) **398**, 221 (1999).
- [121] A. P. Kampf and J. R. Schrieffer, Phys. Rev. B **42**, 7967 (1990).
- [122] V. J. Emery, S. A. Kivelson, and O. Zachar, Phys. Rev. B **56**, 6120 (1997).
- [123] V. Barzykin and D. Pines, Phys. Rev. B **52**, 13585 (1995).
- [124] H.-D. Chen, J.-P. Hu, S. Capponi, E. Arrigoni, and S.-C. Zhang, Phys. Rev. Lett. **89**, 137004 (2002).

- 
- [125] H.-D. Chen, O. Vafek, A. Yazdani, and S.-C. Zhang, *Phys. Rev. Lett.* **93**, 187002 (2004).
- [126] N. D. Mermin and H. Wagner, *Phys. Rev. Lett.* **17**, 1133 (1966).
- [127] P. C. Hohenberg, *Phys. Rev.* **158**, 383 (1967).
- [128] D. Pines and P. Nozières, *The Theory of Quantum Liquids* (Benjamin, New York, 1966), Vol. I.
- [129] J. Kosterlitz and D. Thouless, *J. Phys. C: Solid State Phys.* **6**, 1181 (1973).
- [130] V. L. Berezinskii, *Zh. Éksp. Teor. Fiz.* **59**, 907 (1970), (*Sov. Phys. JETP*, **32**, 493 (1971)).
- [131] E. L. Pollock and D. M. Ceperly, *Phys. Rev. B* **36**, 8343 (1987).
- [132] P. Sengupta, L. P. Pryadko, F. Alet, M. Troyer, and G. Schmid, cond-mat/0412338 (unpublished).
- [133] G. V. Chester, *Phys. Rev. A* **2**, 256 (1970).



# Zusammenfassung

---

Diese Arbeit läßt sich in zwei grobe Abschnitte gliedern. Der erste Teil umfaßt die Kapitel 1– 3, in denen drei verschiedene Konzepte beschrieben werden, die zum Verständnis stark korrelierter Vielteilchen-Systeme dienen. Dies sind zunächst einmal die  $SO(5)$ -Theorie in Kapitel 3, die den allgemeinen Rahmen vorgibt und auf der numerischen Seite die SSE (*Stochastic-Series Expansion*) in Kapitel 1 und der Contractor Renormierungsgruppen Ansatz (Contractor-Renormalization Group approach, s. Kapitel 2). Die zentrale Idee dieser Dissertationsschrift besteht darin, diese verschiedenen Konzepte zu kombinieren, um ein besseres Verständnis der Hochtemperatursupraleiter zu erhalten. Im zweiten Teil dieser Arbeit (Kap. 4 und Kap. 5) werden die so gewonnenen Ergebnisse dargestellt.

Nach einer kurzen Einführung, wurde in Kapitel 1 die den numerischen Untersuchungen in Kap 4 und Kap. 5 zugrunde liegende Stochastische Reihen Entwicklung (SSE) vorgestellt. Die SSE gehört zu den Quanten Monte-Carlo Verfahren. Im Vergleich zu Algorithmen, die auf einer Diskretisierung der imaginären Zeit beruhen hat die SSE den fundamentalen Vorteil, daß sie keinen systematischen Fehler trägt. Eine zentrale Position in der Beschreibung des Algorithmus nimmt der sogenannte “Operator Schleifenaktualisierungs-Mechanismus” (engl. Operator Loop Update Mechanism) ein. Dieses Verfahren wurde, aufbauend auf den Konzepten von Dorneich und Troyer [63] im Rahmen dieser Arbeit deutlich verbessert [22, 21]. Durch diese Optimierung, die insbesondere den Bereich der Messung von Greenschen Einteilchenfunktionen betrifft, gelang es die Größe der behandelbaren Systeme um eine Größenordnung zu erhöhen (von ca. 5000 Plätzen bei  $T = 1J_c$  auf ca. 10000 Plätze bei  $T = 0.5J_c$ ). Diese Erhöhung stellte eine notwendige Bedingung dar, um die in Kapitel 4 und Kapitel 5 dargestellten Ergebnisse erhalten zu können. Insbesondere ist sie für die Untersuchung des Skalenverhaltens am kritischen Punkt im Phasendiagramm von Bedeutung

Darüber hinaus wurden substanzielle Verbesserungen des Algorithmus hinsichtlich der Meßbarkeit von nicht diagonalen Zweiteilchen-Greenfunktionen, als auch von Einteilchen-Greenfunktionen die nicht im Hamiltonoperator enthalten, sind entwickelt.

Wurde in Kapitel 1 ein numerisches Verfahren vorgestellt und weiterentwickelt, so ist der Ansatz des in Kapitel 2 beschriebenen Verfahrens ein anderer. Mit Hilfe der dort vorgestellten iterativen Contractor Renormierungsgruppen Technik kann die Physik eines Ausgangsmodells auf ein effektives Niedrigenergiemodell abgebildet werden, welches die effektiven niedrig-energetischen Anregungen des Ausgangsmodells in Form von Quasi-Teilchen (Bosonen, Fermionen) beschreibt. Die Anwendung des Verfahrens auf das *Hubbard-Modell* liefert nach einer Iteration ein Modell, welches die Physik des *Hubbard-Modells* auf wechselwirkende Loch-Paare und Triplet-Anregungen reduziert [23]. Die Diskussion dieser Zustände in Abschnitt 2.1 zeigte, daß sie geeignet sind, um Antiferromagnetismus und Supraleitung, zwei zentrale Komponenten für die Physik der Hochtemperatur-Supraleiter zu beschreiben.

Das letzte Kapitel des ersten Teils dieser Arbeit (Kap. 3) widmet sich einem eleganteren, zunächst mathematisch postulierten [17] Ansatz, um die Physik der Hochtemperatur-Supraleiter zu erfassen: Das Symmetrieprinzip. Die  $SO(5)$ -Theorie der Hochtemperatur Supraleitung [18] führt einen fünf-dimensionalen Ordnungsparameter ein, der die auf den "ersten Blick" sehr verschieden erscheinenden Ordnungsparameter für Antiferromagnetismus (3 komponentiger Ordnungsparameter) und Supraleitung (2 komponentiger Ordnungsparameter) vereint. Die Generatoren der  $SO(5)$ -Gruppe verbinden dann antiferromagnetische und supraleitende Zustände, durch entsprechenden Rotationen. Die  $SO(5)$ -Theorie macht eine Reihe von experimentell überprüfbar Aussagen, neben dem globalen Phasendiagramm z.B. die Neutronen-Resonanz-Mode [18]. Allerdings hat die exakte  $SO(5)$ -Theorie der ursprünglichen Zhang Arbeit [17] auch einen gravierenden Nachteil. Exakt  $SO(5)$ -symmetrische Modelle können die Mott-Physik der Hochtemperatur-Supraleiter in der Nähe von Halbfüllung nicht wiedergeben, da Zustände, die gepaarte Elektronen beschreiben und Zustände die Lochpaar-Anregungen beschreiben in einer exakten  $SO(5)$  Lie-Algebra und Theorie energetisch entartet sind. Projiziert man aber die Elektronen-Paare durch eine Gutzwiller-Projektion aus dem Modell [100], so wird die  $SO(5)$ -Symmetrie auf dem Niveau des Hamilton-Operators zu Gunsten einer korrekten Beschreibung der Mott-Physik explizit gebrochen. Diese Symmetriebrechung auf der Ebene des Hamilton-Operators ( $\hat{H}$ ) ist jedoch eigentlich zu erwarten, da  $\hat{H}$  noch nicht das Skalenverhalten, d.h. das niedrig energetische Verhalten ( $E \approx k_B T_c$ ) selbst zeigt, sondern es nur implizit beinhaltet. Dazu muß das Skalenverhalten eines multi-kritischen Punktes studiert werden. Die alles entscheidende Frage ist, ob in der Nähe eines solchen Punktes die  $SO(5)$ -Symmetrie auftritt – oder wie man sagt – asymptotisch restauriert wird. Selbst in der ursprünglichen exakten  $SO(5)$ -Theorie [17] ist

die  $SO(5)$ -Symmetrie durch das chemische Potential, welches die Dotierung beschreibt gebrochen. Zhang, Hu, Arrigoni, Hanke und Auerbach haben ein entsprechendes Modell mit gebrochener  $SO(5)$ -Symmetrie konstruiert [100]. Erstaunlicherweise stimmt dieses projizierte *sof*-Modell mit dem durch CORE Rechnungen (s. Kapitel 2) motivierten effektiven Modell im stark-korrelierten Parameterbereich im wesentlichen überein.

Im zweiten Teil dieser Arbeit wird nun das in den Kapiteln 2 und 3 motivierte verallgemeinerte  $SO(5)$ -Modell mit den in Kapitel 1 vorgestellten und entwickelten numerischen Möglichkeiten untersucht.

Dazu wird zunächst das Phasendiagramm als Funktion der Temperatur und der Dotierung (chem. Potential) für das projizierte  $SO(5)$ -Modell berechnet. Das berechnete Phasendiagramm enthält zentrale Elemente der experimentell beobachteten Phasendiagramme der Hochtemperatur-Supraleiter, d.h. einen antiferromagnetischen Isolator für kleine Dotierungen und eine supraleitende Phase für größere Dotierungen. Durch eine geeignete Wahl der Modellparameter ( $J_c/(2J_s) = 0.225$ ) konnte sogar das korrekte Verhältniss von supraleitender Sprungtemperatur zur Néel-Temperatur wiedergegeben werden. Das Phasendiagramm zeigt einen multikritischen Punkt, in dessen Nähe die  $SO(5)$ -Symmetrie in der Tat wieder hergestellt wird, obgleich diese auf dem Niveau des Hamilton-Operators explizit gebrochen ist [19, 24]. Nach unserem besten Wissen war es das erste Mal, daß Phasenübergänge in einem Quantenmodell mittels numerischen Simulationen so exakt bestimmt werden konnten, daß die Berechnung der kritischen Exponenten mit hinreichender Genauigkeit möglich wurde. Dies ist vor allem ein Verdienst der in Kapitel 1 geleisteten Optimierung des Algorithmus.

Das Phasendiagramm der Hochtemperatur-Supraleiter zeigt aber neben AF und SL z.B. auch ladungsgeordnete Phasen [25, 26, 27, 28, 29], die mit dem projizierten  $SO(5)$ -Modell nicht beschrieben werden können. Ermutigt durch die in Kapitel 4 dargestellten Ergebnisse, wurde das projizierte  $SO(5)$ -Modell erweitert, indem längerreichweitige Wechselwirkungen zwischen den Loch-Paar Bosonen hinzugefügt wurden [30], um somit auch die ladungsgeordneten Phasen zu erfassen. Diese Wechselwirkungen sind durch CORE Analysen [30], als auch durch allgemeinere  $SO(5)$  Ansätze [18, 31] begründet.

Dieses erweiterte Modell wurde dann in Kapitel 5 eingehend untersucht. Dabei wurde zunächst das Grundzustandsphasendiagramm berechnet und mit den SSE-Daten der früheren Referenz [30] verglichen. Dabei fiel auf, daß die in Referenz [30] berichteten Ergebnisse bis auf antiferromagnetische Phase reproduziert werden konnten. Der Grund für diese Abweichung konnte in der inkonsistenten Bestimmung der SpinstEIFheit in Referenz [30] lokalisiert werden (siehe Anhang A). Da das erweiterte projizierte  $SO(5)$ -Modell (*ep* $SO(5)$ -Modell) für die zunächst in Ref. [30] gewählten Parameter keinen Antiferromagnetismus zeigt, wurde ausgehend von analytischen Überlegungen das chemische

Potential für die Triplett-Anregungen variiert, und gezeigt daß dann das Modell – wie erwartet – die antiferromagnetische Phase reproduziert. Das Grundzustandsphasendiagramm enthält also Antiferromagnetismus, Supraleitung und als phaszinierenden neuen Befund ladungsgeordnete Phasen. Die in den Simulationen nachgewiesene Ladungsordnung in sogenannten Schachbrettmustern, liefert eine natürliche Erklärung für die mittels der Rastertunnelmikroskopie in  $\text{Bi}_2\text{Sr}_2\text{CaCu}_2\text{O}_{8+\delta}$  und  $\text{Ca}_{2-x}\text{Na}_x\text{CuO}_2\text{Cl}_2$  experimentell beobachtete Ladungsordnung [25, 26, 27, 28, 29]. Motiviert durch Experimente von Komyia et al. [33], die für bestimmte sogenannte kommensurable Dotierungen (‘magic doping fractions’) eine verringerte Ladungsträgermobilität berichten, wurde auch die Dotierungsabhängigkeit des “Schachbrettordnungsparameters” bestimmt. Das  $\text{epSO}(5)$ -Modell zeigt ladungsgeordnete Schachbrettmusterphasen (‘Checkboard-Phases’) für eben diese sogenannten kommensurablen Dotierungen  $\delta_c = 1/8, 1/4, 3/8$  und  $1/16$ . Im Rahmen eines einfachen physikalischen Bildes wurde insbesondere ein Zusammenhang zwischen der experimentell beobachteten verringerten Ladungsträgermobilität und der Ladungsordnung im  $\text{epSO}(5)$ -Modell hergestellt, der die verringerte Ladungsträgermobilität erklärt. Dabei wurde auch das Wechselspiel von Ladungsordnung und Supraleitung eingehend untersucht, d.h. zunächst wurde der Phasenübergang als Typ zweiter oder höherer Ordnung charakterisiert. Die Temperaturabhängigkeiten der Ordnungsparameter wurden mittels kanonischer Messungen untersucht. Es zeigte sich ein überraschendes ‘Wiedereintritts-Phänomen’ (‘Reentrance Behavior’), d.h. bei Temperatur  $T=0$  ist das System supraleitend, wird dann mit Erhöhung der der Temperatur ladungsgeordnet, um bei erneuter Temperaturerhöhung wieder supraleitend zu werden.

Im letzten Abschnitt des Kapitels 5 wird gezeigt, daß der effektive  $\text{epSO}(5)$ -Hamiltonoperator als allgemeineres effektives Vielteilchenmodell betrachtet werden kann und zum Beispiel geeignet ist,  $^4\text{He}$ -Atome in einem Gitter zu beschreiben. Im Rahmen einer solchen Interpretation des  $\text{epSO}(5)$ -Modells wurde eine supersolide Phase nachgewiesen, d.h. eine Phase in der Suprafluidität und kristalline Ordnung coexistieren. Solch ein Verhalten wurde möglicherweise kürzlich für  $^4\text{He}$ -Atome experimentell beobachtet [36, 37].

Die zentrale Idee dieser Arbeit, d.h. die Kombination der  $\text{SO}(5)$ -Theorie mit den Fähigkeiten bosonischer Quanten-Monte-Carlo Verfahren und den Überlegungen der Renormierungsgruppe, hat sich sich am Beispiel der Physik der Hochtemperatur-Supraleiter als sehr tragfähig erwiesen. Wie schon in den vorhergehenden Abschnitten zusammengefaßt, reproduzieren die numerischen Simulationen der beiden behandelten Modelle eine Reihe wichtiger experimenteller Daten. Die Grundlage für eine künftige weitere schrittweise Erweiterung des Modells wurde so geschaffen. Eine offene Frage ist z.B. die Restaurierung der  $\text{SO}(5)$ -Symmetrie an einem multi-kritischen Punkt, wenn die

längerreichweitigen Wechselwirkungen mit in das Modell einbezogen sind.

Abschliessend muss darauf hingewiesen werden, daß die rein bosonische Natur der Modelle eine vorgegebene Randbedingung darstellt, welche die Konstruktion und die Tragfähigkeit der Modelle als mikroskopische Ansätze zur Lösung des Hoch- $T_c$  Problems möglicherweise einschränkt. Nur aufgrund der rein bosonischen Natur der Quasiteilchen, die in den Modellen wechselwirken, waren die numerischen Studien in der dargestellten Form (bis zu 10000 Gitterplätze bei  $T \approx 0.5J_c$ ) und Präzision möglich. Dennoch vertritt der Autor die Auffassung das dieser Ansatz phenomenologisch gerechtfertigt war. Diese Auffassung beruht zum einen darauf, daß im Rahmen dieser Arbeit wesentliche experimentelle Beobachtungen an den Hochtemperatur-Supraleitern reproduziert werden konnten (s.o.). Zum Anderen muß ganz klar festgestellt werden, daß derzeit keine numerischen Verfahren bekannt sind, die die gleichzeitige Einbeziehung fermionischer Physik ermöglichen (bei ähnlichen Systemgrößen und Temperaturen). Dennoch bleibt zu hoffen, daß durch verbesserte Algorithmen und Rechnersysteme künftig auch gekoppelte fermionisch-bosonische Modellsysteme ähnlich effizient behandelt werden können, wie es heute schon für bosonische Modelle möglich ist.



## Publikationen

1. Object-oriented C++ class library for many body physics on finite lattices and a first application to high-temperature superconductivity  
Ansgar Dorneich, Martin Jöstingmeier, Enrico Arrigoni, Christopher Dahnken, Thomas Eckl, Werner Hanke, Shou-Cheng Zhang and Matthias Troyer  
*in Proceedings of the First Joint HLRB and KONWIHR Result and Reviewing Workshop, Garching, Oct. 2002*, pp. 307,  
Editors: S. Wagner, W. Hanke, A. Bode and F.Durst  
Springer, Berlin Heidelberg New York (2003)
2. Scaling properties of the projected SO(5) model in three dimensions  
M. Jöstingmeier, A. Dorneich, E. Arrigoni, W. Hanke and Shou-Cheng Zhang  
*Phys. Rev. B* **68**, 245111 (2003)
3. Accessing the Dynamics of Strongly-Correlated Many Body Systems within the Operator Loop Update and its Application to High-Temperature Superconductivity  
Ansgar Dorneich, Martin Jöstingmeier, Enrico Arrigoni, Werner Hanke and Matthias Troyer  
*in Proceedings of the NIC Symposium 17.-18. Feb 2004*, pp. 227,  
Editors: D. Wolf, G. Münster, M. Kremer  
NIC Series Vol. 20, ISBN 3-00-012372-5
4. Phasediagram and scaling properties of the projected SO(5) model in three dimensions,  
M. Jöstingmeier, A. Dorneich, E. Arrigoni, W. Hanke and Shou-Cheng Zhang  
*in Proceedings of the Second Joint HLRB and KONWIHR Result and Reviewing Workshop, Garching, March. 2004*, pp. 289,  
Editors: S. Wagner, W. Hanke, A. Bode and F.Durst  
Springer, Berlin Heidelberg New York (2004)
5. Quantum-Monte Carlo analysis of the extended projected-SO(5) model  
M. Jöstingmeier, W. Hanke, S. Capponi and Shou-Cheng Zhang  
preprint available





## **Martin Jöstingmeier**

*Diplom-Physiker*

geboren: 1. Mai 1974

in Halle (Westf.)

verheiratet, keine Kinder

# **Lebenslauf**

1980 - 1984

1984 - 1993

09/1993 - 12/1993

12/1993 - 11/1994

11/1994 - 10/2000

09/1997 - 06/1998

09/1999 - 10/2000

10/2000

seit 12/2000

04/1998 - 06/1998

08/1995

## **Schul- und Berufsausbildung**

Grundschule Halle-Ost

Kreisgymnasium Halle (Westf.)

Abschluss: Allgemeine Hochschulreife

## **Wehrersatzdienst**

Ausbildung zum Rettungssanitäter:

Studieninstitut für kommunale Verwaltung  
in Ostwestfalen-Lippe

Rettungssanitäter beim Landkreis Gütersloh

## **Hochschulausbildung**

### **Studium der Physik:**

Bayerische Julius-Maximilians Universität  
Würzburg

### **Auslandstudium:**

Université Joseph Fourier  
Grenoble (Frankreich)

### **Diplomarbeit:**

Numerische Studien zur bosonischen  
Beschreibung von Spinsystemen

### **Abschluss: Diplom-Physiker**

### **Promotionsstudium**

### **Praktika**

Hutchinson, dép. FIT-Profilés,  
Moirans (Frankreich)

Qualitätskontrolle und Entwicklung

Treuhand Nordwest GmbH, Bielefeld



# Danksagung

---

Zu vorderst bedanke ich mich bei Herrn Professor Dr. Hanke; er ermöglichte mir auf diesem attraktiven und aktuellen Forschungsgebiet der Festkörperphysik mitzuarbeiten. Neben seiner physikalischen Intuition haben mir insbesondere seine Geduld und sein immer auf Fairness bedachter Sportsgeist sehr imponiert.

Besonders profitierte ich auch von der Zusammenarbeit mit Professor Dr. Arrigoni und Professor Dr. Assad. In zahlreichen Diskussionen haben sie mich an ihrem excellenten Fachwissen teilhaben lassen und viele gute Ideen zu meiner Arbeit beigesteuert. Dafür schulde ich ihnen großen Dank.

Ansgar Dorneich vermittelte mir viel Wissen im Bereich der Numerik und überließ mir sein Programmpaket, welches die Grundlage für meine eigenen Entwicklungen darstellte. Ihm und auch den anderen Kollegen der Arbeitsgruppe, möchte ich ganz herzlich für die angenehme und freundschaftliche Zusammenarbeit danken, namentlich sind dies Dr. Andrzej Fleszar, PD Dr. Michael Potthoff, PD Dr. Mikhail Kiselev, Christopher Dahnken, Dr. Marc Zacher, Thomas Eckl, Michael Bechmann, Sascha Brehm, Stephan Hochkeppel und Matthias Balzer sowie Christine Schmeisser und Bettina Spiegel.

Schlussendlich geht ein besonderer Dank an meine Frau Christina Maria und meine Eltern. Die Unterstützung, die ich von ihnen erfahren durfte, macht mich sehr glücklich und hat entscheidend dazu beigetragen, daß ich die Zeit des Promotionsstudiums nicht missen möchte. Allen ein herzliches 'Vergelt's Gott!'.



## **Eidesstattliche Versicherung**

Hiermit versichere ich, Martin Jöstingmeier geboren am 1. Mai 1974 in Halle (Westf.), an Eides statt, daß ich die vorliegende Arbeit eigenständig, d.h. insbesondere ohne Hilfe eines kommerziellen Promotionsberaters angefertigt habe. Es wurden keine anderen als in der Arbeit angegebenen Quellen und Hilfsmittel benutzt. Diese Arbeit liegt nicht in gleicher oder anderer Form in einem anderen Prüfungsfach vor.

Würzburg, am 10. Mai 2005

Martin Jöstingmeier